Compliant transmission mechanisms

Farhadi Machekposhti, Davood

DOI
10.4233/uuid:865dce30-2133-4e1a-add9-f0cb4ba4b3c4

Publication date
2018

Document Version
Final published version

Citation (APA)
Farhadi Machekposhti, D. (2018). *Compliant transmission mechanisms*. [Dissertation (TU Delft), Delft University of Technology]. https://doi.org/10.4233/uuid:865dce30-2133-4e1a-add9-f0cb4ba4b3c4

This book develops and validates kinematics and synthesis methods for the design of compliant transmission mechanisms, which are the alternatives to classical gears and couplings. The new theories are generated based on two nonlinear phenomena, singularity and buckling, which are often avoided.

The presented results pave the way for a new design platform for transmission mechanisms in the different field of applications, such as horology, robotics, medical instruments, and MEMS.

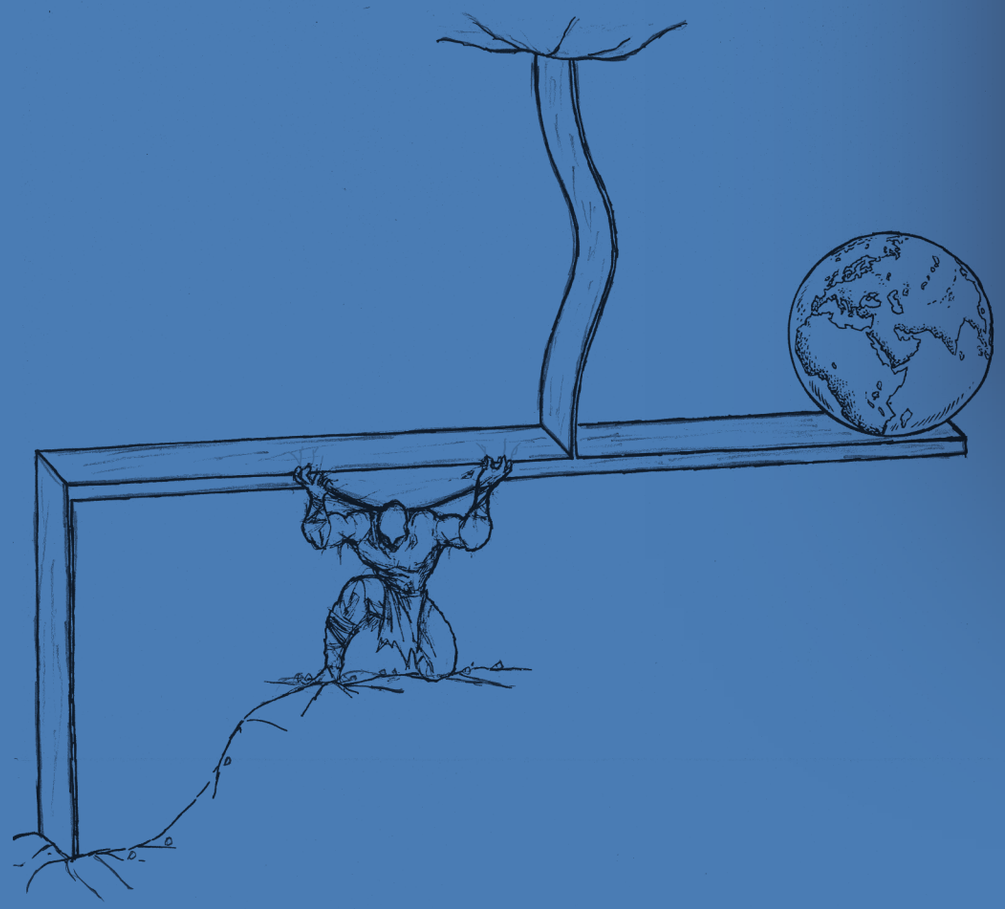

TU Delft Delft University of Technology

Compliant Transmission Mechanisms

Davood Farhadi Machekposhti

Compliant Transmission Mechanisms

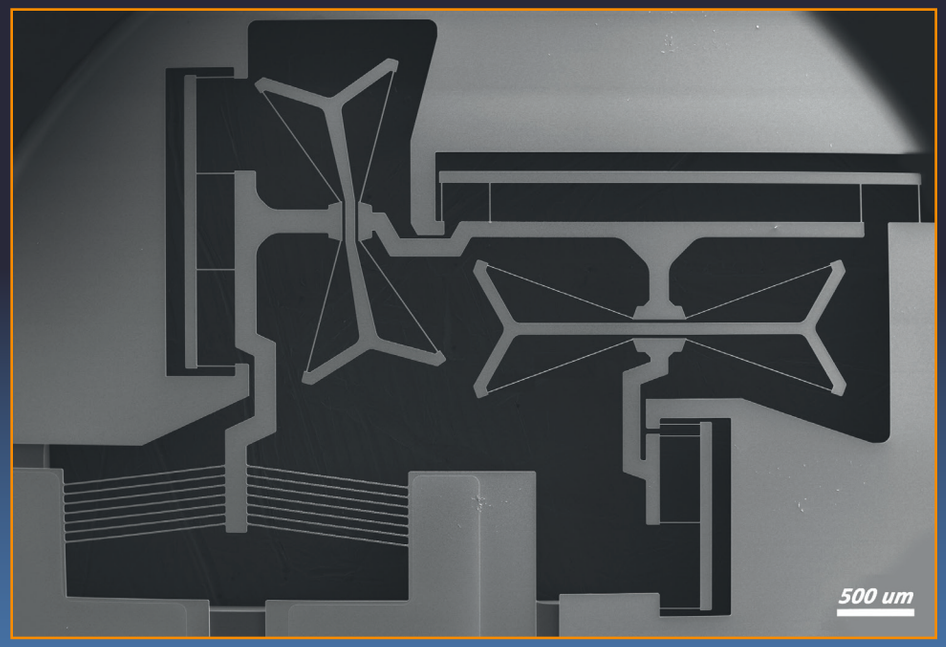

Davood Farhadi Machekposhti

COMPLIANT TRANSMISSION MECHANISMS

COMPLIANT TRANSMISSION MECHANISMS

Dissertation

for the purpose of obtaining the degree of doctor
at Delft University of Technology
by the authority of the Rector Magnificus, Prof. dr. ir. T.H.J.J. van der Hagen,
chair of the Board for Doctorates
to be defended publicly on
Wednesday 7, November 2018 at 10:00 o'clock

by

Davood FARHADI MACHEKPOSHTI

Master of Science in Mechanical Engineering-Applied Designing,
Babol Noshirvani University of Technology, Babol, Iran,
born in Sary, Iran.

This dissertation has been approved by the promotors.

Composition of the doctoral committee:

Rector Magnificus,	Chairperson
Prof. dr. J. L. Herder,	Delft University of Technology, promotor
Dr. N. Tolou,	Delft University of Technology, copromotor

Independent members:

Prof. dr. B. D. Jensen,	Brigham Young University, United States
Prof. dr. L. Zentner,	Ilmenau University of Technology, Germany
Prof. dr. J. P. M. B. Vermeulen	Eindhoven University of Technology, The Netherlands
Prof. dr. P. Breedveld,	Delft University of Technology, The Netherlands
Prof. dr. P. J. French,	Delft University of Technology, The Netherlands

This research is financed and supported by TAG Heuer and LVMH Watches Division.

Keywords: Compliant Mechanism, MEMS, Transmission, Frequency Multiplier, Coupling

Printed by: Gildeprint

Front: SEM image of a MEMS frequency multiplier transmission mechanism, with a ratio of 1:3, integrated with a thermal actuator. The device is based on the theories developed in Chapters 2 and 4.

Back: Sketch of a man and a lever arm, where the lever is suspended on two slender beams and utilizes buckling to swing the earth. The concept is based on the principle presented in chapter 3. The drawing was inspired and adapted from the famous quote by Archimedes: "Give me a place to stand, and I shall move the earth."

ISBN 978-94-6323-376-7

An electronic version of this dissertation is available at
`http://repository.tudelft.nl/`.

To my mother

who thought me the power of patience in
accomplishing important tasks;
who was illiterate but creative enough
to manage my first dictation practice
by putting the words on playing cards.

CONTENTS

PREFACE

In the last few decades, compliant mechanisms have shown a unique platform to design and develop alternatives to classical mechanical concepts and linkages. They are seeing expanded use due to several advantages such as part-count reduction, increased precision and reliability, and ability to miniaturize, e.g. to design Micro- and Nano-Mechanical devices. Although lots of compliant mechanisms in literature can be seen as a transmission mechanism, there has been no attempt to develop monolithic equivalents of classical transmission linkages such as gears and couplings. The purpose of this book is to fulfill this knowledge gap.

This book is the work that has been performed from June 2014 – June 2018 at Delft University of Technology. The research was financed and promoted by the LVMH Watch Division (TAG Heuer) and was part of a bigger project. The project was started in 2014, where the LVMH watch Division, Delft University of Technology and TU Delft spin-off Flexous teamed up to develop a new movement for mechanical wristwatches using compliant mechanism concept. In June 2014, I joined the team as a Ph.D. student to develop compliant transmission mechanisms. I enjoyed the opportunity to work with a group of brilliant engineers and researchers where their invaluable feedbacks made a big contribution to this work. For instance, while I was working to use the singularity and nonlinear behaviour of complex linkages to get the frequency and speed doubling feature (Chapter 2), the industrial requirements on kinematic linearity inspired me to look for a different alternative. In particular, I managed to utilize buckling, another nonlinear phenomenon, to design transmission linkages with linear kinematics (Chapter 3).

Meanwhile, my stay at the Technical University of Munich, between September 2017 and December 2017, was also fruitful. Working at a new environment gave me a unique opportunity to have a deeper insight into singularity analysis in the linkages and turn it into a mechanism design approach. In particular, it helped me to develop the synthesis method, presented in Chapter 4, for the design of compliant frequency multiplier transmission mechanisms.

Here, I would like to express my sincere gratitude to all the people who have been involved in my research in one way or another. To my promoter Just Herder for all the years of fruitful discussion and thinking together on fundamental kinematic challenges, his sharp feedback, excellent supervision, and encouragement. To my co-promoter Nima Tolou for his invaluable support and encouragement during my research. For his sharp comments and feedbacks on the technical aspect of the project and my Ph.D. management. Without his supervision and contributions, this research could not have been successfully conducted. I owe special thanks to both of them for offering me the opportunity to work on this project.

My gratitude also goes to the Chair of Applied Mechanics at the Technical University of Munich, Germany. Special thanks to Daniel Rixen for his wise comments and warm hosting. Great thanks also to my colleagues there, Christian, Eva-Maria, and Morteza.

I should add great thanks to all PME staff and PME support staff. I am particularly grateful to Farbod Alijani, Jo Spronck, Volkert van der Wijk, Fred van Keulen, Urs Staufer and Peter Steeneken for their feedback and support on different occasion. Hassan HosseinNia deserves special mention for his companion and having an open door for hours of discussion, feedback and suggestions.

I also want to extend a warm thank to my colleagues. To my fellow PhD-candidates and Post-Docs: Reinier, Gerard, Thijs, Patrice, Milton, Giuseppe, Freek, Stefan, Ali, Niranjan, Joep, Werner, Jelle, Alden, Wan, and Andres. To my project colleagues from Flexous: Oleg, Wout, Sybren, Marteen, Sjoerd, and Wouter, and from TAG Heuer: Christian, Thomas, Fabrice, Vincent and its general manager Dr. Guy Sémon. To all my master students, Iori, Jan, Henri, Thijs, Marije, Rijk, and Janeau who gave me the chance to learn and have more fun in parallel with my main Ph.D. research.

My greatest appreciation goes out to my family. To my dear parents, Salimeh and Hassan, for their endless love, support and encouragement. To my brother Mabood and my sister Mahroo for their love and encouragement.

I have waited until here to thank the most important one and express my love to her. To my greatest support, soul mate and running mate Fatemeh (Afagh) Safinia, who gives meaning to this work.

Davood FARHADI MACHEKPOSHTI
Delft, July 2018

1

INTRODUCTION

This chapter presents the aim of this thesis within the scope of compliant mechanisms and classical transmission mechanisms. The importance of compliant transmission mechanisms in different field of applications, such as Micro-Electro-Mechanical Systems (MEMS) and mechanical watches is elucidated. Besides, the background limitations and challenges are discussed and the structure of this thesis is schemed.

1

1.1. BACKGROUND

Transmission mechanisms are conventional machine elements, which provide a controlled transfer of power. Gears, linkages and couplings are the main examples of such mechanisms. Gears provide speed and torque conversion from a source of power to an output, whereas couplings convert the motion direction of a rotating input source. The history of classical gears and couplings dates back to a long time ago, where they were used in various human-made functional machines, a few of the oldest examples are shown in Figure 1.1. The south-pointing chariot, known as the first cybernetic machine (1050–771 BCE, China), used a complex set of gears to indicate south regardless of the trajectory of the carriage, Figure 1.1 (a) [1]. The Antikythera mechanism, the second oldest geared instrument (80 BC, Greece), is an ancient analog computer which employs 37 gears wheel to predict astronomical positions, Figure 1.1 (b) [2, 3]. Another example is the first sundial delineator (1676, England) where a nonlinear coupling was used to linearize the nonlinear motion of the shadow of a gnomon over the sundial, shown in Figure 1.1 (c) [4].

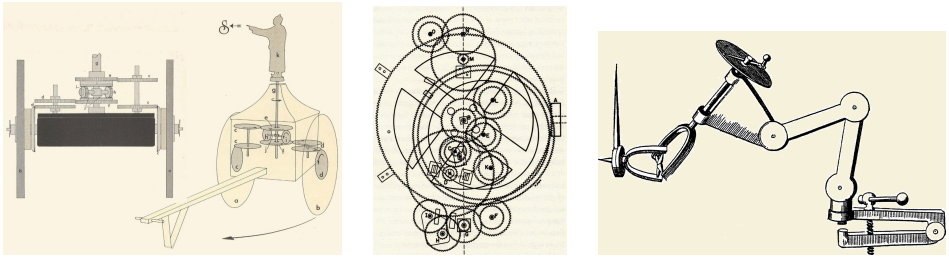

(*a*) (*b*) (*c*)

Figure 1.1: Historical background to the classical transmission mechanisms, gears and couplings; (a) South-pointing chariot (200 AD, China), (b) Antikythera mechanism (80 BC, Greece), and (c) Hooke's sundial delineator (1676, England).

Advances in fabrication technique and design innovations led to numerous improvements for these continuously rotating rigid-body mechanisms. This enabled their application in different scales and field of applications, such as the few examples shown in Figure 1.2.

For example, consider the classical gears in mechanical wrist watches, shown in Figure 1.2 (a). A train of several tiny gears transfers the stored energy in the barrel spring to the oscillating escapement to regulate the release of energy in precisely timed increments. In addition, gears are applied to transfer the motion of the escapement wheel to the hands which turn at different speed to indicate the time.

Another example can be found in the Micro-electro-mechanical systems (MEMS), the technology of microscopic devices. Several MEMS gears are employed in the design of micro engines, shown in Figure 1.2 (b), to control the torque and speed of the MEMS actuators. These tiny gears are produced in batch-fabrication without the need for assembly, using polysilicon surface micro machining techniques [7, 8].

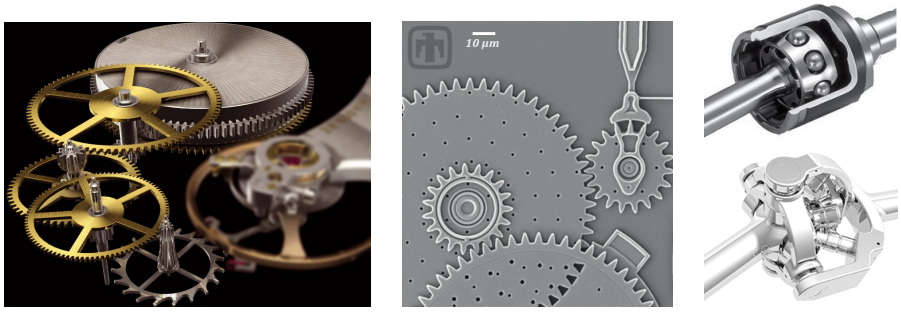

(*a*) (*b*) (*c*)

Figure 1.2: Advanced classical transmission mechanisms; (a) meso-scale gear train in the mechanical wrist watches, (b) micro gears in MEMS-based microengine (Sandia National Laboratories), and (c) constant velocity couplings in the automotive, measurement instrumentation, and robotic industry [5, 6].

The third example is formed by transmission couplings, shown in Figure 1.2 (c), which are one of the primary practical examples of three-dimensional linkages with spatial kinematics. These transmission mechanisms accommodate misalignment between two rotating axes while they keep a constant input-output velocity ratio. They have numerous application in the field of precision measurement and instruments, and laser processing.

1.2. PROBLEM STATEMENT AND MOTIVATION

Over the centuries, the working principle for these classical transmission mechanisms has remained almost the same. They consist of multiple rigid links which are engaged and connected by sliding contacts and movable hinges. The nature of these rigid-body mechanisms imposes a lot of disadvantages such as wear, friction, backlash, and the need for assembly, lubrication, and maintenance, which results in reduced precision, efficiency, and reliability. Moreover, it is difficult and sometimes not cost and energy efficient to miniaturize these rigid-body mechanisms.

For instance, a couple of meso-scale gears in mechanical watches have to be machined to near perfection and assembled precisely on tiny jewelry bearings to get a worthy movement with an efficiency about 92%. In spite of this level of perfection and effort on the fabrication and assembly process, the mechanical efficiency of the whole gear train in wristwatches usually ends up to 65%.

There are several obstacles to utilize rigid-body transmission mechanisms in MEMS applications. For example, wear and friction can dominate the performance of MEMS devices due to the large surface-to-volume ratios and low restoring forces. Figure 1.3 demonstrates a drive wheel in a MEMS micro engine and its rotational bearing after testing [9]. The evidence of wear and loss of silicon material can be seen in the picture. Wobbling, backlash, stiction, and poor mechanical efficiency are the other disadvantages of rigid-body mechanisms in MEMS devices [10, 11]. Besides, it is difficult, and it is not size and cost efficient to integrate the conventional gear transmissions with the MEMS-based actuating scheme such as electrostatic, piezoelectric, and shape-memory

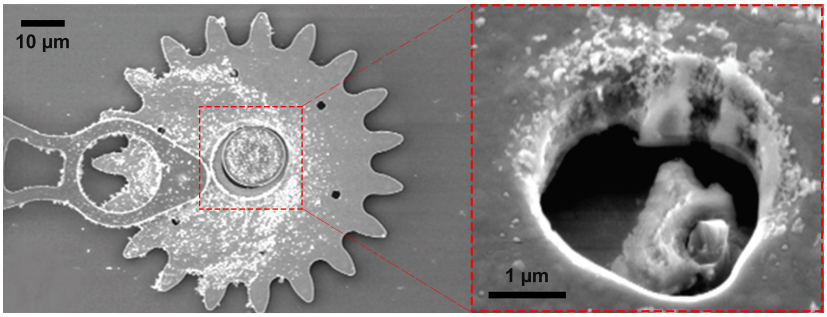

Figure 1.3: Friction and wear in a rotational bearing in a silicon MEMS device [9].

alloys.

Another disadvantage of rigid-body transmissions, like couplings, are usually their complexity in kinematics. These mechanisms have lots of parts, connections, and hinges. For example, even a simple coupling like Rzeppa joint, shown in Figure 1.4, has at least 13 different parts. Miniaturization of these transmissions is nearly impossible since the common MEMS-based fabrication techniques use a single planar layer or multiple layers of material to produce two dimensional or two and a half dimensional devices [12].

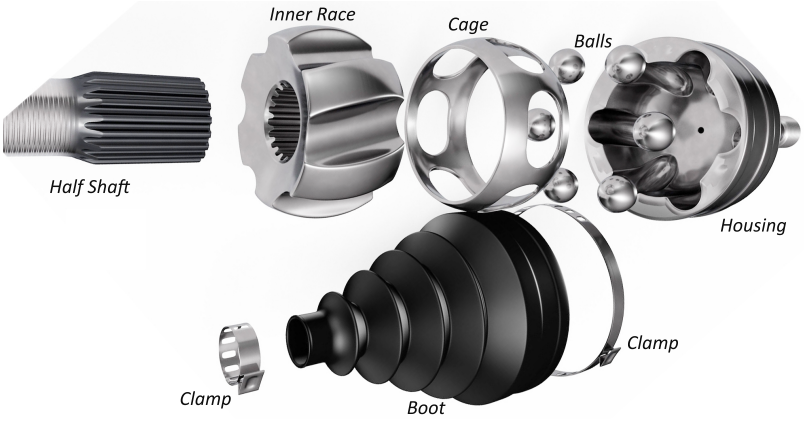

Figure 1.4: Rzeppa joint is one of the simplest constant velocity coupling, with at least 13 different components.

Therefore, design alternatives for these classical machine elements, which can deal with the disadvantages mentioned above, can pave the way for new possibilities and design platforms in different fields and industries, such as horology, robotics, aerospace, medical instruments, and MEMS.

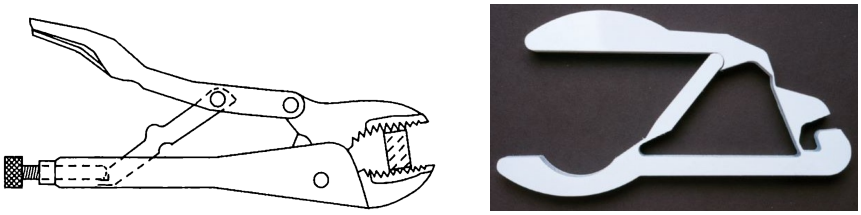

(*a*) (*b*)

Figure 1.5: (a) Rigid-body vice grip, and (b) its compliant and single piece counterpart [13].

1.3. COMPLIANT MECHANISMS

To realize sophisticated motions with minimal mechanical complexity the natural elasticity of materials can be employed, rather than using the rigid hinges and connections. This relatively new paradigm in engineering design, called compliant mechanisms, enables the creation of solid state (monolithic) mechanisms that are strong, compliant, precise, and reliable [13–16]. Besides, the main advantage of the compliant mechanisms is the potential for monolithic fabrication and results in the minimum number of parts to accomplish a specified task [13]. The rigid-body vice grip, Figure 1.5 (a), and its compliant equivalent, Figure 1.5 (b), is an example of part reduction.

There are several methods available in prior art to design compliant mechanisms, such as rigid-body replacement method [13], Freedom and Constraint Topologies (FACT) [17, 18], and Topology optimization [19]. The rigid-body replacement method is the most useful and practical method for the design of large deflection compliant mechanisms [20]. This method uses the traditional kinematic synthesis knowledge and Pseudo-Rigid-Body Model (PRBM) for the transition to a compliant equivalent [21–23]. Consider the vice grip mechanism shown in Figure 1.5 (a). Through relatively simple steps a compliant vice grip can be made as shown in Figure 1.5 (b), by cutting a piece of material and thinning the relatively rigid parts at the points where the rigid-body hinges are supposed to be.

1.4. KNOWLEDGE GAP AND RESEARCH OBJECTIVE

The rigid-body replacement method will be selected as a suitable design approach for the transition of existing rigid-body mechanisms to compliant equivalent. However, the current principles of classical gears and couplings impose three limitations to design their compliant alternatives.

Continuous Rotation: One of these limitations is that classical transmission mechanisms are rotating continuously but the range of motion for a compliant mechanism will be limited by the stress in the material which will not allow getting a continuous rotation.

Force Transmission: The transmission principle for conventional gears and couplings is based on the engagement between separated bodies and form closure like teeth and sliding contacts, while in compliant mechanisms motion will be transferred by elastic deformation of its own materials and preferably within a monolithic embodiment.

Kinematics: The kinematic alternatives for these classical transmission mechanisms

are limited. For instance, gears convert force and speed by converting the motion frequency based on different gearing ratios. However, there is not suitable kinematics as an alternative to classical gears for motion frequency multiplication.

Therefore, the objective of this thesis is ***to develop kinematics and synthesis methods for the design of compliant transmission mechanisms as the alternatives to classical gears and couplings.***

1.5. THESIS OUTLINE

The outline of this thesis is visually illustrated in Figure 1.6. The overall structure of the study takes the form of six chapters, including:

Chapter 2 introduces and analyzes new methods and kinematics for the design of compliant frequency doubler transmissions, an alternative to classical gearing mechanism with the ratio of two. The building blocks proposed in this chapter doubles the motion frequency with nonlinear kinematics by utilizing the presence of singularity in kinematic chains.

Chapter 3 presents and develops novel kinematics for the design of compliant frequency doubler transmission, an alternative to classical gearing mechanism with a ratio of two. The proposed building block in this chapter follows linear kinematics and utilizes buckling in compliant beams to double the motion frequency of a reciprocating input.

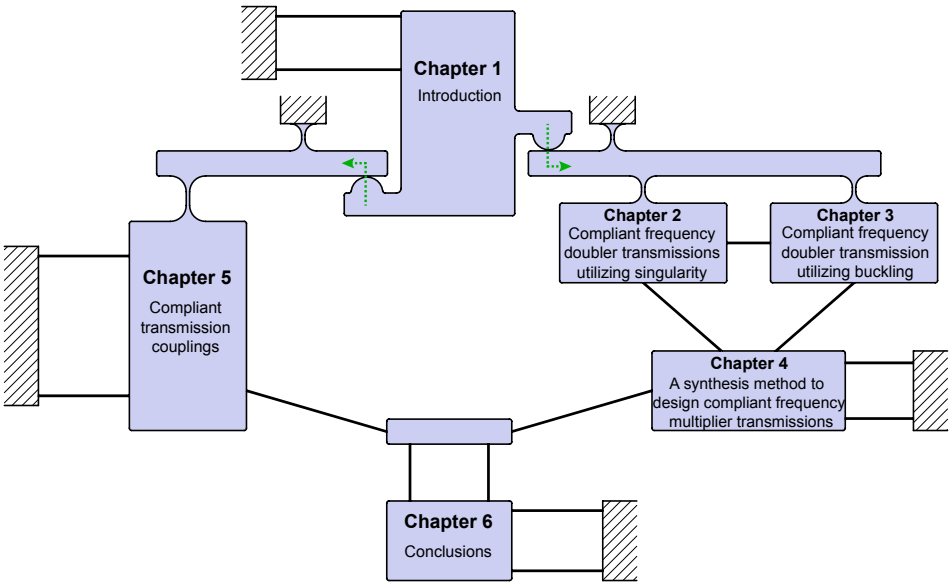

Figure 1.6: A schematic representation of the outline of this thesis. Two different paths are indicated, with two green arrows, for the readers. The right path includes Chapters 2, 3, and 4 and address the compliant frequency multiplier transmission mechanisms as the alternatives to classical gears. The left path contains Chapter 5 and covers the compliant alternatives to classical transmission couplings.

Chapter 4 proposes a synthesis method to design compliant frequency multiplier transmission mechanisms. The frequency doubler transmissions developed in *Chapter 2* and *Chapter 3* are used as principal building blocks to design any integer frequency ratios.

Chapter 5 presents the design of compliant transmission couplings which can accommodate different misalignments. The first section develops a compliant constant velocity coupling for rotational axes with an angular misalignment and the second section elaborates on a compliant transmission coupling for rotational axes with a lateral misalignment.

Chapter 6 summarizes the most important results and implications of this research, together with recommendations covering potential improvements or aspects for future investigation before the proposed compliant transmission mechanisms reach commercial maturity.

1

REFERENCES

[1] J. Needham, L. Wang, and G. D. Lu, *Science and civilisation in China*, Vol. 5 (Cambridge University Press Cambridge, 1963).

[2] D. de Solla Price, *Gears from the greeks. the antikythera mechanism: a calendar computer from ca. 80 bc,* Transactions of the American Philosophical Society , 1 (1974).

[3] T. Freeth, Y. Bitsakis, X. Moussas, J. H. Seiradakis, A. Tselikas, H. Mangou, M. Zafeiropoulou, R. Hadland, D. Bate, A. Ramsey, *et al., Decoding the ancient greek astronomical calculator known as the antikythera mechanism,* Nature **444**, 587 (2006).

[4] A. Mills, *Robert hooke's 'universal joint'and its application to sundials and the sundial-clock,* Notes and Records **61**, 219 (2007).

[5] A. H. Rzeppa, *Universal joint,* (1935), uS Patent 2,010,899.

[6] G. A. Thompson, *Constant velocity coupling and control system therefor,* (2006), uS Patent 7,144,326.

[7] J. J. Sniegowski and E. J. Garcia, *Surface-micromachined gear trains driven by an on-chip electrostatic microengine,* IEEE Electron Device Letters **17**, 366 (1996).

[8] K. Deng, M. Mehregany, and A. S. Dewa, *A simple fabrication process for polysilicon side-drive micromotors,* Journal of microelectromechanical systems **3**, 126 (1994).

[9] D. M. Tanner, W. M. Miller, K. A. Peterson, M. T. Dugger, W. P. Eaton, L. W. Irwin, D. C. Senft, N. F. Smith, P. Tangyunyong, and S. L. Miller, *Frequency dependence of the lifetime of a surface micromachined microengine driving a load,* Microelectronics Reliability **39**, 401 (1999).

[10] K. Gabriel, F. Behi, R. Mahadevan, and M. Mehregany, *In situ friction and wear measurements in integrated polysilicon mechanisms,* Sensors and Actuators A: Physical **21**, 184 (1990).

[11] K. Deng, R. J. Collins, M. Mehregany, and C. N. Sukenik, *Performance impact of monolayer coating of polysilicon micromotors,* Journal of the Electrochemical Society **142**, 1278 (1995).

[12] M. J. Madou, *Fundamentals of microfabrication: the science of miniaturization* (CRC press, 2002).

[13] L. L. Howell, *Compliant mechanisms* (John Wiley & Sons, 2001).

[14] S. Kota, J. Hetrick, Z. Li, and L. Saggere, *Tailoring unconventional actuators using compliant transmissions: design methods and applications,* IEEE/ASME Transactions on mechatronics **4**, 396 (1999).

[15] S. Kota, J. Joo, Z. Li, S. M. Rodgers, and J. Sniegowski, *Design of compliant mechanisms: applications to mems,* Analog integrated circuits and signal processing **29**, 7 (2001).

[16] B. P. Trease, Y.-M. Moon, and S. Kota, *Design of large-displacement compliant joints,* Journal of mechanical design **127**, 788 (2005).

[17] J. B. Hopkins and M. L. Culpepper, *Synthesis of multi-degree of freedom, parallel flexure system concepts via freedom and constraint topology (fact)–part i: Principles,* Precision Engineering **34**, 259 (2010).

[18] J. B. Hopkins and M. L. Culpepper, *Synthesis of multi-degree of freedom, parallel flexure system concepts via freedom and constraint topology (fact). part ii: Practice,* Precision Engineering **34**, 271 (2010).

[19] M. Frecker, G. Ananthasuresh, S. Nishiwaki, N. Kikuchi, and S. Kota, *Topological synthesis of compliant mechanisms using multi-criteria optimization,* Journal of Mechanical design **119**, 238 (1997).

[20] L. L. Howell, S. P. Magleby, and B. M. Olsen, *Handbook of compliant mechanisms* (John Wiley & Sons, 2013).

[21] L. L. Howell and A. Midha, *A method for the design of compliant mechanisms with small-length flexural pivots,* Journal of mechanical design **116**, 280 (1994).

[22] L. L. Howell and A. Midha, *Parametric deflection approximations for end-loaded, large-deflection beams in compliant mechanisms,* Journal of Mechanical Design **117**, 156 (1995).

[23] L. L. Howell and A. Midha, *A loop-closure theory for the analysis and synthesis of compliant mechanisms,* Journal of mechanical design **118**, 121 (1996).

2

COMPLIANT FREQUENCY DOUBLER TRANSMISSIONS UTILIZING SINGULARITY

Many compliant stroke amplifiers exist for the transformation of displacement and force. However, the transformation of operating frequency by compliant mechanisms is much more scarce, and compliant transmission mechanisms for frequency multiplication were not reported yet. Singularity is one of the focal topics in kinematics, which usually provides an insight of practical and theoretical limitations for the design and control of the mechanisms. This chapter presents a new type of compliant transmission mechanisms which utilizes singularity to double the motion frequency of a reciprocating input motion. Section 2.2 is concerned with a new movement principle for frequency multiplication, proposed based on singularity in kinematic chains. The next section, Section 2.3, discusses the compliant design criteria for this type of transmission mechanisms. The following sections, Sections 2.4 and 2.5, address two different compliant frequency doubler building blocks with non-linear kinematics. The building blocks in Section 2.4 utilize the singularity in a four-bar linkage to double an input motion frequency. However, the input-output velocity ratio is decreased due to the movement around the singularity in a four-bar mechanism. Therefore, new kinematics and compliant design based on an eight-bar linkage are developed in Section 2.5 to increase input-output velocity ratio as well as frequency doubling. Furthermore, in both sections, corresponding designs were dimensioned and fabricated to validate the theoretical models and finite-element model (FEM) with the experimental evaluations at different length scale.

Parts of this chapter have been published in *Journal of Microelectromechanical Systems* [1].

2.1. INTRODUCTION

Displacement, force, and operation frequency are the main criteria for selection of an actuator for an application, while also size, cost, efficiency, and power supply have a great impact on choosing an actuator [2]. A power transmission mechanism is needed when actuator specifications do not match the requirements of a given application.

Many transmission mechanisms exist for the transformation of displacement and force such as lever mechanisms for the case of translational actuators and gears for the case of rotational actuators. Lever mechanisms work in finite travel range translational displacement, while gear mechanisms are based on a continuous rotational displacement. Consequently, gears convert the frequency of an input rotation, while lever mechanisms solely increase the translational range of an input translation. Gear trains are the only examples of transmission mechanisms that have been used in mechanical and micro-electro-mechanical systems (MEMS) [3, 4] to multiply the motion frequency. However, gears are rigid-body mechanisms which generally give rise to many drawbacks such as friction, backlash, wear, and the need for assembly, lubrication, and maintenance. Besides, it is difficult to achieve full cycle rotational motion with the existing MEMS fabrication technology [3].

To deal with the shortcomings of rigid-body mechanisms, many compliant lever mechanisms exist in the prior art for the transformation of displacement and force in micro-mechanisms [5–14]. Generally, two types of lever transmission can be found, these being the mechanical levers, which are based on different planar linkages, and soft-spring/stiff-spring attenuation [15], examples are shown in Figure 2.1.

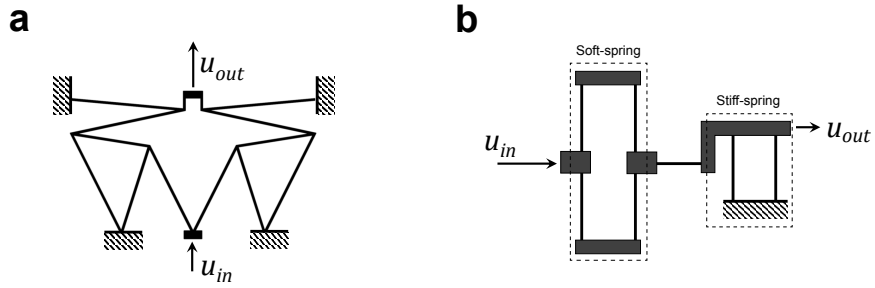

Figure 2.1: Different compliant lever transmission mechanisms. (a) A compliant displacement amplifier based on double slider linkage arrangement [5]. (b) A compliant displacement reducer based on soft-spring/stiff-spring concept [15].

In spite of different concepts for the design of compliant displacement amplifier transmissions, the conversion of motion frequency by compliant mechanisms is much more rare. The monolithic nature of such mechanisms could allow for miniaturization and enable a compact system design by integration of the transmission mechanism and actuation part.

In this chapter, we propose a new method for the design of compliant frequency doubler transmissions, based on exploiting the singularity in the rigid-body mechanisms. The main advantage of the proposed movements is that the mechanism does not need full cycle rotational joints or frictional contacts to double frequency.

The first building block presented in this chapter, discussed in Sections 2.4, utilizes the singularity in a four-bar mechanism. The design principle and the pseudo-rigid-body model (PRBM) are presented and described in this section. Besides, a compliant micro Frequency-Quadrupler is designed and discussed as a case study based on a building block approach. Moreover, finite element analysis (FEA) is carried out, and experiments are conducted to cross validate the characteristics of the proposed compliant transmission mechanism in micro scale. The second frequency doubler building block developed in this chapter is based on an eight-bar linkage, presented in Section 2.5. The proposed kinematics double both motion frequency and speed of reciprocating input motion. To validate the kinematics, PRBM, and FEM, a macro scale device was designed and dimensioned for experimental evaluations.

2.2. MOVEMENT PRINCIPLE

A limited-cycle kinematic is proposed to multiply the motion frequency within a finite travel range. This will eliminate the need for problematic continuous, infinite travel range, rotational joints and rigid contact for frequency multiplication at the micro scale. A generalized input-output kinematic relationships for such a transmission mechanism is envisioned in Figure 2.2.

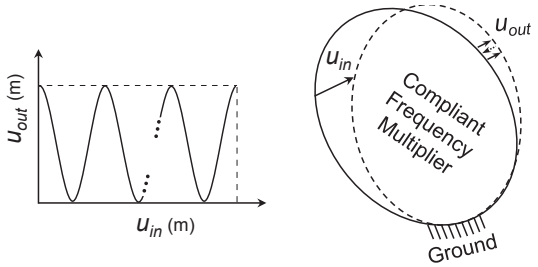

Figure 2.2: The generalized input-output displacement relationship of a compliant frequency multiplier transmission mechanism.

To increase the motion frequency, direction of the output motion, u_{out}, need to reverse while the input is subjected to the displacement u_{in}. This behaviour can be shown in the first kind of singularity in the rigid-body mechanisms (also called serial singularity), where the output link experiences zero velocity while the input subjected to a displacement. This type of kinematic singularity refers to a configuration where a kinematic chain reaches the boundary of the workspace.

Therefore, for a frequency multiplier transmission mechanism, the input-output frequency multiplication ratio can be identified based on the number of singularities of the first kind, m, in the kinematic chain within the considered range of motion, and can be given by

$$\frac{f_{out}}{f_{in}} = m+1 \tag{2.1}$$

where f_{out} (in cycles per second Hz) and f_{in} are the motion frequency of the input and the output members of the mechanism.

2.3. COMPLIANT DESIGN CRITERIA

To design a compliant frequency multiplier transmission mechanism different criteria need to be considered:

- ***Desired output displacement;*** *can be defined as the desired geometrical or mechanical advantage of a compliant transmission mechanism;*
- ***Transmission stiffness;*** *the stiffness of a compliant transmission mechanism in the direction of force transmission. In other words, the required stiffness of the transmission mechanism to an output load.*
- ***Actuation stiffness;*** *the stiffness felt by an actuator due to the internal stiffness of a compliant transmission mechanism.*
- ***Stress limitation;*** *limits to keep away from material failure, i.e. plastic deformation.*
- ***Dynamics and buckling instabilities.***

However, dynamics and buckling instabilities are not addressed in this thesis since the primary goal is to develop new kinematics and compliant designs.

2.4. A FREQUENCY DOUBLER BUILDING BLOCK BASED ON A FOUR-BAR LINKAGE

The proposed frequency doubler building block in this section is based on a four-bar linkage, where for a finite travel range there is only one configuration representing a singularity of the first kind. This can be shown in the double slider four-bar mechanism, Figure 2.3 (a), which can be a favorable choice for MEMS devices due to the rectilinear input and output motions. Therefore, based on Eq. 2.1, the mechanism can multiply the input motion frequency with a ratio of 1 : 2, Figure 2.3 (b). As can be seen, the motion

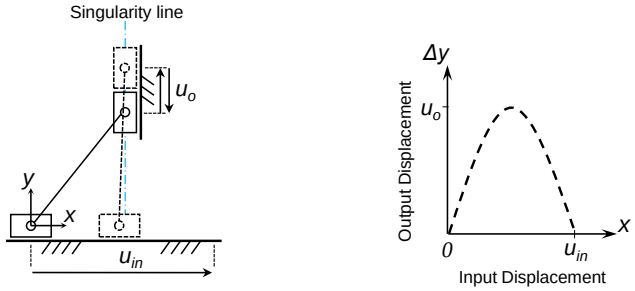

Figure 2.3: The double slider four-bar mechanism (a) rigid-body mechanism representation, (b) the input-output displacement relationship.

of the output slider (u_o) completes a full cycle while the input slider displaced with u_{in} from left to right, which is half a complete cycle.

Theoretically, a frequency multiplier mechanism with the ratio of 2^n can be achieved by concatenating n number of frequency doubler mechanisms, where $n = 1, 2, ..., N$. However, the output performs a small displacement compared to the input since the mechanism is working around the singularity. Therefore, this limits the use of this mechanism in a serial combination to reach higher multiplication ratios or reach the desired output displacement.

2.4.1. COMPLIANT DESIGN

Two partial compliant frequency doubler building blocks are proposed, shown in Figure 2.4. The stroke of the output is amplified by arranging two compliant equivalents of the double slider mechanism in series with a shared input. In the building blocks shown in Figure 2.4, a general embodiment is assumed for the beam elements of the flexures, where the geometric parameter a corresponds to the degree of distributed compliance [16]. The Building block shown in Figure 2.4 (a) can multiply the output frequency when a rectilinear cyclic motion with sinus function is subjected to the input. Therefore, the design with the initial configuration at the singularity can be the first building block in a series connection of frequency doubler mechanisms since the output will be a cosine motion. However, this can be solved by a pre-deflection at the input of each building block in respect with the output of the previous block or use the building block with an angled arrangement, illustrated in Figure 2.4(b).

COMBINATION WITH A COMPLIANT STROKE AMPLIFIER

The output displacement of the proposed frequency doubler building blocks is limited by the maximum input displacement and the length of the beams. Therefore, a compliant mechanical stroke amplifier can be paired with the output of the mechanism to am-

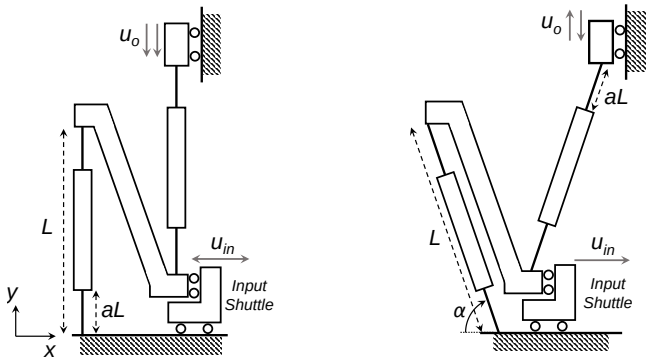

(*a*) (*b*)

Figure 2.4: Partially compliant frequency doubler building blocks, with two different initial shapes; (a) at the singularity, and (b) at the angled arrangement.

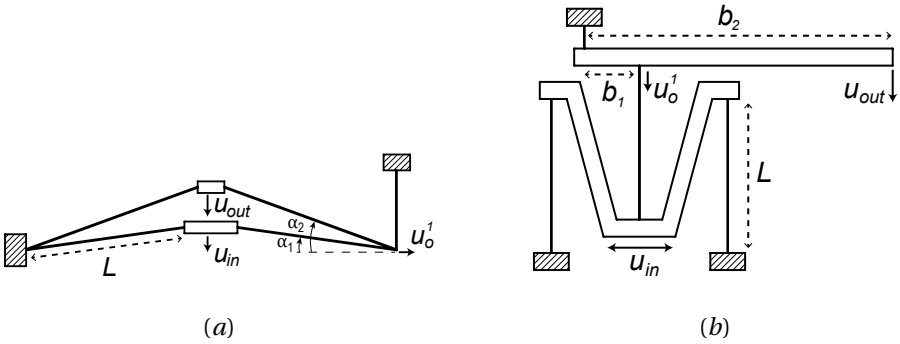

Figure 2.5: Combinations of frequency doubler building block and different compliant stroke amplifier concepts; (a) double slider mechanism (Case I), and (b) lever mechanism (Case II).

plify the displacement with a desired factor. There are different types of compliant stroke amplifiers available in the prior art which are generated based on different methods such as topology optimization [5, 6], instant center approach [8], and rigid-body replacement method. Two different examples are presented herein, which illustrate the combination of the proposed compliant cycle doubler building blocks with different types of stroke amplifier concepts, Figure 2.5. The output displacement from the cycle doubler building blocks, u_o^1, can be amplified to a desired output displacement, u_{out}, by a stroke amplifier. The Case I comprises two sets of angled beams where their ends are constrained by a vertical beam, shown in Figure 2.5 (a). The first set, with the angle of α_1, is the cycle doubler mechanism, equivalent to the angled arrangement shown Figure 2.4 (b). The second set with the angle of α_2 acts as a stroke amplifier with the instant multiplication ratio of $tan(\alpha_2)$, where the condition $\alpha_2 < 45$ should be satisfied to get a stroke multiplication ratio higher than one [8]. Case II, illustrated in Figure 2.5 (b), includes a compliant cycle doubler building block, equivalent to the arrangement shown in Figure 2.4 (a), paired with a lever arm as a stroke amplifier with a multiplication ratio of b_2/b_1.

2.4.2. PSEUDO-RIGID-BODY MODEL

KINEMATICS

The input-output displacement relationship of the building blocks, shown in Figure 2.4, can be described by the Pseudo-Rigid-Body model (PRBM) [17]. Considering a distributed compliance, $a = 0.5$, the output displacement of the building blocks shown in Figure 2.4 (a) can be given by

$$u_o = 2\gamma L\left(1-\sqrt{1-\left(\frac{u_{in}}{\gamma L}\right)^2}\right) \tag{2.2}$$

where, $\gamma = 0.8517$ is the characteristic radius factor for a fixed-guided flexible segment [17], and u_{in} is the reciprocating input motion.

In the same manner, the output displacement for the initially angled configuration,

Figure 2.4 (b), can be determined by

$$u_o = 2\gamma L\left(\sqrt{1-\left(\sin\alpha - \frac{u_{in}}{\gamma L}\right)^2} - \cos\alpha\right). \tag{2.3}$$

where α is the initial angle and for a reciprocating input motion u_{in} with an amplitude of U_{in} can be given by

$$\alpha = \arcsin\left(\frac{U_{in}}{2\gamma L}\right) \tag{2.4}$$

For lumped compliance, i.e. $a < 0.5$, the term γL should be replaced by $(L - aL)$ in all above-mentioned kinematic equations.

STIFFNESS CHARACTERISTICS

An ideal transmission mechanism provides the desired kinematics with a zero actuation force along its degrees of freedom (DOF) and zero displacements with infinite stiffness along its degrees of constraint (DOC). Compliant mechanisms naturally deviate from this ideal definition. Their actuation force is not zero due to their internal stiffness. Besides, distribution of compliance in a compliant transmission mechanism gives rise to elastokinematic effects in the transmission direction, which leads to a kinematic error between the input and the output motion when the mechanism is loaded.

The derivations for different stiffness characteristics of the beam modules using Euler's equation is discussed in [18]. By applying a similar technique, the proposed transmission building blocks yields the following input-output kinematics in compressive loading cases

$$u_o^L = u_o + \frac{F_{out}L^3}{2EI}\left(\frac{1}{\kappa} + \lambda\left(\frac{u_{in}}{L}\right)^2\right) \tag{2.5}$$

where, u_o^L is the output displacement in the presence of an output load, F_{out}. The symbol E denotes the Young's Modulus of the material, and I is the second moment of area, which for a beam with rectangular cross section (I_r) and a trapezoidal cross section (I_t) can be written by

$$I_r = \frac{1}{12}wt^3, \quad I_t = \frac{1}{48}w(t_1+t_2)\left(t_1^2+t_2^2\right). \tag{2.6}$$

where, w is the out of plane thickness, t is the in-plane thickness of the beam with a rectangular cross-section, and t_1 and t_2 are the top and bottom layer thickness of the beam with a trapezoidal cross-section, respectively.

In addition the dimensionless parameters λ and κ in Eq. 2.5 can be given by [16, 18]

$$\begin{aligned}\lambda &= \frac{2a^3\left(105-630a+1440a^2-1480a^3+576a^4\right)}{175\left(3-6a+4a^2\right)^3},\\ \kappa &= \frac{6L^2}{at^2}.\end{aligned} \tag{2.7}$$

The actuation stiffness, K_x, of the building blocks shown in Figure 2.4, which are a combination of two flexure based modules in parallel, can be given by written as

$$K_x = \frac{12EI}{aL^3\left(3-6a+4a^2\right)}. \tag{2.8}$$

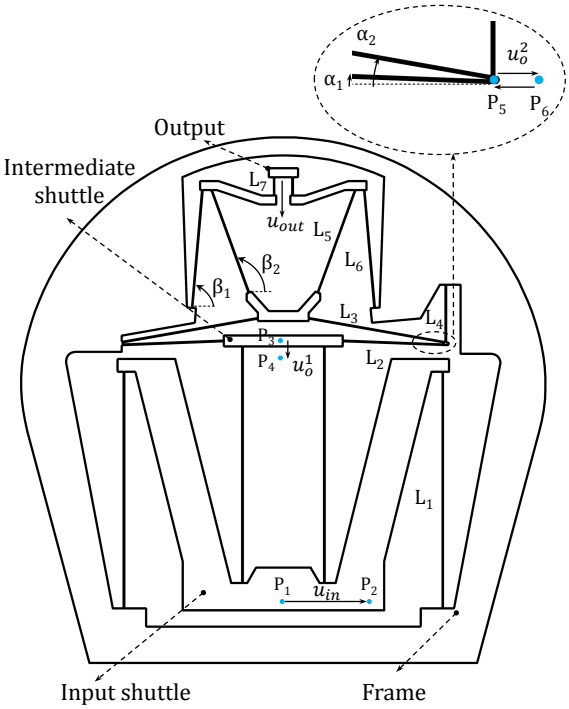

Figure 2.6: The design embodiment of compliant micro Frequency-Quadrupler.

Therefore, the actuation force for a compliant design with N concatenated proposed frequency doubler building blocks can be given by using virtual work principle

$$F_{in}\delta u_{in} = K_x^{(1)} u_{in}\delta u_{in} + \sum_{n=2}^{N} K_x^{(n)} u_o^{(n-1)}\delta u_o^{(n-1)} + F_{out}\delta u_{out}. \tag{2.9}$$

However, depending on where the stroke amplifiers and output load F_{out} are considered in the design, the corresponding terms need to be added.

2.4.3. EXPERIMENTAL RESULTS AND DISCUSSION

DESIGN

A compliant Frequency-Quadrupler is designed based on the proposed method, shown in Figure 2.6. The set of design parameters are summarized in Table 2.1. Furthermore, a constant thickness of $t = 30\mu m$ is considered in the drawing for all the flexures included in the design. The design composes two frequency doubler building blocks, concatenated with a set of stroke amplifiers. The design comprises an input shuttle which can be subjected to a reciprocating input motion, and it is connected to ground and an intermediate shuttle each with two parallel long length flexures. This is a fully compliant equivalent of the building block shown in Figure 2.4 (a). For an input displacement of u_{in} towards the right (from point P_1 to point P_2), the intermediate shuttle moves downwards

Table 2.1: Design parameters for the compliant micro Frequency-Quadrupler.

Parameters	L_1	L_2	L_3	L_4	L_5	L_6	L_7	β_1	β_2	α_1	α_2
Values	13 mm	5.5 mm	7.5 mm	3 mm	6 mm	6.5 mm	1 mm	85°	110°	2.21°	10°

from point P_3 to point P_4. Besides, the intermediate shuttle follows similar movement when the input moves towards the left with a displacement of u_{in}. Therefore, the intermediate shuttle completes two cycles for a full cyclic movement of the input, which results in a frequency multiplication factor of two. The intermediate shuttle is connected to ground and a cantilever beam, equivalent to concept Figure 2.5 (a), via two angled long length flexures, with the angle α_1. The endpoint P_5 travels to point P_6 and then return back to the same point P_5 (a complete cycle), while the intermediate shuttle moves from P_3 to point P_4. This provides another frequency doubling effect, which results in an overall frequency multiplication ratio of four between the input movement and the motion at point P_6. However, the stroke is small due to a consecutive combination of two motion frequency multipliers. Therefore, a stroke amplifier is connected to the output of compliant Frequency-Quadrupler mechanism with an multiplication ratio of 1 : 19. The compliant stroke amplifier design in this paper is based on the instant center approach [8], which contains a serial combination of double slider building blocks. According to the virtual work principle and Eq. 2.9, the actuation force of the proposed design can be given by

$$F_{in}\delta u_{in} = K_x^{(1)} u_{in}\delta u_{in} + K_x^{(2)} u_o^{(1)}\delta u_o^{(1)} + K_{sa} u_o^{(2)}\delta u_o^{(2)}, \tag{2.10}$$

where K_{sa} is the actuation stiffness of the designed compliant stroke amplifier, and $K_x^{(1)}$, and $K_x^{(2)}$ are the actuation stiffness of the first and second frequency multipliers building blocks, respectively, which for a distributed compliance can be written as

$$K_x^{(1)} = \frac{48EI}{L_1^3}, \quad K_x^{(2)} = \frac{24EI}{L_2^3}, \tag{2.11}$$

and, the terms $\delta u_o^{(1)}$ and $\delta u_o^{(2)}$ can be driven by the kinematic equations, Eq. 2.2 and Eq. 2.3, respectively,

$$\begin{aligned} \delta u_o^{(1)} &= \frac{2u_{in}}{\gamma L_1\sqrt{1-\left(\frac{u_{in}}{\gamma L_1}\right)^2}}\delta u_{in}, \\ \delta u_o^{(2)} &= \frac{2\left(\sin\alpha - \frac{u_o^{(1)}}{\gamma L_2}\right)}{\sqrt{1-\left(\sin\alpha - \frac{u_o^{(1)}}{\gamma L_2}\right)^2}}\delta u_o^{(1)}. \end{aligned} \tag{2.12}$$

FABRICATION

A micro device was fabricated in silicon using deep reactive ion etching (DRIE), shown in Figure 2.7. The prototype was made for experimental evaluations and to verify the

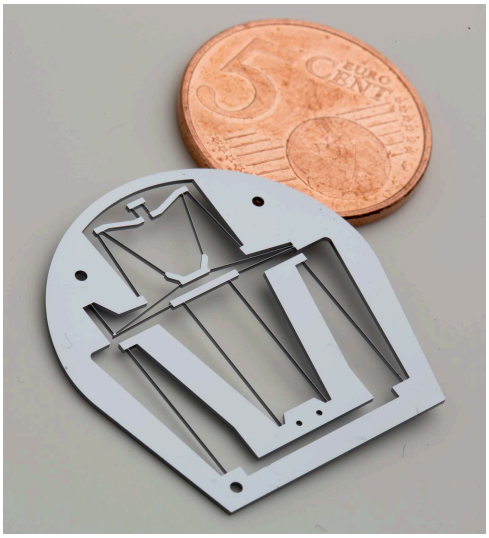

Figure 2.7: The prototype of the compliant Frequency-Quadrupler transmission fabricated out of Silicon using DRIE process.

Pseudo-Rigid-Body Model (PRBM) and the finite element model (FEM) of the actuation stiffness and the input-output kinematics. The design was first patterned on a $w = 525\mu m$ thickness silicon wafer and then etched by DRIE. This was done with the basic Bosch plasma etching process, which includes two subprocesses: the etching and the passivation, to produce a device with a high aspect ratio.

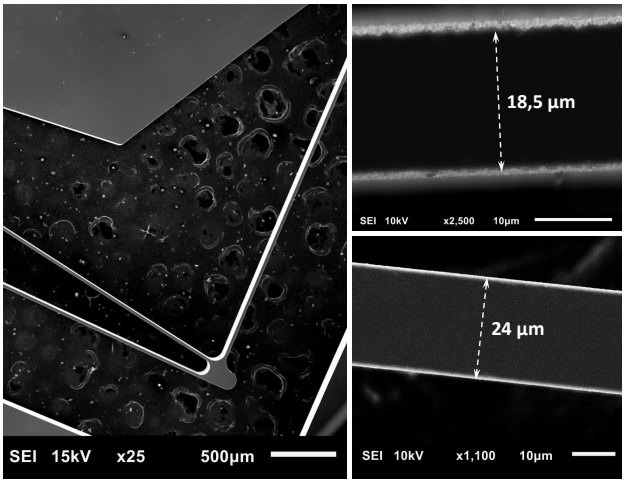

Figure 2.8: The zoomed-in scanning electron microscopy (SEM) image of the released device, with a uniform depth of 525 μm and feature size of 18.5 μm. Top and bottom right are showing the top and bottom view of the beams, respectively.

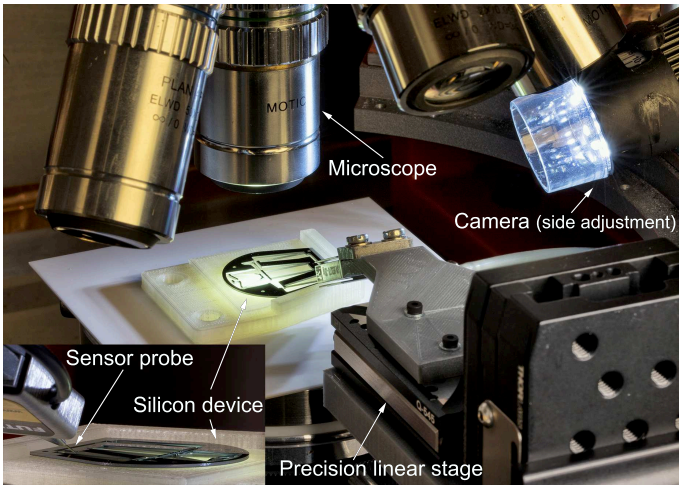

Figure 2.9: Experimental setup to evaluate the actuation force, and the input-output kinematics of the compliant Frequency-Quadrupler.

CHARACTERIZATION

The designed and dimensioned compliant embodiment is composed of flexures with a rectangular cross-section. However, the released fabricated device will get a trapezoidal cross section due to the non-constant etching rate of DRIE precess [19, 20]. Therefore, a scanning electron microscope (SEM) measurement was conducted to find the thickness of the flexures at the top and bottom layers. The results are then applied to the FEM and the PRBM by creating a customized cross-section based on the SEM results. The zoomed-in SEM image of the silicon device is shown in Figure 2.8.

A customized test setup was constructed for testing the actuation stiffness and the input-output kinematics of the silicon device, shown in Figure 2.9. The force deflection of the device is measured using a 20 $gram$ force sensor *(FUTEK LSB200)* with a resolution of 20 μN. The force sensor was mounted on a precision linear stage *(PI Q-545)*, with a resolution of 1 nm and minimum incremental motion of 6 nm, to provide a rectilinear input motion. A displacement of 2 mm is applied to the input shuttle of the micro device, and the movement of the output shuttle was simultaneously captured by an optical microscope *(Keyence VHX-1000E)*. The displacement was analyzed afterward using image processing, where it was detected with 500 nm accuracy.

PERFORMANCE

A parametric finite element model (FEM) was created in ANSYS to analyze the silicon made compliant Frequency-Quadrupler. The beam element based on Timoshenko beam theory *(BEAM188)* was used for the flexures, and rigid constraint elements *(MPC184)* for the intermediate bodies. Besides, a trapezoidal beam cross section was implemented for the flexures, based on the results from SEM image with the top layer thickness of $t_1 = 18.5\ \mu m$ and the bottom layer thickness of $t_2 = 24\ \mu m$. Besides, an orthotropic material properties for a standard (100) silicon wafer [21] were considered to investigate

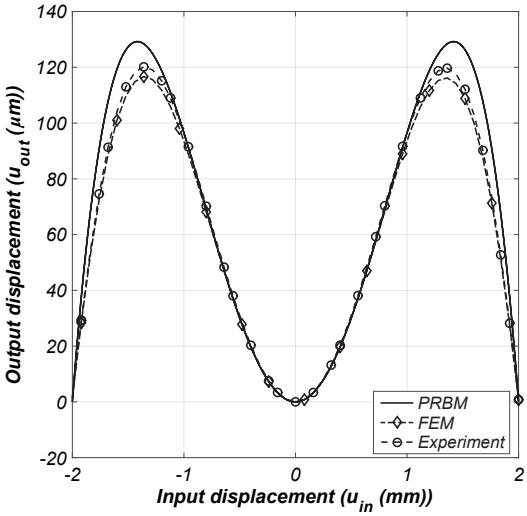

Figure 2.10: The results from Pseudo-Rigid-Body Model (PRBM), finite element model (FEM), and experiment for the input-output kinematics of the compliant Frequency-Quadrupler.

the device further: $E_x = E_y = 169\ GPa$, $E_z = 130\ GPa$ are the Young's Modulus, $\nu_{yz} = 0.36$, $\nu_{zx} = 0.28$, $\nu_{xy} = 0.064$ are the Poisson's ratio, and $G_{yz} = G_{zx} = 79.6\ GPa$, $G_{xy} = 50.9\ GPa$, $\rho = 2330\ kg/m^3$ are the shear modulus in different directions. The FEM model was evaluated while the maximum Von Mises stress was limited by the tensile yield strength of the silicon, 200 MPa. This value is considered far below the maximum yield strength of the silicon, which is about 6 GPa based on the prior art. This was an industrial constraint which was considered to prevent any risk of crack growth in silicon crystal of the proposed transmission mechanism.

The optical displacement measurement, FEM, and the Pseudo-Rigid-Body Model (PRBM) show the same behavior and order of magnitude for the input-output kinematic relationship, shown in Figure 2.10. As can be seen, the proposed compliant transmission mechanism multiplies the input motion frequency with a factor of four, and with a maximum output displacement of 120 μm. The PRBM shows maximum 6.7% discrepancy with the experimental results. This can be explained by the elastokinematic effects since the presented theoretical plot is based on the PRBM.

The compliant stroke amplifier provides a compressive spring force on the second compliant frequency doubler building block, corresponded to the angled beams with the angle α_1. The discrepancy between the PRBM and the experiment can be diminished to 1.6% by considering the elastokinematic effects on the displacement $u_o^{(2)}$ using Eq. 2.5. The corresponding stiffness of the compliant stroke amplifier is $K_{sa} = 8.8\ N/mm$, which was calculated by using the FEM model. In general, the performance of the output displacement will be closer to the PRBM model by an increase in the transmission stiffness K_y of the compliant frequency doubler building block. The improvement can be made by considering a lumped compliance design, i.e., $a < 0.5$, or a parallel arrangement of the angled beams. However, these will increase the actuation force of the compliant device.

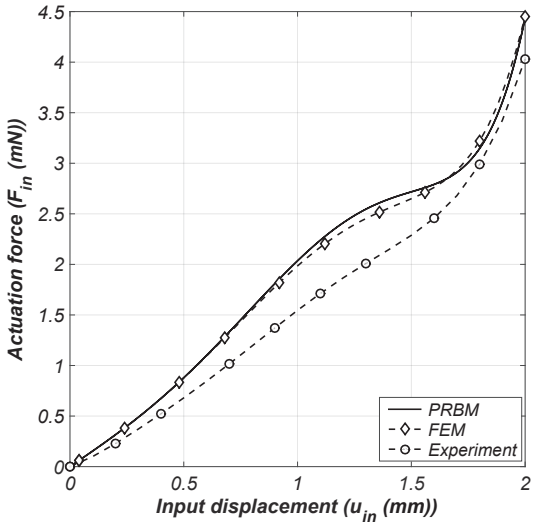

Figure 2.11: Force displacement characteristics of the micro compliant Frequency-Quadrupler. The results are from the Pseudo-Rigid-Body Model (PRBM), finite element model (FEM), and the experiment.

The force-deflection measurement is illustrated and compared to the FEM, and the PRBM in Figure 2.11. The results show a nonlinear correlation between the actuation force and the displacement, which can be explained by the nonlinear kinematics of the proposed compliant frequency doubler building block. Clearly, by increasing the input displacement the compliant device behaving as a linear spring, softening spring, and hardening spring, sequentially. Besides, it is shown that the results from FEM and the PRBM are in agreement. Although there is a small discrepancy between these results, maximum 3.4%, which explains the accuracy of the PRBM.

As can be seen in Figure 2.11, the result from measurement shows a more linear stiffness behavior as compared to both the FEM and the PRBM. Besides, a 9.4% discrepancy is observed on maximum actuation force between the measurement and the PRBM. These can be explained by uncertainties in the thickness measurement by SEM, $\pm 1.5 \mu m$. A decrease in thickness t of $0.5 \mu m$ for flexible members with an initial average thickness of $21.25 \mu m$ results in 7.8% decrease in the actuation force. Moreover, the difference in nonlinear stiffness behavior, between the PRBM and experiment, can be explained by the stiffness of compliant stroke amplifier, in which a similar trend can be observed between PRBM and experiment by 25% decrease in the actuation stiffness of the compliant stroke amplifier with an initial stiffness of $K_{sa} = 8.8\ N/mm$.

Based on the force-deflection results, there is a trade-off between adding compliant multipliers (frequency or stroke) and the additional motion stiffness that is associated with those. However, the principle of static balancing can be applied to remove the internal stiffness of different blocks, since the elastic force is a conservative force stored in the compliant elements. For instance, a balancing segment (preloaded beams) which provides a negative stiffness can be added to cancel the positive stiffness of each compliant building blocks [22, 23].

2.5. A FREQUENCY DOUBLER BUILDING BLOCK BASED ON AN EIGHT-BAR LINKAGE

In the previous section, compliant stroke amplifiers were concatenated with the proposed frequency quadrupler building block to increase its geometrical advantage ($G.A.$). However, even by using the stroke amplifiers with an amplification factor of 1 : 19, the output travel range of frequency quadrupler transmission was too small, i.e., with an average $G.A.$ of 0.125. As it was discussed, there were mainly two reasons. First, the frequency doubler building blocks used in the design were based on a four-bar linkage and entailed a stroke amplifier with a high amplification factor, at least 1 : 152, to achieve an overall $G.A. \geq 1$. Second, the mechanical advantage ($M.A.$) of a compliant transmission mechanism is not simply the reciprocal of $G.A.$, due to the internal elastic deformation of a monolithic system. In fact, for a compliant transmission mechanism with a positive internal stiffness the $M.A.$ decreases, and results in an overall reduction of $G.A.$. This will limit the applicability and design efficiency of the proposed building block approach, which is based on concatenating different building block of the frequency multiplier and stroke amplifiers.

Therefore, the objective of this section is to combine both functionalities, frequency

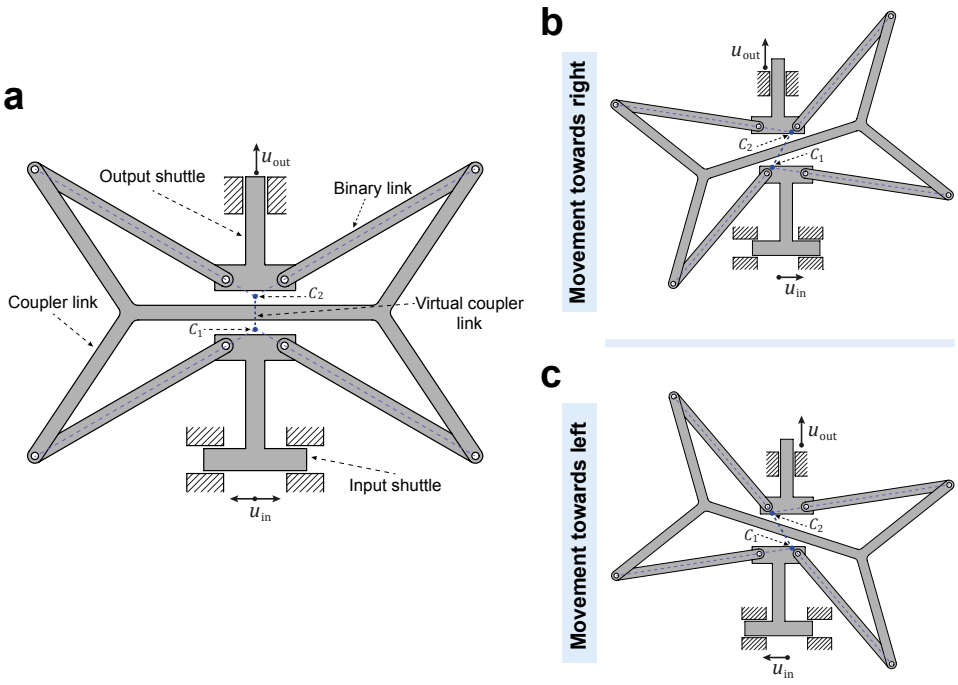

Figure 2.12: A frequency and speed doubler transmission mechanism. (a) A schematic representation of the proposed eight-bar linkage. (b) The first configuration, where the mechanism results in an upward output displacement for an input displacement towards the right. (c) The second configuration, the output moves again upward for an input displacement subjected towards the left.

doubling, and displacement amplification, in one transmission mechanism building block. This will eliminate the need for an extra compliant building block for the stroke amplification.

Based on Eq. 2.2, there are only two parameters to increase the output displacement of a compliant frequency doubler building block generated based on the double slider mechanism. These are the input displacement, u_{in}, and the effective length, L, of the coupler link. The output displacement can be increased by decreasing the effective length of the coupler link or applying a larger input displacement. However, both strategies increase the stress in an equivalent compliant design and are restricted by the allowable stress in the constitute material.

An eight-bar linkage is proposed, shown in Figure 2.12 (a), which double both the output displacement and the motion frequency. As can be seen in Figure 2.12 (b) and (c), the output shuttle always experiences an upward motion while the input reciprocates around the singularity configuration. The coupler link in this mechanism is connected to the input and the output shuttles with four binary links. The binary links provide two instantaneous centers of rotation, C_1 between the coupler link and the input shuttle, and C_2 between the coupler link and the output shuttle. The distance between these two instantaneous centers of rotation represents a virtual coupler link between the input and the output shuttles. In fact, this is an eight-bar linkage equivalent with double slider four-bar mechanism in which the effective length of the coupler link can be decreased virtually to achieve a larger output displacement. Moreover, the virtual coupler link changes in length while the mechanism is moving, due to the relocation of the instantaneous centers of rotation, and gives more parameters to optimize the mechanism for a desired *G.A.*.

2.5.1. COMPLIANT DESIGN

A compliant frequency doubler transmission building block is generated based on the proposed eight-bar linkage using the rigid-body replacement synthesis method, as shown in Figure 2.13. As can be seen, the binary links are replaced by the fixed-fixed distributed flexures with the length of L_2. Besides, the rigid-body prismatic joints at the input and the output shuttles are replaced by two double parallelogram (DP) flexures with the length of L_4, and L_5. In fact, these rectilinear flexure bearings provide a translational degree of freedom (DoF) for the input shuttle along the horizontal line, and for the output shuttle along the vertical line. The position of DP flexures respect to the fixed-fixed distributed flexures are indicated with the parameters p_1 and p_2. Although, different rectilinear flexure bearings can be found in the literature to replace the rigid-body prismatic joints in the design [16, 18, 24–31], where designers might choose different embodiments depends on the actuation, and transmission stiffness requirements. Here, the DP flexures are selected since it provides relatively low actuation stiffness for the input and the output shuttles while the bearing stiffness of these suspensions can be adjusted by the parameters w_1, w_2, w_3, and w_4.

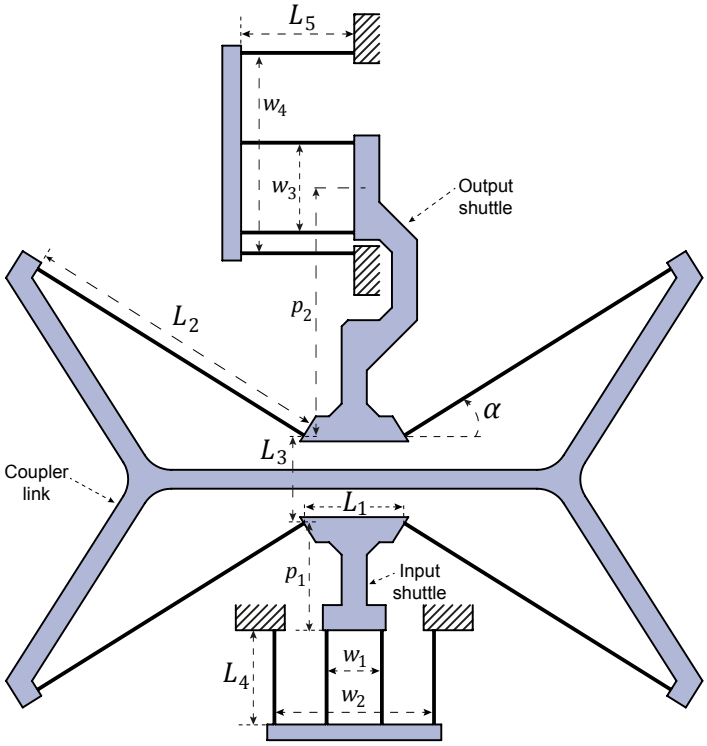

Figure 2.13: A compliant frequency doubler transmission building block based on the proposed rigid-body eight-bar linkage.

2.5.2. PSEUDO-RIGID-BODY MODEL

A Pseudo-Rigid-Body Model (PRBM) is presented to study the kinematics and stiffness characteristics of the proposed compliant design, as shown in Figure 2.14. As can be seen, the DP flexures are replaced by the sliders and corresponding translational stiffness, K_1 and K_2, which can be formulated as

$$K_1 = \frac{12EI}{{L_4}^3}, \quad K_2 = \frac{12EI}{{L_5}^3}. \tag{2.13}$$

where, E is the Young's Modulus of the material, and I is the second moment of area.

The fixed-fixed distributed flexures can be modeled as binary links, with the length of $L_2' = \gamma L_2$, associated with the torsional spring K_t at the hinges. The torsional spring constant for a fixed-fixed flexible segment can be given by [17]

$$K_t = 2\gamma K_\Theta \frac{EI}{L_2}. \tag{2.14}$$

where, $\gamma = 0.85$ is the characteristic radius factor, and $K_\Theta = 2.65$ is the stiffness coefficient.

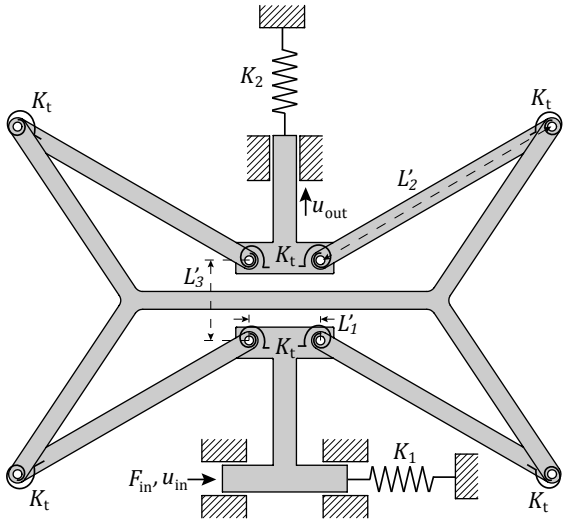

Figure 2.14: Pseudo-Rigid-Body Model (PRBM) of the proposed compliant frequency doubler transmission. All the torsional springs are equal and indicated with spring constant of K_t.

Moreover, the distances between end points of each two binary links, L_1' and L_3', in the PRBM can be given by

$$L_1' = L_1 + \big(1-\gamma\big) L_2 \cos\alpha, \qquad L_3' = L_3 + \big(1-\gamma\big) L_2 \sin\alpha. \tag{2.15}$$

KINEMATICS

Kinematic analysis is carried out using the PRBM to determine the motion characteristic of the compliant frequency doubler transmission mechanism. The complex number method is used for the position and velocity analysis of the mechanism. The vector loops, loop 1 and 2, are shown in Figure 2.15 and the associated complex vector loop equations can be formulated as

$$\vec{r}_1 + \vec{r}_2 - \vec{r}_5 - \vec{r}_4 = 0 \tag{2.16}$$

and

$$\vec{u}_{in} + \vec{r}_4 + \vec{r}_3 + \vec{r}_2 - \vec{y}_{out} = 0 \tag{2.17}$$

or

$$R_1 + R_2 e^{i\theta_2} - R_5 e^{i\left(\theta_3 - \frac{\pi}{2}\right)} - R_4 e^{i\theta_4} = 0 \tag{2.18}$$

and

$$u_{in} + R_4 e^{i\theta_4} + R_3 e^{i\theta_3} + R_2 e^{i\theta_2} - y_{out} e^{i\left(\frac{\pi}{2}\right)} = 0 \tag{2.19}$$

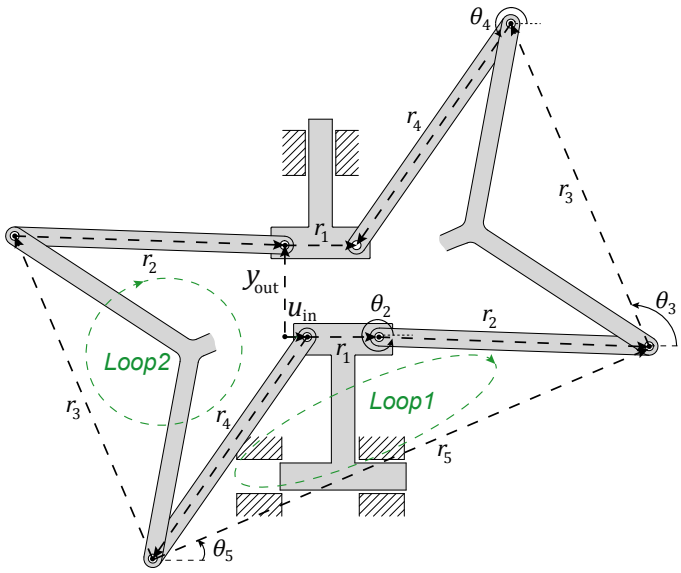

Figure 2.15: Vector loops for the proposed eight-bar frequency doubler linkage.

Expressing Eq. 2.18 and 2.19 in terms of their real and imaginary parts results in following scalar equations

$$R_1 + R_2\cos\theta_2 - R_5\sin\theta_3 - R_4\cos\theta_4 = 0 \tag{2.20}$$

$$R_2\sin\theta_2 + R_5\cos\theta_3 - R_4\sin\theta_4 = 0 \tag{2.21}$$

$$u_{in} + R_4\cos\theta_4 + R_3\cos\theta_3 + R_2\cos\theta_2 = 0 \tag{2.22}$$

$$R_4\sin\theta_4 + R_3\sin\theta_3 + R_2\sin\theta_2 - y_{out} = 0 \tag{2.23}$$

where,

$$\begin{aligned} &R_1 = L_1', \qquad R_2 = R_4 = L_2', \qquad R_3 = L_3' + 2L_2'\sin\alpha, \\ &R_5 = L_1' + 2L_2'\cos\alpha, \qquad y_{out} = L_3' + u_{out}. \end{aligned} \tag{2.24}$$

This results in four equations and four unknowns. The angles $\theta_2, \theta_3, \theta_4$, and the position of the output shuttle y_{out} are the unknowns for displacement analysis. These equations can be solved using a nonlinear equation solving method, such as the Newton-Raphson method. It is not trivial to express a closed-form equation for the proposed eight-bar linkage. However, these nonlinear functions can be approximated with a Taylor series expansion, where the unknown can be expressed semi-analytically.

The $\sin\theta$ and $\cos\theta$ terms can be approximated with a Taylor series expansion of an arbitrary order as

$$\begin{aligned} \sin\theta &= \sin\theta_0 + \Delta\theta\cos\theta_0 - \frac{\Delta\theta^2}{2}\sin\theta_0 + \dots, \\ \cos\theta &= \cos\theta_0 - \Delta\theta\sin\theta_0 - \frac{\Delta\theta^2}{2}\cos\theta_0 + \dots. \end{aligned} \tag{2.25}$$

where, the number of coefficients can be determined based on the required accuracy of the solution. Considering only the first two terms, neglecting the higher order, the Eq. 2.20-2.23 can be rewritten as

$$\begin{aligned} R_2\sin\theta_{20}\Delta\theta_2 + R_5\cos\theta_{30}\Delta\theta_3 - R_4\sin\theta_{40}\Delta\theta_4 \\ = R_1 - R_5\sin\theta_{30} + R_2(\cos\theta_{20} - \cos\theta_{40}) \end{aligned} \tag{2.26}$$

$$\begin{aligned} R_2\cos\theta_{20}\Delta\theta_2 - R_5\sin\theta_{30}\Delta\theta_3 - R_4\cos\theta_{40}\Delta\theta_4 \\ = -R_5\cos\theta_{30} - R_2(\sin\theta_{20} - \sin\theta_{40}) \end{aligned} \tag{2.27}$$

$$\begin{aligned} R_2\sin\theta_{20}\Delta\theta_2 + R_3\sin\theta_{30}\Delta\theta_3 + R_4\sin\theta_{40}\Delta\theta_4 \\ = u_{in} + R_3\cos\theta_{30} + R_2(\cos\theta_{20} + \cos\theta_{40}) \end{aligned} \tag{2.28}$$

$$\begin{aligned} R_2\cos\theta_{20}\Delta\theta_2 + R_3\cos\theta_{30}\Delta\theta_3 + R_4\cos\theta_{40}\Delta\theta_4 - y_{out} \\ = -R_3\sin\theta_{30} - R_2(\sin\theta_{20} + \sin\theta_{40}) \end{aligned} \tag{2.29}$$

where, θ_{20}, θ_{30}, and θ_{40} are the initial angles of the mechanism and can be given by

$$\theta_{20} = 2\pi - \alpha, \quad \theta_{30} = \frac{\pi}{2}, \quad \theta_{40} = \pi + \alpha. \tag{2.30}$$

This set of linear equations, where $\Delta\theta_2$, $\Delta\theta_2$, $\Delta\theta_2$, and y_{out} are the unknown, can be written in form of matrix equation as

$$Ax = b \tag{2.31}$$

where, A is the coefficient matrix, x is the vector of unknown, and b is the column vector of constant terms, which can be expressed as

$$A = \begin{bmatrix} R_2\sin\theta_{20} & R_5\cos\theta_{30} & -R_4\sin\theta_{40} & 0 \\ R_2\cos\theta_{20} & -R_5\sin\theta_{30} & -R_4\cos\theta_{40} & 0 \\ R_2\sin\theta_{20} & R_3\sin\theta_{30} & R_4\sin\theta_{40} & 0 \\ R_2\cos\theta_{20} & R_3\cos\theta_{30} & R_4\cos\theta_{40} & -1 \end{bmatrix}, \; x = \begin{bmatrix} \Delta\theta_2 \\ \Delta\theta_3 \\ \Delta\theta_4 \\ y_{out} \end{bmatrix}, \tag{2.32}$$

and,

$$b = \begin{bmatrix} R_1 - R_5\sin\theta_{30} + R_2(\cos\theta_{20} - \cos\theta_{40}) \\ -R_5\cos\theta_{30} - R_2(\sin\theta_{20} - \sin\theta_{40}) \\ u_{in} + R_3\cos\theta_{30} + R_2(\cos\theta_{20} + \cos\theta_{40}) \\ -R_3\sin\theta_{30} - R_2(\sin\theta_{20} + \sin\theta_{40}) \end{bmatrix}, \tag{2.33}$$

This set of equations has a unique solution which can be given by

$$x = A^{-1}b \tag{2.34}$$

where, A^{-1} is the inverse of A.

The velocities and kinematic coefficients of the proposed eight-bar linkage can be determined by differentiating the position equations, Eq. 2.18 and 2.19, with respect to time. This results in the following velocity equations

$$i\omega_2 R_2 e^{i\theta_2} - i\omega_3 R_5 e^{i\left(\theta_3 - \frac{\pi}{2}\right)} - i\omega_4 R_4 e^{i\theta_4} = 0 \tag{2.35}$$

and

$$V_{in} + i\omega_4 R_4 e^{i\theta_4} + i\omega_3 R_3 e^{i\theta_3} + i\omega_2 R_2 e^{i\theta_2} - V_{out} e^{i\left(\frac{\pi}{2}\right)} = 0 \tag{2.36}$$

Expressing Eq. 2.35 and 2.36 in terms of their real and imaginary parts results in

$$\omega_2 R_2 \sin\theta_2 + \omega_3 R_5 \cos\theta_3 - \omega_4 R_4 \sin\theta_4 = 0 \tag{2.37}$$

$$\omega_2 R_2 \cos\theta_2 - \omega_3 R_5 \sin\theta_3 - \omega_4 R_4 \cos\theta_4 = 0 \tag{2.38}$$

$$\omega_2 R_2 \sin\theta_2 + \omega_3 R_3 \sin\theta_3 + \omega_4 R_4 \sin\theta_4 - V_{in} = 0 \tag{2.39}$$

$$\omega_2 R_2 \cos\theta_2 + \omega_3 R_3 \cos\theta_3 + \omega_4 R_4 \cos\theta_4 - V_{out} = 0 \tag{2.40}$$

By solving the equations for the unknown velocities, the velocity ratios *(Kinematic coefficients)* can be given by

$$\frac{\omega_2}{V_{in}} = \frac{R_5 \cos(\theta_3 - \theta_4)}{R_2(R_5 \cos\theta_3 \sin(\theta_2 + \theta_4) + R_3 \sin\theta_3 \sin(\theta_4 - \theta_2) + 2R_5 \sin\theta_2 \sin\theta_3 \sin\theta_4)} \tag{2.41}$$

$$\frac{\omega_3}{V_{in}} = \frac{\sin(\theta_4 - \theta_2)}{R_5 \cos\theta_3 \sin(\theta_2 + \theta_4) + R_3 \sin\theta_3 \sin(\theta_4 - \theta_2) + 2R_5 \sin\theta_2 \sin\theta_3 \sin\theta_4} \tag{2.42}$$

$$\frac{\omega_4}{V_{in}} = \frac{R_5 \cos(\theta_2 - \theta_3)}{R_2(R_5 \cos\theta_3 \sin(\theta_2 + \theta_4) + R_3 \sin\theta_3 \sin(\theta_4 - \theta_2) + 2R_5 \sin\theta_2 \sin\theta_3 \sin\theta_4)} \tag{2.43}$$

$$\frac{V_{out}}{V_{in}} = \frac{R_3 \sin(\theta_4 - \theta_2) + R_5 \tan\theta_3 \sin(\theta_4 + \theta_2) + 2R_5 \cos\theta_2 \cos\theta_4}{R_5 \sin(\theta_4 + \theta_2) + R_3 \tan\theta_3 \sin(\theta_4 - \theta_2) + 2R_5 \sin\theta_2 \tan\theta_3 \sin\theta_4} \tag{2.44}$$

STIFFNESS CHARACTERISTICS

Actuation stiffness: The force-displacement characteristic for the proposed compliant frequency doubler transmission building block can be derived from the PRBM and the principle of virtual work. This results in

$$F_{in} = F_1 + 2T_1 \frac{\delta\theta_4}{\delta u_{in}} + 2T_2 \frac{\delta\theta_4 - \delta\theta_3}{\delta u_{in}} + 2T_3 \frac{\delta\theta_2 - \delta\theta_3}{\delta u_{in}} + 2T_4 \frac{\delta\theta_2}{\delta u_{in}} + (F_2 + F_{out}) \frac{\delta u_{out}}{\delta u_{in}} \tag{2.45}$$

where, $\delta\theta_2$, $\delta\theta_3$, $\delta\theta_4$, and δu_{out} are the virtual displacements. The ratio of these virtual displacements to the input virtual displacement, δu_{in}, can be given by the corresponding kinematic coefficients, Eq. 2.41 - 2.44.

The virtual work due to the torsional springs at hinges can be defined from the moment at the hinges, T_1, T_2, T_3, T_4, and the appropriate virtual displacement.

$$\begin{aligned} T_1 &= K_t(\theta_4 - \theta_{40}), \\ T_2 &= K_t((\theta_4 - \theta_{40}) - (\theta_3 - \theta_{30})), \\ T_3 &= K_t((\theta_2 - \theta_{20}) - (\theta_3 - \theta_{30})), \\ T_4 &= K_t(\theta_2 - \theta_{20}). \end{aligned} \tag{2.46}$$

where, K_t is the PRBM torsional spring constant, and θ_{i0} define the initial position of the mechanism at which all the spring are undeflected. Besides, the virtual work from the translational springs at the sliders, K_1 and K_2, can be given by

$$F_1 = K_1 u_{in}, \qquad F_2 = K_2 u_{out}. \tag{2.47}$$

Transmission stiffness: The proposed compliant frequency doubler mechanism is intended to double the motion frequency of actuation against an output load. Since the output load alters the desired kinematics of a compliant transmission mechanism, it is essential to discuss the limitations for different loading scenarios.

In the case of a pushing output force, the fixed-fixed distributed flexures will be under tensile loads. This is generally an ideal situation for a compliant transmission mechanism to maintain its kinematics in presence of an output load. However, the tensile forces at the fixed-fixed distributed flexures transfer a reaction force and moment along the degrees of constraint (DOC) of the rectilinear flexure bearings at the input and the output shuttles. Since there is an offset between the rectilinear flexure bearings and the endpoints of the fixed-fixed distributed flexures, the reaction moment is more dominant. This can impose parasitic rotations at the input and the output shuttles. The double parallelogram flexure (DP) at the output shuttle and its free body diagram is shown in Figure 2.16.

The reaction moments, caused by the output load F_{out}, on the DP flexures can be expressed as

$$M_1 = D_1 F_{out}, \qquad M_2 = D_2 F_{out}. \tag{2.48}$$

where, M_1 is the reaction moment at the input shuttle, M_2 is the reaction moment at the output shuttle, and the coefficients D_1 and D_2 can be determined by a static force

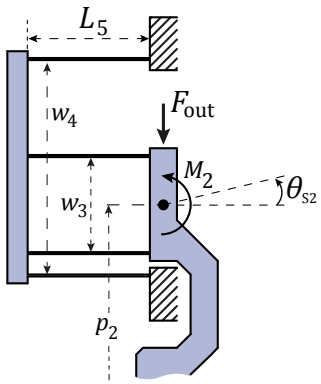

Figure 2.16: Double parallelogram flexure (DP) at the output shuttle and free body diagram.

analysis, and can be given by

$$D_1 = \frac{4p_1R_5\cos\theta_2\cos\theta_3\cos\theta_4 + \left(R_1R_5\cos\theta_3 - 2p_1R_3\cos\theta_3 + 2p_1R_5\sin\theta_3\right)\sin(\theta_2+\theta_4)}{2R_5\cos\theta_3\sin(\theta_4-\theta_2) + 2R_3\sin\theta_3\sin(\theta_4+\theta_2)}$$

$$+\frac{R_1R_3\left(\sin\theta_3\sin(\theta_4-\theta_2) - 2\cos\theta_3\sin\theta_2\sin\theta_4\right) + 2R_1R_5\sin\theta_2\sin\theta_3\sin\theta_4}{2R_5\cos\theta_3\sin(\theta_4-\theta_2) + 2R_3\sin\theta_3\sin(\theta_4+\theta_2)}, \tag{2.49}$$

and,

$$D_2 = \frac{R_1R_5\cos\theta_3\sin(\theta_4-\theta_2) + \left(2P_2R_3\cos\theta_3 + R_1R_3\sin\theta_3 - 2p_2R_5\sin\theta_3\right)\sin(\theta_4+\theta_2)}{2R_5\cos\theta_3\sin(\theta_4-\theta_2) + 2R_3\sin\theta_3\sin(\theta_4+\theta_2)}$$

$$+\frac{-4P_2R_5\cos\theta_2\cos\theta_3\cos\theta_4}{2R_5\cos\theta_3\sin(\theta_4-\theta_2) + 2R_3\sin\theta_3\sin(\theta_4+\theta_2)}. \tag{2.50}$$

The moment-angular displacement relationship of the DP flexures at the input and the output shuttles can be given by

$$M_1 = K_{\theta_{S_1}}\theta_{S_1}, \qquad M_2 = K_{\theta_{S_2}}\theta_{S_2}. \tag{2.51}$$

where, θ_{S_1} and θ_{S_2} are the parasitic rotations at the input and the output shuttles, respectively. $K_{\theta_{S_1}}$ and $K_{\theta_{S_2}}$ are the rotational stiffness of the DP flexures at the input and the output shuttles, respectively, which can be given by [18]

$$K_{\theta_{S_1}} = \frac{Ebt^3\kappa_1 w_1^2 w_2^2}{24L_4^3\left(w_1^2+w_2^2\right)\left(1+\kappa_1\lambda\left(\frac{u_{in}}{2L_4}\right)^2\right)}, \tag{2.52}$$

$$K_{\theta_{S_2}} = \frac{Ebt^3\kappa_2 w_3^2 w_4^2}{24L_5^3\left(w_3^2+w_4^2\right)\left(1+\kappa_2\lambda\left(\frac{u_{out}}{2L_5}\right)^2\right)}, \tag{2.53}$$

where, b and t are flexure width and thickness, respectively. And the non-dimensional coefficients λ, κ_1, and κ_2 are

$$\lambda = \frac{1}{700}, \quad \kappa_1 = \frac{12L_4^2}{t^2}, \quad \kappa_2 = \frac{12L_5^2}{t^2}. \tag{2.54}$$

By substituting Eq. 2.51 into Eq. 2.48, a direct relationship between the output force (F_{out}) and the parasitic rotations at the input (θ_{S_1}) and the output shuttles (θ_{S_2}) can be determined. Therefore, this relationship allows designing appropriate DP flexures at the input and the output shuttles for a given output force and maximum allowable parasitic rotation of the output shuttle.

In the case of a pulling output force, the four fixed-fixed distributed flexures will be under compressive loads, and the buckling load of the beams determines the maximum force transmission capability of the compliant design. Therefore, the maximum output pulling force can be estimated by the classical Euler–Bernoulli beam theory as

$$\text{Max. output pulling force:} \quad F_{out} = \frac{4\pi^2 EI}{{L_2}^2\sin\alpha}. \tag{2.55}$$

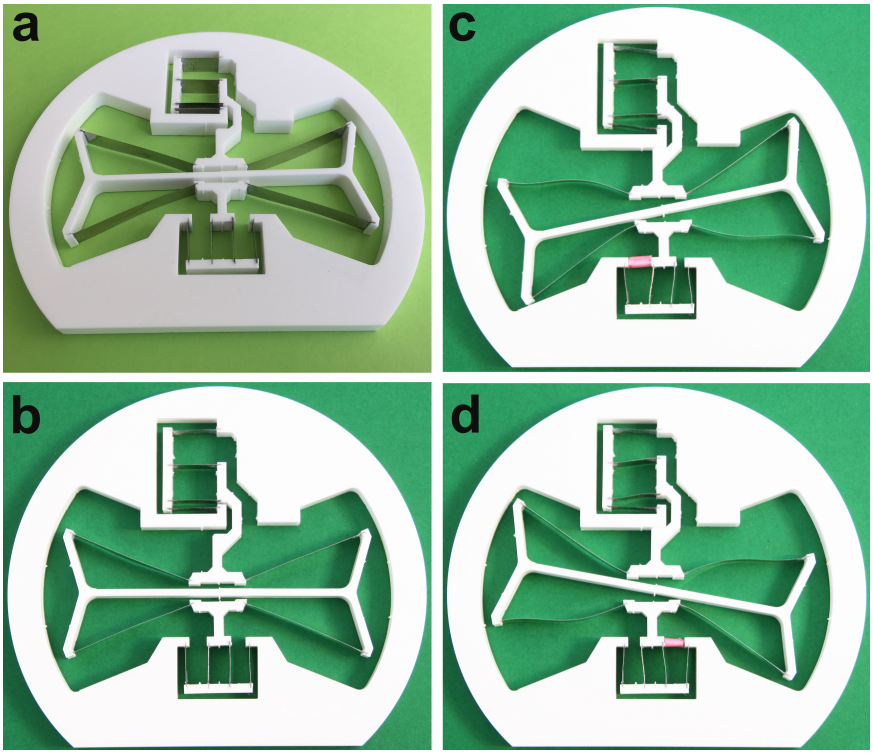

Figure 2.17: The prototype of compliant frequency and speed doubler transmission mechanism. (a) A 3D view of the prototype fabricated out of acrylic for the rigid parts and flexures out of steel. (b) The top view of the prototype at the rest position. (c) The prototype at the deflected positions, the input is deflected towards the right, (d) the input is deflected towards the left.

Although, the maximum pulling force can be increased by considering a lumped compliance design for the four fixed-fixed flexures instead of a distributed compliance.

2.5.3. EXPERIMENTAL EVALUATION AND DISCUSSION

In this section, the proposed compliant frequency doubler transmission building block is dimensioned and fabricated for experimental evaluation. Moreover, the results from experiments, finite element model (FEM), and the theoretical model are illustrated and discussed for the actuation stiffness and the input-output kinematics.

DESIGN AND FABRICATION

A macro scale compliant frequency doubler transmission is designed based on the proposed eight-bar linkage. The prototype design parameters are summarized in Table 2.2. The device is designed for a maximum input displacement of $1mm$, which results in an output displacement of $2mm$ with a doubled frequency. The austenitic stainless steel with the width of $b = 8mm$ and the thickness of $t = 0.05mm$ is used for all flexures in the design.

Table 2.2: Design parameters for the compliant macro frequency doubler transmission mechanism. All the length are given in [mm].

Parameters	L_1	L_2	L_3	L_4	L_5	w_1	w_2	w_3	w_4	p_1	p_2	α
Values	19	40	8.9	12	14.5	7	20	11.5	25.5	13.5	31.5	22°

A macro device was fabricated with the rigid parts out of Acrylic and the flexures out of stainless steel AISI316L, shown in Figure 2.17 (a) and (b). The input shuttle is deflected towards left and right with a displacement of $1mm$, Figure 2.17(d) and (c), to illustrate the motion and the deflection of the proposed compliant transmission mechanism. As can be seen, both movements yield in an upward displacement for the output shuttle and result in doubling the frequency of the input motion. As can be seen in Figure 2.17 (c) and (d), at least two fixed-fixed distributed flexures are always loaded in tension. Besides, two others are loaded in such that it results in an inflection point. This occurs since the fixed-fixed flexures are loaded with an applied end force and end moment acting in opposite directions.

CHARACTERIZATION AND PERFORMANCE

A customized test setup was built to measure the actuation stiffness and the input-output kinematics of the prototype, shown in Figure 2.18 (a). The force-deflection of the device is measured using a $10lbs$ force sensor *(FUTEK LSB200)*, where the nonlinearity, hysteresis, and non-repeatability of the force sensor imposes a maximum force measurement uncertainty of $\pm 0.05N$. The force sensor was mounted on a precision linear stage to provide a rectilinear input motion. A displacement of $1mm$ is applied to the input shuttle of the macro device, and the displacement of the output shuttle was simultaneously captured by the camera. The displacement was then analyzed using image processing, where it was detected with $100\mu m$ accuracy.

Moreover, a parametric finite element model (FEM) was created in ANSYS to analyze the proposed compliant frequency doubler transmission mechanism. The beam element based on Timoshenko beam theory *(BEAM188)* was used for the flexures, and rigid constraint elements *(MPC184)* for the rigid-bodies. The FEM model was evaluated while the maximum Von Mises stress was limited by $210MPa$. The other material specifications are $E = 183\ GPa$, and $\rho = 7.9\ gr/cm^3$ which were considered during modeling.

The force-displacement measurement is illustrated and compared to the FEM, and the PRBM in Figure 2.18 (b). The results show a nonlinear correlation between the actuation force and the input displacement, which can be explained by the nonlinear kinematics of the proposed eight-bar linkage. Clearly, by increasing the deflection the compliant transmission behaving as a linear, and softening spring, sequentially. Besides, it is shown that the results from the FEM and the experiment are in agreement. Although, there is a small discrepancy between these results, maximum 8.9%, which can be explained by the uncertainty in the force measurement. As can be seen, the PRBM force deflection result differs from the FEM and the experiment. The differences are primarily due to the initial angle α of the fixed-fixed flexures, which decreases the accuracy of the PRBM.

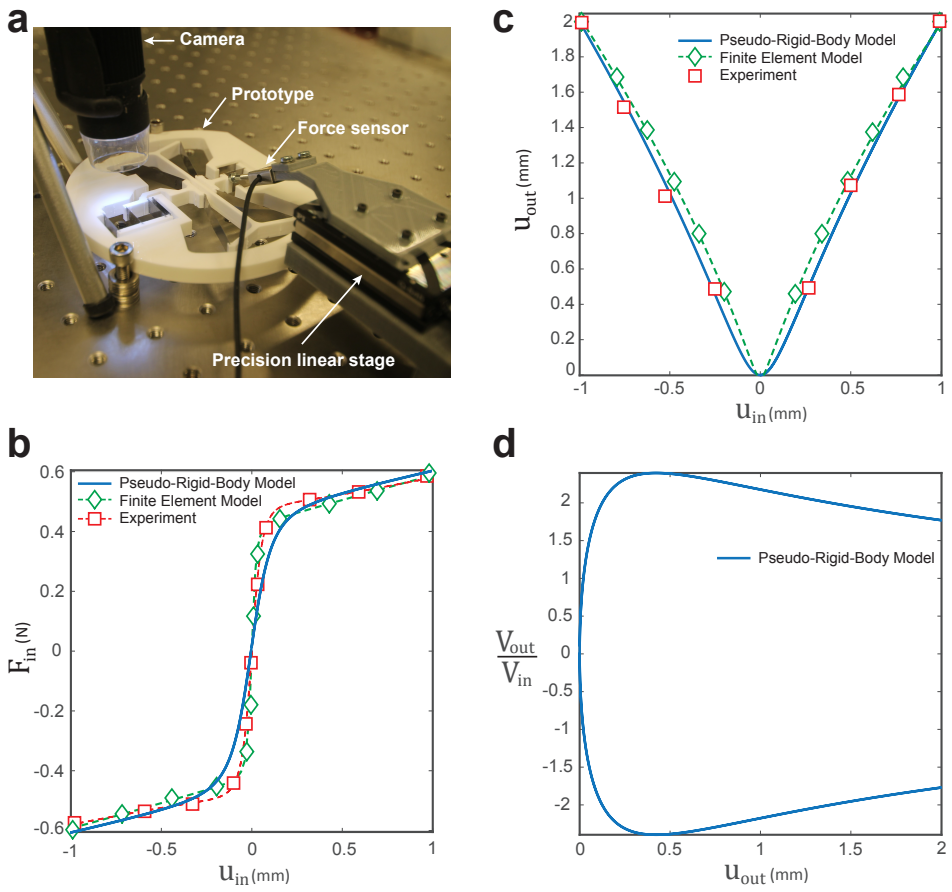

Figure 2.18: Characterization and performance of the compliant frequency and speed doubler transmission mechanism. (a) The experimental set-up to evaluate the actuation force and the input-output kinematics of the macro device. (b) Force-Displacement characteristics of the device. (c) The results for input-output displacement relationships, (d) The input-output velocity ratio versus the output displacement. The results are from Pseudo-Rigid-Body Model (PRBM), finite element model (FEM), and the experiment.

The optical displacement measurement, FEM, and the Pseudo-Rigid-Body Model (PRBM) show the same behavior and order of magnitude for the input-output kinematic relationship, shown in Figure 2.18 (c). As can be seen, the proposed compliant transmission mechanism doubles the input motion frequency, with an output displacement of $2mm$. The PRBM shows a maximum discrepancy of 14% and 10.5% with the FEM and experiment, respectively. The differences can be explained by the accuracy of the displacement measurement, with percentage uncertainty of 5%, and the accuracy of the PRBM and the values chosen for the characteristic radius factor and the stiffness coefficient.

Furthermore, the velocity ratio between the input and the output shuttles versus the output displacement, calculated from PRBM, is shown in Figure 2.18 (d). This illustrates

how the output velocity, and as a result the output force, varies at different position of the output shuttle due to the kinematic nonlinearity of the proposed eight-bar mechanism.

2.6. CONCLUSIONS

This chapter presented a new principle of movement to design compliant frequency doubler transmission mechanisms. The method exploits the first kind of singularity in planar mechanisms to double an input motion frequency. In the course of the chapter, two different frequency doubler building blocks were developed.

The first building block presented in this chapter was based on a four-bar planar mechanism. A monolithic frequency doubler transmission mechanism was designed and developed based on the compliant version of the double-slider four-bar mechanism, taking advantage of its singularity properties. Additionally, the input-output kinematics and force-deflection characteristic of the proposed compliant transmission mechanism were addressed by using the Pseudo-Rigid-Body model (PRBM). A compliant Frequency-Quadrupler transmission mechanism was designed and dimensioned as a case study. Furthermore, a micro-scale prototype was fabricated out of silicon using Deep Reactive Ion Etching (DRIE) for experimental evaluation. An optical displacement measurement in addition with a force-displacement measurement were performed to analyze the input-output kinematics and the actuation stiffness of the device, of which the results verify the PRBM and finite element models. By concatenating multiple of these mechanisms in a building block approach it was shown that higher frequency multiplication ratios can be achieved. However, this ratio was limited by the desired input-output velocity ratio, i.e. geometrical advantage ($G.A$). Since the frequency doubler building block based on a four-bar linkage is inherently limited to a $G.A. < 1$, it was not possible to achieve higher frequency multiplication ratios with a $G.A. > 1$.

Therefore, in the last section of this chapter, a novel eight-bar linkage was developed to double both the motion frequency and the $G.A$. An equivalent compliant frequency doubler was designed based on the proposed linkage using rigid-body replacement method. Different design parameters were addressed analytically, using PRBM, for the input-output kinematics and different stiffness characteristics. Furthermore, a macro-scale device was dimensioned and fabricated to experimentally evaluate the proposed compliant transmission mechanism.

The compliant transmission mechanisms developed in this chapter have nonlinear actuation stiffness and finite transmission stiffness. This can introduce dynamic problems and makes analysis more complicated. Therefore, a natural progression of this work is to analyze the dynamics and buckling instabilities of the proposed compliant transmission building blocks.

REFERENCES

[1] D. F. Machekposhti, J. L. Herder, G. Sémon, and N. Tolou, *A compliant micro frequency quadrupler transmission utilizing singularity,* Journal of Microelectromechanical Systems (2018).

[2] J. Huber, N. Fleck, and M. Ashby, *The selection of mechanical actuators based on performance indices,* in *Proceedings of the Royal Society of London A: Mathematical, Physical and Engineering Sciences*, Vol. 453 (The Royal Society, 1997) pp. 2185–2205.

[3] J. J. Sniegowski and E. J. Garcia, *Surface-micromachined gear trains driven by an on-chip electrostatic microengine,* IEEE Electron Device Letters **17**, 366 (1996).

[4] J.-S. Park, L. L. Chu, A. D. Oliver, and Y. B. Gianchandani, *Bent-beam electrothermal actuators-part ii: Linear and rotary microengines,* Journal of Microelectromechanical Systems **10**, 255 (2001).

[5] S. Kota, J. Hetrick, Z. Li, and L. Saggere, *Tailoring unconventional actuators using compliant transmissions: design methods and applications,* IEEE/ASME Transactions on mechatronics **4**, 396 (1999).

[6] S. Khan and G. Ananthasuresh, *Improving the sensitivity and bandwidth of in-plane capacitive microaccelerometers using compliant mechanical amplifiers,* Journal of Microelectromechanical Systems **23**, 871 (2014).

[7] L. L. Chu, J. A. Hetrick, and Y. B. Gianchandani, *High amplification compliant microtransmissions for rectilinear electrothermal actuators,* Sensors and Actuators A: Physical **97**, 776 (2002).

[8] C. J. Kim, S. Kota, and Y.-M. Moon, *An instant center approach toward the conceptual design of compliant mechanisms,* Journal of Mechanical Design **128**, 542 (2006).

[9] C. B. Pedersen and A. A. Seshia, *On the optimization of compliant force amplifier mechanisms for surface micromachined resonant accelerometers,* Journal of Micromechanics and Microengineering **14**, 1281 (2004).

[10] S.-C. Huang and G.-J. Lan, *Design and fabrication of a micro-compliant amplifier with a topology optimal compliant mechanism integrated with a piezoelectric microactuator,* Journal of Micromechanics and Microengineering **16**, 531 (2006).

[11] A. J. Nielson and L. L. Howell, *An investigation of compliant micro-half-pantographs using the pseudorigid body model,* Mechanics of structures and machines **29**, 317 (2001).

[12] J. Hetrick and S. Kota, *An energy formulation for parametric size and shape optimization of compliant mechanisms,* Journal of Mechanical Design **121**, 229 (1999).

[13] S. Kota, J. Hetrick, Z. Li, S. Rodgers, and T. Krygowski, *Synthesizing high-performance compliant stroke amplification systems for mems,* in *Micro Electro Mechanical Systems, 2000. MEMS 2000. The Thirteenth Annual International Conference on* (IEEE, 2000) pp. 164–169.

[14] G. S. Baichapur, H. Gugale, A. Maheshwari, S. D. Bhargav, and G. Ananthasuresh, *A vision-based micro-newton static force sensor using a displacement-amplifying compliant mechanism (dacm),* Mechanics Based Design of Structures and Machines **42**, 193 (2014).

[15] S. T. Smith, *Flexures: elements of elastic mechanisms* (CRC Press, 2014).

[16] M. Olfatnia, S. Sood, J. J. Gorman, and S. Awtar, *Large stroke electrostatic comb-drive actuators enabled by a novel flexure mechanism,* Journal of Microelectromechanical Systems **22**, 483 (2013).

[17] L. L. Howell, *Compliant mechanisms* (John Wiley & Sons, 2001).

[18] S. Awtar, A. H. Slocum, and E. Sevincer, *Characteristics of beam-based flexure modules,* Journal of Mechanical Design **129**, 625 (2007).

[19] K. R. Williams and R. S. Muller, *Etch rates for micromachining processing,* Journal of Microelectromechanical systems **5**, 256 (1996).

[20] K. R. Williams, K. Gupta, and M. Wasilik, *Etch rates for micromachining processing-part ii,* Journal of microelectromechanical systems **12**, 761 (2003).

[21] M. A. Hopcroft, W. D. Nix, and T. W. Kenny, *What is the young's modulus of silicon?* Journal of microelectromechanical systems **19**, 229 (2010).

[22] N. Tolou, V. A. Henneken, and J. L. Herder, *Statically balanced compliant micro mechanisms (sb-mems): Concepts and simulation,* in *Proceedings of the ASME Design Engineering Technical Conferences & Computers and Information in Engineering Conference, Montreal, Canada, Aug* (2010) pp. 15–18.

[23] K. Hoetmer, G. Woo, C. Kim, and J. Herder, *Negative stiffness building blocks for statically balanced compliant mechanisms: design and testing,* Journal of Mechanisms and Robotics **2**, 041007 (2010).

[24] R. Jones and I. Young, *Some parasitic deflexions in parallel spring movements,* Journal of Scientific Instruments **33**, 11 (1956).

[25] W. C. Tang, T.-C. Nguyen, and R. T. Howe, *Laterally driven polysilicon resonant microstructures,* in *Micro Electro Mechanical Systems, 1989, Proceedings, An Investigation of Micro Structures, Sensors, Actuators, Machines and Robots. IEEE* (IEEE, 1989) pp. 53–59.

[26] B. Krijnen and D. M. Brouwer, *Flexures for large stroke electrostatic actuation in mems,* Journal of micromechanics and microengineering **24**, 015006 (2013).

[27] D. M. Brouwer, B. De Jong, and H. Soemers, *Design and modeling of a six dofs mems-based precision manipulator,* Precision Engineering **34**, 307 (2010).

[28] S. T. Smith, *Foundations of ultra-precision mechanism design*, Vol. 2 (CRC Press, 2003).

[29] R. M. Panas and J. B. Hopkins, *Eliminating underconstraint in double parallelogram flexure mechanisms,* Journal of Mechanical Design **137**, 092301 (2015).

[30] L. Saggere, S. Kota, and S. Crary, *New design for suspension of linear microactuators,* in *ASME* (1994).

[31] D. F. Machekposhti, N. Tolou, and J. L. Herder, *A review on compliant joints and rigid-body constant velocity universal joints toward the design of compliant homokinetic couplings,* Journal of Mechanical Design **137**, 032301 (2015).

3

COMPLIANT FREQUENCY DOUBLER TRANSMISSION UTILIZING BUCKLING

The previous chapter introduced frequency doubler transmission mechanisms with nonlinear kinematics. For some applications, the kinematic nonlinearities limit the maximum frequency multiplication ratio which can be achieved by concatenating the frequency doubler transmission building blocks. This is imposed by the fact that the nonlinearity can be propagated for higher multiplication ratios and causes a non-uniform force transmission. This chapter presents a new method for the design of frequency doubler transmission mechanisms with a linear kinematics. The proposed method is based on switching between two instant center of rotations by utilizing the buckling in the beam. Section 3.2 presents the methodology used in this chapter. Furthermore, a micro compliant design was dimensioned and fabricated in Section 3.3 as a case study to validate the analytical model and the finite-element model (FEM) with the experimental evaluations.

Parts of this chapter have been submitted to *Applied Physics Letters*.

3.1. INTRODUCTION

Gears are the workhorse transmission concept in mechanical engineering. They have a long-standing history, from the Antikythera mechanism, one of the oldest geared instrument (80 BC, Greece), which was used to predict astronomical positions [1, 2], to current Micro-Electro-Mechanical-Systems (MEMS)-based gears which have been applied in micro engines [3, 4].

The most common functions include torque transformation which is normally quantified by mechanical advantage (M.A.), i.e. the ratio of output torque over input torque; and angular velocity transformation which is normally quantified by geometrical advantage (G.A.), i.e. the ratio of output angular velocity over input velocity. Another key function of gears is frequency multiplication, considering that revolutions per time unit from an input shaft are often converted to reciprocating motion at the output. An everyday example is present in a combustion engine, where timing of the valves is done by a gear transmission of ratio 2, and the final conversion to reciprocating motion by a cam mechanism. In this study, this timing function will be referred to as frequency multiplication, characterized analogue to the previous functions by a metric that we shall term frequency advantage (F.A.), i.e. the ratio of output frequency over input frequency.

Mechanical frequency and speed multiplier mechanisms are necessary for a variety of applications, including tailoring micro actuators [5], vibration energy harvesting [6, 7], quantum cascade lasers [8], mass sensing [9], bio-sensing [10], and motion sensors and accelerometers [11, 12]. Furthermore, integration of frequency multiplier transmission mechanisms on a local mechanical resonator can approach the limits on position and displacement measurements, which are ultimately limited by quantum mechanics [13, 14].

Over the centuries, the working principle of gear systems has essentially remained the same. They consist of discrete components which are engaged and connected by rolling contacts and suspended by rotational hinges (revolute joints). This gives rise to numerous drawbacks and source of uncertainties including backlash, friction, wear, poor mechanical efficiency, and micro stiction [15, 16]. Apart from the need for assembly and lubrication, it is difficult and it is not size and cost efficient to integrate the classical gear transmissions with the MEMS/NEMS-based actuating and sensing schemes. Consequently, in vacuum (e.g. high-tech semiconductor industry, space), in biological environments (e.g. surgical instruments), or any situation where maintenance is to be avoided, gear systems are unsuitable.

In such cases, compliant mechanisms can be used advantageously. These mechanisms move due to deformation of slender parts, thus avoiding the relative motion of rigid parts in conventional (linkage or gear) mechanisms [17–25]. As a result, friction and backlash are absent, and there is no need for lubrication or assembly. However, one key challenge is that their range of motion is severely limited: compliant joints cannot do full-cycle rotation as revolute joints (e.g. ball bearings) can. As a result, to date, no solutions for precise frequency multiplication by compliant mechanisms have been reported.

In this chapter, we show how in spite of the fundamental limitation of motion range of compliant mechanisms, a monolithic frequency multiplier is conceived, designed and tested. We demonstrate a new movement with linear kinematics which utilizes elastic

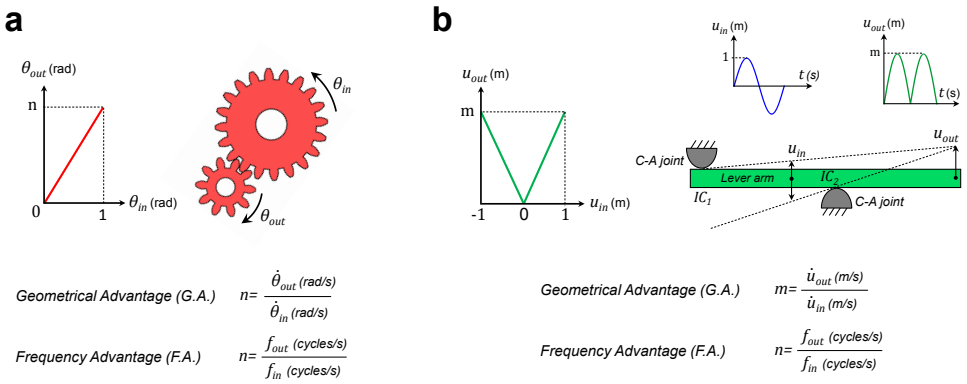

Figure 3.1: Movement principles. (a) A pair of classical gears, where the input-output velocity and frequency ratios are dependent and representing the same values, although with different units. (b) The proposed movement for the frequency and speed multiplication with rectilinear input-output motion, where the input-output velocity and frequency ratios are independent.

deformation and buckling of beams to double motion frequency. This new type of transmission mechanisms makes it possible to adapt the frequency and speed characteristics of MEMS/NEMS-based local oscillators, sensors, and actuators with an integrated micro mechanism.

The organization of this chapter is as follows: the design methodology the theoretical model are introduced and discussed in Section 3.2. A design example was dimensioned and fabricated as a case study and presented in Section 3.3. Besides, experiments and finite element model (FEM) are conducted to cross validate the characteristics of the proposed compliant transmission mechanism. Furthermore, the conclusions based on the results are given in Section 3.4.

3.2. METHODOLOGY

3.2.1. MOVEMENT PRINCIPLE AND DEVICE DESIGN

We propose a new movement for frequency multiplication, illustrated in Figure. 3.1 (b), as an alternative to classical gears, as shown in Figure. 3.1 (a). As can be seen in Figure. 3.1 (b), a finite travel range movement with linear kinematics is envisioned to double the frequency of a reciprocating input motion. Two contact-aided (C-A) joints on opposite side of the input displacement vector u_{in} represent two instant centers of rotation, IC_1 and IC_2, between the lever arm and ground. Therefore, according to the input and output displacement vectors, u_{in} and u_{out}, a back-and-forth input motion transmits a forward output motion and results in doubling motion frequency.

A compliant and monolithic design for frequency doubling is generated based on the proposed movement, as shown in Figure. 3.2(a). Different compliant joints in the design allow for the desired relative motions between rigid parts by elastic deformation of flexible segments. The arrangement of the beams imposes constraints and leaves the desired degrees of freedom (DoF) to follow the prescribed kinematics. The contact-aided joints are replaced with two buckle-sensitive beams with a length of L_{b_1} and L_{b_2}. They provide

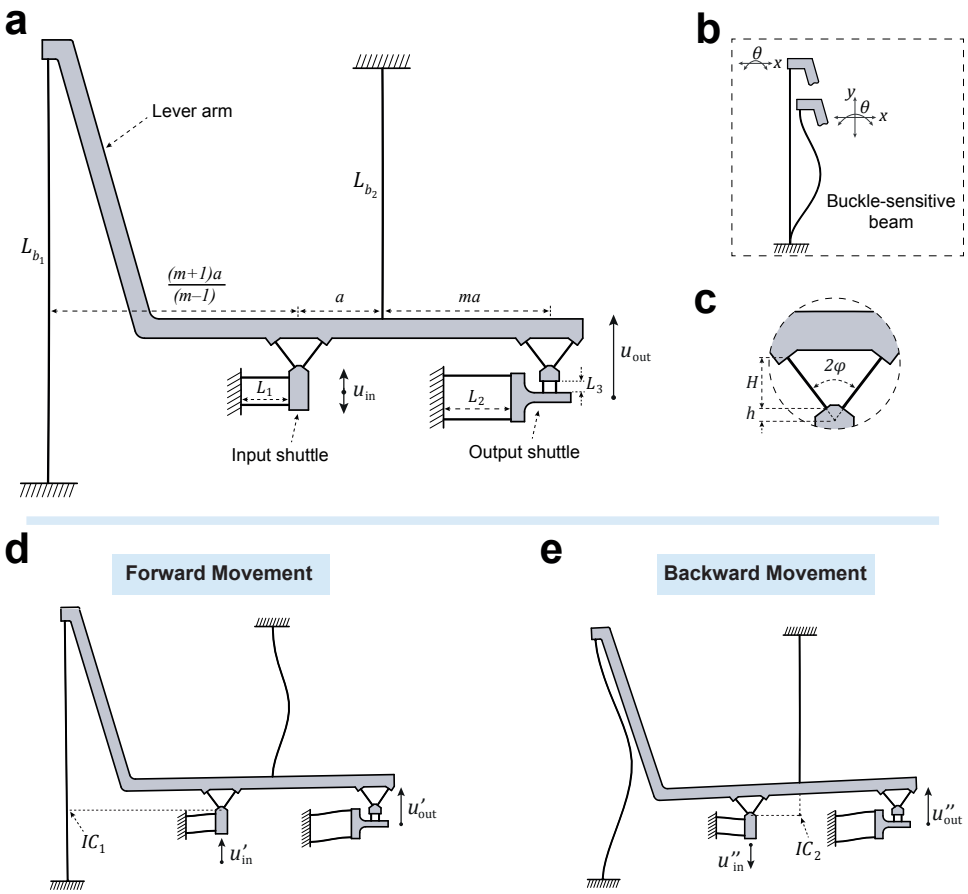

Figure 3.2: Design of the monolithic frequency doubler transmission. (a) Schematic representation and geometric parameters of the design. (b) The buckle-sensitive beams which are employed in the design as the compliant reconfigurable joints. (c) The geometric parameter of the double blade rotary pivot used in the design as a compliant rotational joint. (d) Forward movement with a displacement of u'_{in}. (e) Backward movement with a displacement of u''_{in}.

two DoF (rotation and translation) when a tensile force is applied, and undergo buckling and relieve all planar kinematic constraints when a compressive force is applied, shown in Figure. 3.2(b). Thus, the buckle-sensitive beams constitute compliant reconfigurable joints. The rectilinear motion of the input and the output shuttles is supported via the parallelogram flexures with a length of L_1, L_2, and L_3, respectively. Two double blade rotary pivots, shown in Figure. 3.2(c), are used to provide a relative rotation between the lever arm and both shuttles.

Two cycles of the movement of the proposed compliant design are shown in Figure. 3.2 (d) and (e). As can be seen, for a forward movement of the input shuttle, the buckle-sensitive beam in the right side of the input buckles and the lever arm rotates around the virtual instant center of rotation, IC_1, which is along the left buckle-sensitive beam.

This results in an upward movement of the output shuttle with a displacement of u'_{out}. Likewise, the lever arm rotates around the virtual instant center of rotation, IC_2, while a downward motion is subjected to the input. As a consequence, the buckle-sensitive beam on the left side of the input shuttle undergoes buckling and results in yet another upward movement of the output, u''_{out}. Since the back-and-forth movement of the input always causes upward displacements for the output, the mechanism doubles the input motion frequency.

As shown in Figure. 3.2 (a), the position of the buckle-sensitive beams respect to the input and output shuttles can be chosen in such a way that the instantaneous geometrical advantage, m, for both cycles are equal and can be represented as

$$\frac{u'_{out}}{u'_{in}} = \frac{u''_{out}}{u''_{in}} = m. \tag{3.1}$$

3.2.2. PSEUDO-RIGID-BODY MODEL

The Pseudo-Rigid-Body Model (PRBM) for both cycles are generated, illustrated in Figure. 3.3 (a) and (b), to determine the stiffness characteristics of the proposed compliant micro frequency and speed multiplier transmission mechanism. The parallelogram flexures indicated with length L_1, L_2, and L_3, in the compliant design are replaced by sliders and associated translational stiffness coefficients K_1, K_2, and K_3, respectively, which can be formulated as

$$K_j = \frac{24EI}{{L_j}^3}, \quad j = \{1,2,3\}. \tag{3.2}$$

where, E is the Young's Modulus of the material, and I is the second moment of area. The second moment of area for a beam with rectangular cross section (I_r) and a trapezoidal cross section (I_t) can be written by

$$I_r = \frac{1}{12} w t^3, \quad I_t = \frac{1}{48} w (t_1 + t_2)\left(t_1^2 + t_2^2\right). \tag{3.3}$$

where, w is the out of plane thickness, t is the in-plane thickness of the beam with a rectangular cross-section, and t_1 and t_2 are the top and bottom layer thickness of the beam with a trapezoidal cross-section, respectively.

The double blade rotary pivot is modeled as a pin joint with a torsional spring K_4 located at its virtual center of rotation, where the stiffness constant is given by [26]

$$K_4 = \frac{8EI(H^2 + Hh + h^2)cos\varphi}{(H-h)^3}. \tag{3.4}$$

The buckle-sensitive beams can be considered as a fixed-fixed flexible segment when they are under tensile forces. This can kinematically be represented as a binary pseudo-rigid link with the length of γL_{b_1} and γL_{b_2} associated with the torsional springs K_6 and K_5 at hinges, respectively. The torsional spring constant K_5 and K_6 for a fixed-fixed segment is given by [17]

$$K_5 = 2\gamma K_\Theta \frac{EI}{L_{b_2}}, \quad K_6 = 2\gamma K_\Theta \frac{EI}{L_{b_1}}, \tag{3.5}$$

where $\gamma = 0.85$ is the characteristic radius factor, and $K_\Theta = 2.65$ is the stiffness coefficient.

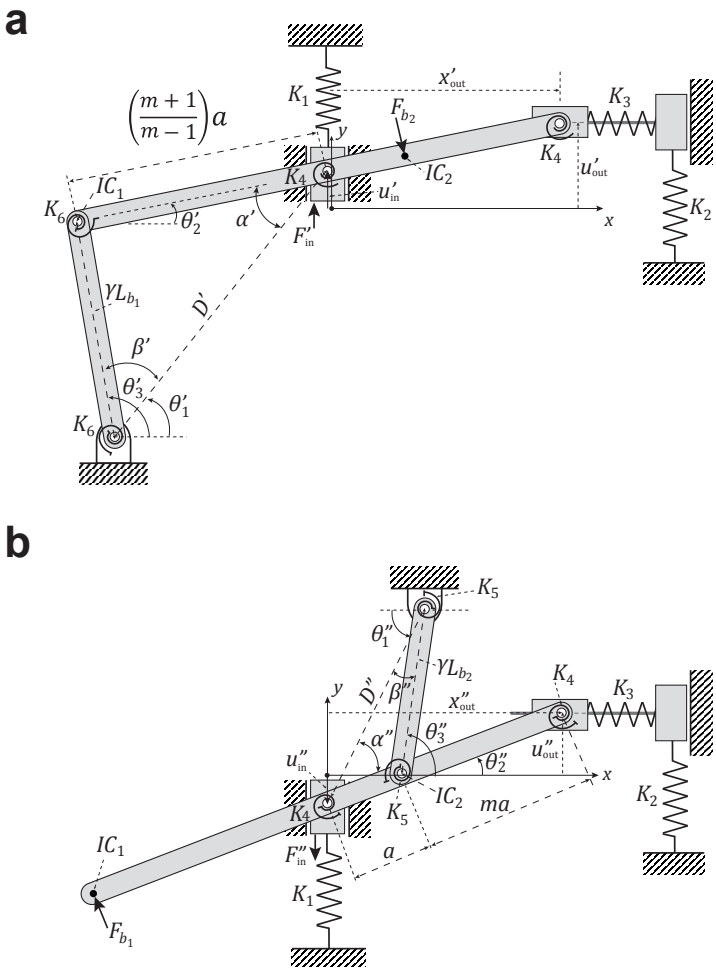

Figure 3.3: The Pseudo-Rigid-Body Model (PRBM) of the monolithic frequency doubler transmission. (a) The PRBM for a forward movement with a displacement of u'_{in}. (b) The PRBM for a forward movement with a displacement of u''_{in}.

Since the buckled beam can not pose any kinematic constraint, they are replaced by their equivalent buckling forces, F_{b_2} and F_{b_1}, in the corresponding PRBM. The buckling force can be estimated by the classical Euler–Bernoulli beam theory and for the fixed-fixed beams can be expressed as

$$F_{b_1} = \frac{4\pi^2 EI}{{L_{b_1}}^2}, \qquad F_{b_2} = \frac{4\pi^2 EI}{{L_{b_2}}^2}. \tag{3.6}$$

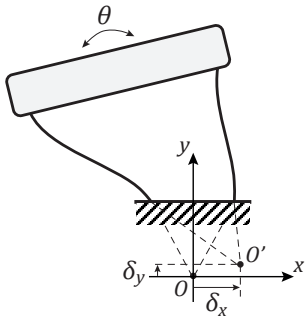

Figure 3.4: Center of rotation drift associated by rotation for a double blade rotary pivot.

KINEMATICS

The kinematics of the compliant design are studied by using the PRBM. As can be seen in Figure. 3.4, due to the distributed compliance of the double blade rotary pivot, the virtual center of rotation deviates from its initial position, point O moves to point O', with the association of the rotation. This drift in the axis of rotation, denoted as the offset δ, alters the original rigid-body kinematics by changing the effective length of the lever arms. This drift, also called axis drift, depends on the amount of rotation θ and the geometry of the joint, which for the double blade rotary pivot can be given by [26]

$$\begin{aligned} \delta_x &= HB_3 \sin\theta, \\ \delta_y &= HB_3 (n - \cos\theta), \end{aligned} \tag{3.7}$$

where,

$$\begin{aligned} B_3 &= 1 - \tan\varphi \sqrt{\frac{B_2}{B_1} - 1}, \\ B_2 &= \frac{(1-n)^2}{\sin^2\varphi}, \\ B_1 &= 1 + n^2 - 2n\cos\theta, \\ n &= \frac{H + 8h}{9H}. \end{aligned} \tag{3.8}$$

In the proposed transmission mechanism, only the x component of the axis drift, δ_x, leads to a deviation from original linear input-output kinematics, shown in Figure. 3.5. As can be seen, δ'_x and δ''_x moves towards right since the rotations at the double blade rotary pivot, θ'_2 and θ''_2 , are counterclockwise in both cycles. Therefore, the instantaneous geometrical advantage of the proposed rigid-body mechanism, Eq. 3.1, should be

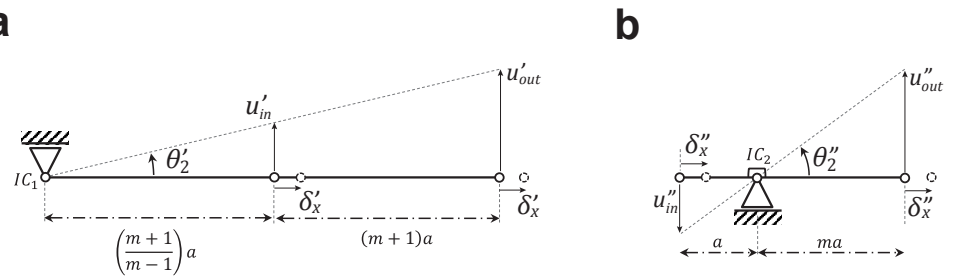

Figure 3.5: The influence of the axis drift of the double blade rotary pivot on the effective length of the lever arms. (a) For a forward movement with a displacement of u'_{in}, and (b) for a downward movement with a displacement of u''_{in}.

rewritten for the compliant design, and can be formulated as

$$\frac{u'_{out}}{u'_{in}} = \left(\frac{\left(\frac{m+1}{m-1}\right)a + (m+1)\,a + \delta'_x}{\left(\frac{m+1}{m-1}\right)a + \delta'_x} \right),$$
$$\frac{u''_{out}}{u''_{in}} = \left(\frac{ma + \delta''_x}{a - \delta''_x} \right). \tag{3.9}$$

where, δ'_x and δ''_x are the x component of the axis drifts associated by the double blade rotary pivot and can be driven by their corresponding rotation θ'_2 and θ''_2, respectively.

Consider two rigid-body mechanisms with the link length and angles as shown in the PRBM, Figure. 3.3, the angles θ'_2 and θ''_2 can be expressed as

$$\theta'_2 = \theta'_3 - \alpha' - \beta',$$
$$\theta''_2 = \theta''_3 - \alpha'' - \beta'', \tag{3.10}$$

where,

$$\theta'_3 = \theta'_1 + \beta',$$
$$\theta''_3 = \theta''_1 + \beta'', \tag{3.11}$$

and,

$$\theta'_1 = \arctan\left(\frac{\left(\gamma L_{b_1} + u'_{in}\right)(m-1)}{(m+1)\,a} \right),$$
$$\theta''_1 = \arctan\left(\frac{\gamma L_{b_2} + u''_{in}}{a} \right). \tag{3.12}$$

The law of cosines can be applied to determine the internal angles α', β', α'', and β'',

as

$$\alpha' = \arccos\left(\frac{a^2\left(\frac{m+1}{m-1}\right)^2 + \left(D'^2 - \gamma^2 {L_{b_1}}^2\right)}{2D'a\left(\frac{m+1}{m-1}\right)}\right),$$

$$\beta' = \arccos\left(\frac{\left(D'^2 + \gamma^2 {L_{b_1}}^2\right) - a^2\left(\frac{m+1}{m-1}\right)^2}{2\gamma L_{b_1} D'}\right), \tag{3.13}$$

$$\alpha'' = \arccos\left(\frac{a^2 + D''^2 - \gamma^2 {L_{b_2}}^2}{2aD''}\right),$$

$$\beta'' = \arccos\left(\frac{D''^2 + \gamma^2 {L_{b_2}}^2 - a^2}{2D''\gamma L_{b_2}}\right),$$

where, the length of D' and D'' are

$$D' = \sqrt{\left(\frac{m+1}{m-1}\right)^2 a^2 + \left(\gamma L_{b_1} + u'_{in}\right)^2},$$
$$D'' = \sqrt{a^2 + \left(\gamma L_{b_2} + u''_{in}\right)^2}. \tag{3.14}$$

The lateral displacement of the output shuttle in both modes X'_{out} and X''_{out} can be given by

$$X'_{out} = a(m+1)\cos\theta'_2$$
$$X''_{out} = a(m+1)\cos\theta''_2. \tag{3.15}$$

ACTUATION FORCE

The input actuation forces for both cycles, F'_{in} and F''_{in} for upward and downward input motion, respectively, can be given by applying the virtual work principle, which results in

$$\begin{aligned} F'_{in} = {} & K_1 u'_{in} + h_{11} F_{b_2} + K_2 h_{12} u'_{out} + 2K_4 h_{14}\left(\theta'_2\right) + K_3 h_{13}\left(x'_{out} - 3a\right) \\ & + K_6 h_{15}\left(\theta'_3 - \frac{\pi}{2}\right) + K_6\left(h_{15} - h_{14}\right)\left(\theta'_3 - \theta'_2 - \frac{\pi}{2}\right), \end{aligned} \tag{3.16}$$

and,

$$\begin{aligned} F''_{in} = {} & K_1 u''_{in} + h_{21} F_{b_1} + K_2 h_{22} u''_{out} + 2K_4 h_{24}\left(\theta''_2\right) + K_3 h_{23}\left(x''_{out} - 3a\right) \\ & + K_5 h_{25}\left(\theta''_3 - \frac{\pi}{2}\right) + K_5\left(h_{25} - h_{24}\right)\left(\theta''_3 - \theta''_2 - \frac{\pi}{2}\right). \end{aligned} \tag{3.17}$$

where, h_{ij} are kinematic coefficients, and can be determined through analytical velocity analysis of the PRBM

$$\begin{aligned}
h_{11} &= \frac{\delta u'_{IC_2}}{\delta u'_{in}} = \frac{2m}{m+1}, \\
h_{12} &= \frac{\delta u'_{out}}{\delta u'_{in}} = m, \\
h_{13} &= \frac{\delta x'_{out}}{\delta u'_{in}} = \frac{(m-1)\sin\theta'_2\cos\theta'_3}{\sin(\theta'_3-\theta'_2)}, \\
h_{14} &= \frac{\delta\theta'_2}{\delta u'_{in}} = -\frac{(m-1)\cos\theta'_3}{a(m+1)\sin(\theta'_3-\theta'_2)}, \\
h_{15} &= \frac{\delta\theta'_3}{\delta u'_{in}} = \frac{1}{\gamma L_{b_1}(\sin\theta'_3-\cos\theta'_3\tan\theta'_2)}.
\end{aligned} \tag{3.18}$$

And,

$$\begin{aligned}
h_{21} &= \frac{\delta u''_{IC_1}}{\delta u''_{in}} = -\frac{2m}{m-1}, \\
h_{22} &= \frac{\delta u''_{out}}{\delta u''_{in}} = -m, \\
h_{23} &= \frac{\delta x''_{out}}{\delta u''_{in}} = -\frac{(m+1)\sin\theta''_2\cos\theta''_3}{\sin(\theta''_3-\theta''_2)}, \\
h_{24} &= \frac{\delta\theta''_2}{\delta u''_{in}} = \frac{\cos\theta''_3}{a\sin(\theta''_3-\theta''_2)}, \\
h_{25} &= \frac{\delta\theta''_3}{\delta u''_{in}} = -\frac{1}{\gamma L_{b_2}(\sin\theta''_3-\cos\theta''_3\tan\theta''_2)}.
\end{aligned} \tag{3.19}$$

Therefore, for given kinematics and considering a constant beam thickness over the compliant design, a symmetric actuation force-deflection profile can be established by satisfying

$$L_{b_1} = \sqrt{m+1}L_{b_2}. \tag{3.20}$$

3.3. DEVICE FABRICATION AND CHARACTERIZATION

A MEMS device was fabricated in silicon using Deep Reactive Ion Etching (DRIE), shown in Figure. 3.6 (a), where the design was etched on a silicon wafer with a thickness of $w = 525\mu m$. The device was made for experimental evaluation of the design, and to verify the PRBM and the finite element model (FEM) for the actuation stiffness and the input-output kinematics. The design parameters were optimized by using the proposed PRBM for linear input-output kinematics and a symmetric actuation force, where the set of design parameters is summarized in Table 3.1. A thickness of $t = 30\mu m$ is considered for all the flexures in the design. Besides, a small initial curvature, with radius of 1000 mm, was implemented for both buckle-sensitive beams to ensure the buckling direction of the beams, and avoid the solution convergence into higher order buckling modes in the FEM.

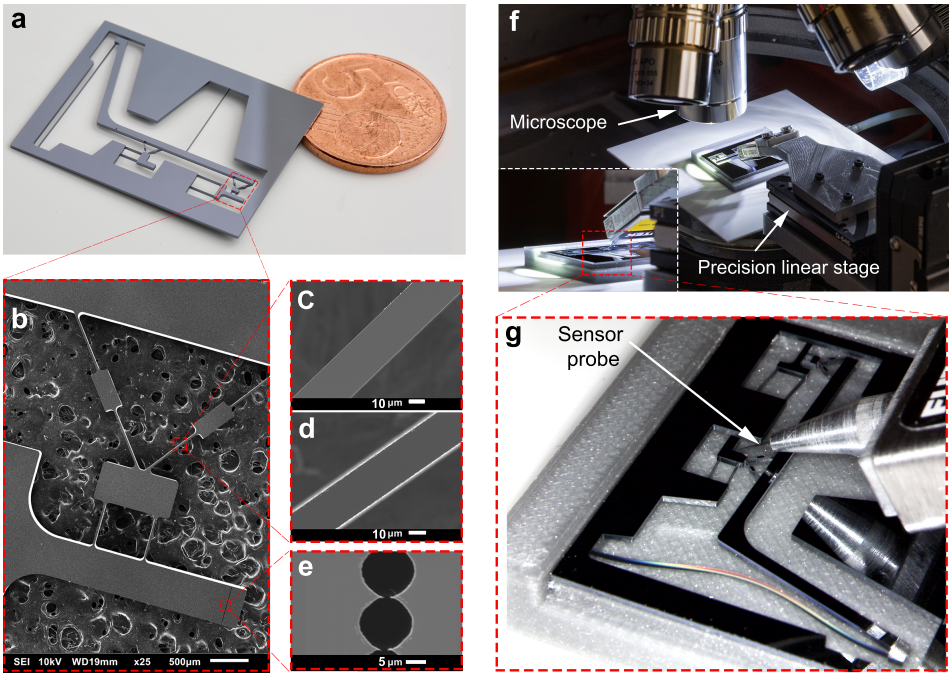

Figure 3.6: MEMS device fabrication, characterization, and experimental set-up. (a) Fabricated MEMS device on silicon using deep reactive ion etching (DRIE). (b) The scanning electron microscopy (SEM) image and zoomed-in view of output shuttle. (c) The SEM of the top thickness of the flexures $t_1 = 18.75\ \mu m$. (d) The SEM of the bottom thickness of the flexures $t_2 = 24.25\ \mu m$. (e) The SEM of markers used to calibrate the optical displacement measurement, with a minimum feature size of 1.5 μm. (f) Experimental set-up to evaluate the actuation force, and the input-output kinematics of the MEMS transmission. (g) A detailed view of actuated MEMS transmission, corresponding to the backward movement.

The designed and dimensioned compliant embodiment is composed of flexures with a rectangular cross-section. However, the released fabricated device got a trapezoidal cross section due to the non-constant etching rate of DRIE precess [27, 28]. Therefore, a scanning electron microscope (SEM) measurement was conducted to find the thickness of the flexures at the top and bottom layers, as shown in Figure. 3.6 (c) and (d). The results are then applied to the FEM and the PRBM by creating a customized cross-section based on the SEM results. An experimental set-up was constructed for testing the actuation stiffness and the input-output kinematics of the silicon device, shown in Figure. 3.6 (f) and (g). The force deflection of the devices is measured using a $20 gram$ force sensor (FUTEK LSB200) with a resolution of 50 μN. The force transducer was mounted on a precision linear stage (PI Q-545), with a resolution of 1 nm and minimum incremental motion of 6 nm, to provide a rectilinear input motion. A displacement of $u'_{in} = u''_{in} = 100\ \mu m$ was applied to the input shuttle of the micro device, while the movement of the output shuttle was simultaneously captured by an optical microscope (Keyence VHX-1000E). The output displacement was then analyzed using image processing, where the measurement was calibrated by the markers with a minimum feature size of 1.5 μm on the

Parameters	m	a	L_{b_1}	L_{b_2}	L_1	L_2	L_3	H	h	φ
Values	2	4.3 mm	22.52 mm	13 mm	2.5 mm	3.5 mm	0.6 mm	1.8 mm	0.05 mm	37.5°

Table 3.1: Design parameters for the monolithic frequency doubler transmission mechanism.

output shuttles. The markers were implemented on the device during DRIE process and later measured by the SEM, shown in Figure. 3.6 (e). This results in a displacement measurement with an accuracy of 100 nm.

A FEM model was made in ANSYS to analyze the compliant frequency doubler transmission. The beam element based on the Timoshenko beam theory *(BEAM188)* was used for the flexures, and rigid constraint elements *(MPC184)* for the rigid-bodies. Moreover, an orthotropic material properties for a standard (100) silicon wafer [29] were considered to investigate the device further: $E_x = E_y = 169\ GPa$, $E_z = 130\ GPa$, $\nu_{yz} = 0.36$, $\nu_{zx} = 0.28$, $\nu_{xy} = 0.064$, $G_{yz} = G_{zx} = 79.6\ GPa$, $G_{xy} = 50.9\ GPa$, $\rho = 2330\ kg/m^3$. The FEM was evaluated while the maximum Von Mises stress was limited by the tensile yield strength of the silicon, 200 MPa. This value is selected far below the maximum yield strength of the silicon, which is about 6 GPa based on the prior art. This was an industrial constraint which was considered to prevent any risk of crack growth in silicon crystal of the proposed compliant transmission mechanism.

The optical displacement measurement, the FEM, and the PRBM show the same behaviour and order of magnitude for the input-output kinematics, as shown in Figure. 3.7(a). The proposed compliant mechanism doubles the input motion frequency as well as velocity for an input displacement of $\pm 100\ \mu m$. The design parameters are optimized using the PRBM to keep linear input-output kinematics with a velocity ratio of $m = 2$. However, a maximum discrepancy of 0.15% and 0.2% with the PRBM was predicted and observed, for the input-output velocity ratio, by the FEM and the experiment, respectively, which can be explained by the accuracy of the PRBM.

The results for the force-displacement characteristic obtained by the experiment, the FEM, and the PRBM are depicted in Figure. 3.7(b). A similar trend in actuation stiffness for both forward and backward input motion is observed. As can be seen, the first part of the stiffness behaviour is associated with Euler-Buckling load caused by the buckle-sensitive beams, with a magnitude of 22.35 mN from PRBM. And the second part follows with a linear stiffness behaviour, corresponds to the spring forces from other flexural joints in the mechanism, in addition to a stable post-buckling force from the buckle-sensitive beams. Moreover, the results from FEM and experiment show 21.2% and 30.4% decrease in the buckling force predicted by the PRBM, respectively. This can be explained by the accuracy of the classical Euler-Beam theory, and the effect of the initial curvature of the beams, as a geometrical imperfection, which was not considered in the PRBM. Moreover, the discrepancy between the experimental results and the FEM can be explained by other imperfection factors and uncertainty in thickness measurement, which is about $\pm 0.8\ \mu m$. A decrease in thickness t of 0.2 μm for buckle-sensitive beams with an initial average thickness of 21.5 μm results in approximately 2.77% decrease in buckling force.

The fundamental working principle of the proposed monolithic frequency doubler

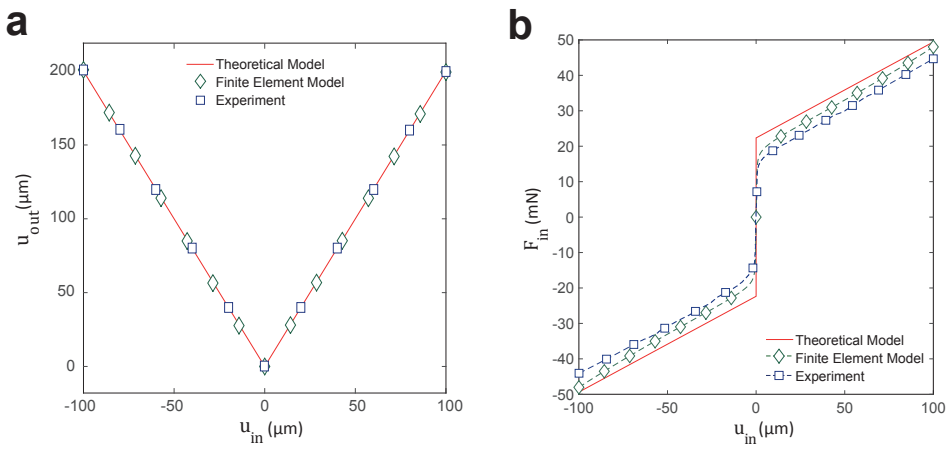

Figure 3.7: MEMS device performance; Measured and calculated results. (a) The input-output displacement relationship shows a linear kinematic. A sinusoidal input displacement with an amplitude of 100 μm resulted in an output displacement of 200 μm with twice of input frequency. (b) Actuation stiffness characteristic of the MEMS device, where shows a symmetrical performance for both cycles. The maximum actuation force of 44.8 mN is measured at the input shuttles for both forward and backward movement.

transmission, the theoretical as well as finite element model, were validated on a MEMS device. According to the kinematics, the input-output velocity ratio m is linear, a maximum discrepancy of 0.2%, and can be selected independently from frequency ratio in the design. Therefore, this level of kinematic linearity enables to design monolithic frequency multiplier transmission mechanism with the ratio of 2^r, by concatenating r number of proposed frequency doubler device, where $r = 1, 2, ..., N$.

Another important aspect of the proposed transmission mechanism is the actuation stiffness of the compliant design. As can be seen in Figure. 3.7(b), the proposed movement is associated with an actuation motion stiffness. However, this is strain energy stored in a monolithic structure, which is a conservative energy and can be transferred to another source of potential energy, and vice versa. Therefore, static balancing principle and geometric anti-spring technique can be used to reduce the actuation stiffness of the MEMS device. For instance, a preloaded beam, which can provide a negative stiffness, can be added along the input shuttle to cancel out the actuation force associated with the internal stiffness of the MEMS device.

The proposed compliant transmission mechanism provides puling force at the output within the acceptable stress limit of the constituted material, however, the pushing force by the output shuttle is below the critical buckling load of the buckle-sensitive beams. Therefore, the future developments would entail extending the presented approach for the transmission of pushing forces, for instance, using a mirrored combination of the proposed compliant design. Moreover, there are some limitations on the maximum multiplication ratio which can be achieved by using the proposed monolithic transmission mechanism that are dictated by the dynamics and operational frequency. A natural progression of this work is to analyze and design for dynamics.

3.4. CONCLUSION

This chapter contends to be the first to report a monolithic and contact-less frequency and speed multiplier transmission mechanism, functionality equivalent with classical gears. We employ elastic deformation and buckling of slender segments in an embodiment that exhibits a precise and linear transmission of frequency and deflection rate. The input-output kinematics and force-deflection characteristics of the proposed compliant transmission mechanism were described by theoretical modeling, a finite element model, and validated experimentally in a silicon MEMS device. The presented results lay the foundation for the development of new types of transmission mechanisms, suitable for on-chip integration, to adapt the frequency and speed requirements of MEMS/NEMS-based oscillators, sensors and actuators.

REFERENCES

[1] D. de Solla Price, *Gears from the greeks. the antikythera mechanism: a calendar computer from ca. 80 bc,* Transactions of the American Philosophical Society , 1 (1974).

[2] T. Freeth, Y. Bitsakis, X. Moussas, J. H. Seiradakis, A. Tselikas, H. Mangou, M. Zafeiropoulou, R. Hadland, D. Bate, A. Ramsey, *et al.*, *Decoding the ancient greek astronomical calculator known as the antikythera mechanism,* Nature **444**, 587 (2006).

[3] J. J. Sniegowski and E. J. Garcia, *Surface-micromachined gear trains driven by an on-chip electrostatic microengine,* IEEE Electron Device Letters **17**, 366 (1996).

[4] K. Deng, M. Mehregany, and A. S. Dewa, *A simple fabrication process for polysilicon side-drive micromotors,* Journal of microelectromechanical systems **3**, 126 (1994).

[5] D. J. Bell, T. Lu, N. A. Fleck, and S. M. Spearing, *Mems actuators and sensors: observations on their performance and selection for purpose,* Journal of Micromechanics and Microengineering **15**, S153 (2005).

[6] F. Cottone, H. Vocca, and L. Gammaitoni, *Nonlinear energy harvesting,* Physical Review Letters **102**, 080601 (2009).

[7] Q. Shi, T. Wang, and C. Lee, *Mems based broadband piezoelectric ultrasonic energy harvester (pueh) for enabling self-powered implantable biomedical devices,* Scientific reports **6**, 24946 (2016).

[8] B. S. Williams, *Terahertz quantum-cascade lasers,* Nature photonics **1**, 517 (2007).

[9] Y. Yang, C. Callegari, X. Feng, K. Ekinci, and M. Roukes, *Zeptogram-scale nanomechanical mass sensing,* Nano letters **6**, 583 (2006).

[10] J. H. Lee, K. S. Hwang, D. S. Yoon, J. Y. Kang, S. K. Kim, and T. S. Kim, *Direct electrical measurement of protein–water interactions and temperature dependence using piezoelectric microcantilevers,* Advanced Materials **23**, 2920 (2011).

[11] M. O. Pasquet, M. Tihy, A. Gourgeon, M. N. Pompili, B. P. Godsil, C. Léna, and G. P. Dugué, *Wireless inertial measurement of head kinematics in freely-moving rats,* Scientific reports **6**, 35689 (2016).

[12] A. Gesing, F. Alves, S. Paul, and J. Cordioli, *On the design of a mems piezoelectric accelerometer coupled to the middle ear as an implantable sensor for hearing devices,* Scientific reports **8**, 3920 (2018).

[13] J. C. Long, H. W. Chan, A. B. Churnside, E. A. Gulbis, M. C. Varney, and J. C. Price, *Upper limits to submillimetre-range forces from extra space-time dimensions,* Nature **421**, 922 (2003).

[14] R. G. Knobel and A. N. Cleland, *Nanometre-scale displacement sensing using a single electron transistor,* Nature **424**, 291 (2003).

[15] K. Gabriel, F. Behi, R. Mahadevan, and M. Mehregany, *In situ friction and wear measurements in integrated polysilicon mechanisms,* Sensors and Actuators A: Physical **21**, 184 (1990).

[16] K. Deng, R. J. Collins, M. Mehregany, and C. N. Sukenik, *Performance impact of monolayer coating of polysilicon micromotors,* Journal of the Electrochemical Society **142**, 1278 (1995).

[17] L. L. Howell, *Compliant mechanisms* (John Wiley & Sons, 2001).

[18] D. F. Machekposhti, N. Tolou, and J. L. Herder, *A fully compliant homokinetic coupling,* Journal of Mechanical Design **140**, 012301 (2018).

[19] S. Kota, J. Hetrick, Z. Li, and L. Saggere, *Tailoring unconventional actuators using compliant transmissions: design methods and applications,* IEEE/ASME Transactions on mechatronics **4**, 396 (1999).

[20] D. F. Machekposhti, N. Tolou, and J. Herder, *A statically balanced fully compliant power transmission mechanism between parallel rotational axes,* Mechanism and Machine Theory **119**, 51 (2018).

[21] C. B. Pedersen and A. A. Seshia, *On the optimization of compliant force amplifier mechanisms for surface micromachined resonant accelerometers,* Journal of Micromechanics and Microengineering **14**, 1281 (2004).

[22] S.-C. Huang and G.-J. Lan, *Design and fabrication of a micro-compliant amplifier with a topology optimal compliant mechanism integrated with a piezoelectric microactuator,* Journal of Micromechanics and Microengineering **16**, 531 (2006).

[23] A. J. Nielson and L. L. Howell, *An investigation of compliant micro-half-pantographs using the pseudorigid body model,* Mechanics of structures and machines **29**, 317 (2001).

[24] J. Hetrick and S. Kota, *An energy formulation for parametric size and shape optimization of compliant mechanisms,* Journal of Mechanical Design **121**, 229 (1999).

[25] S. Kota, J. Hetrick, Z. Li, S. Rodgers, and T. Krygowski, *Synthesizing high-performance compliant stroke amplification systems for mems,* in *Micro Electro Mechanical Systems, 2000. MEMS 2000. The Thirteenth Annual International Conference on* (IEEE, 2000) pp. 164–169.

[26] P. Xu, Y. Jingjun, Z. Guanghua, B. Shusheng, and Y. Zhiwei, *Analysis of rotational precision for an isosceles-trapezoidal flexural pivot,* Journal of mechanical design **130**, 052302 (2008).

[27] K. R. Williams and R. S. Muller, *Etch rates for micromachining processing,* Journal of Microelectromechanical systems **5**, 256 (1996).

[28] K. R. Williams, K. Gupta, and M. Wasilik, *Etch rates for micromachining processing-part ii,* Journal of microelectromechanical systems **12**, 761 (2003).

[29] M. A. Hopcroft, W. D. Nix, and T. W. Kenny, *What is the young's modulus of silicon?* Journal of microelectromechanical systems **19**, 229 (2010).

4

A SYNTHESIS METHOD TO DESIGN COMPLIANT FREQUENCY MULTIPLIER TRANSMISSIONS

The two previous chapters presented different frequency doubler transmission mechanisms. As it was briefly discussed in Chapter 2, higher multiplication ratios based on a power of two can be achieved by a serial combination of the frequency doubler transmission building blocks. However, the design of compliant frequency multiplier transmissions with multiplication ratio based on odd or other prime numbers is not trivial. This chapter presents a synthesis method, based on serial singularity in mechanism, to design frequency multiplier transmissions with any integer multiplication ratios. Section 4.1 briefly discusses the singularity analysis and introduces a graphical method based on the instant centers of rotation to identify serial singularity in one degree of freedom (DoF) rigid-body mechanisms. To generate more topologies for frequency multiplier transmission mechanisms, six-bar planar linkages are classified based on serial singularity and presented in Section 4.2. The results led to develop a synthesis method in Section 4.3 to design transmission mechanisms with any integer frequency ratios by combining the frequency doubler building blocks. Furthermore, to evaluate the proposed synthesis method experimentally, two compliant transmission mechanisms with the frequency ratios of "3" and "4" are designed and dimensioned in Section 4.4 on macro-scale.

4.1. SERIAL SINGULARITY ANALYSIS IN PLANAR MECHANISMS

4.1.1. ANALYTICAL METHOD

A primary analytical description of singularity in closed-loop kinematic chains was introduced by Gosselin and Angeles [1]. They classified three different types of singularity in the close-loop kinematic chains, where the *serial* singularity is the first type in this classification. Moreover, a number of techniques have been developed to investigate and identify the singularity conditions in mechanisms and parallel manipulators [2–6].

The relationship between input and output coordinates of an arbitrary closed-loop kinematic chain can be written as [1]

$$F(\theta_{in}, \theta_{out}) = 0 \tag{4.1}$$

where θ_{in} and θ_{out} represents the input and output coordinates, respectively. By differentiating Eq. 4.1 with respect to time, the input-output velocity relationship can be written as

$$A\dot{\theta}_{in} + B\dot{\theta}_{out} = 0 \tag{4.2}$$

where

$$A = \frac{\partial F}{\partial \theta_{in}}, \quad B = \frac{\partial F}{\partial \theta_{out}}. \tag{4.3}$$

and where A and B are both Jacobian matrices, which are scalers for a single-DoF transmission mechanism. The first kind of singularity (called *serial* singularity) occurs in the configuration where matrix A is singular, resulting in zero output velocity for a non-zero velocity at the input.

Therefore, different poses of serial singularity in the mechanism can be identified by considering the input-output velocity relationship and investigating the conditions where the coefficient of the input velocity is zero.

4.1.2. GRAPHICAL METHOD

For a single-DoF mechanism, the input-output velocity relationship can be directly identified by instant center approach [6, 7]. This aids to graphically identifying the number of poses, and the conditions for *serial* singularity in mechanisms.

Considering a single-DoF transmission mechanism and its instant centers of rotation, the instantaneous input-output velocity relationship can be given by

$$(I_{2C} - I_{12})\,\dot{\theta}_{in} + (I_{2C} - I_{1C})\,\dot{\theta}_{out} = 0. \tag{4.4}$$

where (I) indicating the instantaneous center of rotation between different bodies: ground link (1), the input link (2), and the output link (C). The *serial* singularity occurs for the configurations in which the coefficient of input velocity is equal to zero, i.e. $(I_{2C} - I_{12}) = 0$. This corresponds to the configurations in which the instant center of rotation I_{2C} coincides with I_{12}.

For a four-bar linkage shown in Figure 4.1, the instantaneous input-output velocity relationship can be written as

$$(I_{24} - I_{12})\,\dot{\theta}_2 + (I_{24} - I_{14})\,\dot{\theta}_4 = 0 \tag{4.5}$$

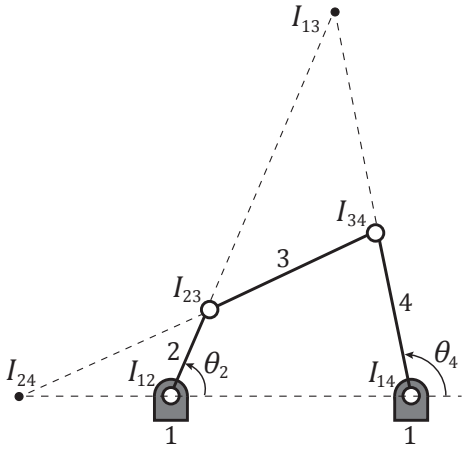

Figure 4.1: A planar four-bar linkage and its instantaneous centers of rotation between different links. Link 2 and link 4 are considered as the input and the output members, respectively.

The *serial* singularity occurs in the configuration where the instant center of rotation I_{24} coincides with I_{12}, or in other words when link 2 and link 3 are aligned. A four-bar linkage can potentially be considered as a frequency doubler building block, since there is only one serial singularity configuration if a limited range of motion is concerned.

4.1.3. CLASSIFICATION OF SIX-BAR LINKAGES BASED ON SERIAL SINGULARITY

Methods to identify singularity in one degree of freedom (one-DoF) mechanisms can be used to classify planar linkages based on the number of poses and the conditions for *serial* singularity. This provides a deeper insight into other topologies for frequency multiplication within planar linkages.

Here, six-bar linkages are classified based on their serial singularity properties. For a six-bar linkage that is constructed from six links and seven joints, and with link 2 and link 6 as the input and the output members, respectively, Eq. 4.4 can be rewritten as

$$(I_{26} - I_{12})\dot{\theta}_2 + (I_{26} - I_{16})\dot{\theta}_6 = 0. \tag{4.6}$$

The serial singularity occurs in the configurations where the instant center of rotation I_{26} coincides with I_{12}. Since the serial singularity is dependent on the kinematic arrangement of a linkage, various situations may produce it. There are five different types of kinematic arrangements for six-bar linkages, known as Watt-I, Watt-II, Stephenson-I, Stephenson-II, and Stephenson-III. Considering the proposed graphical method, the six-bar kinematic chains can be discussed and classified into three main categories based on the number of serial singularities and their corresponding geometrical conditions.

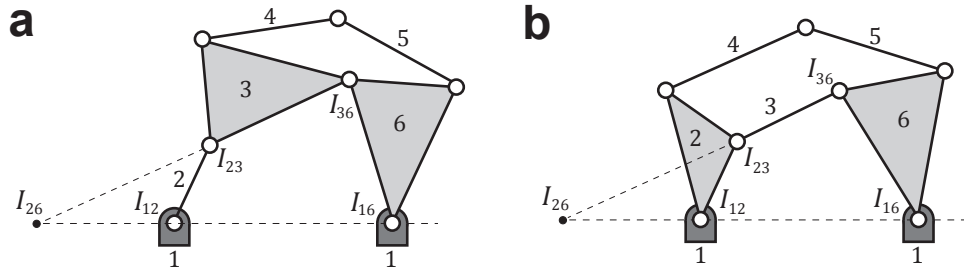

Figure 4.2: First category of six-bar linkages and the conditions for serial singularity: (a) Watt-I and (b) Stephenson-I.

First category: Watt-I and Stephenson-I six-bar linkages are in this category, as shown in Figure 4.2. For a finite travel range, there is only one serial singularity configuration in Watt-I and Stephenson-I. For both linkages, this occurs when the instant center of rotation I_{26} coincides with I_{12}, which corresponds to configurations in which link 2 is aligned with link 3.

Second category: The Stephenson-II and Stephenson-III six-bar linkages are in this category, where there is only one configuration for serial singularity. As can be seen in Figure 4.3, the instant center of rotation I_{26} coincides with I_{12} when the instant center of rotation I_{36} aligns with link 2. In other words, the serial singularity in Stephenson-II and Stephenson-III linkages corresponds to configurations where all three lines along links 2, 4, and 5 intersect each other at a single point. Since there is only one serial singularity configuration, Stephenson-II and III can also be represented as frequency doubler building blocks. One of the advantages of these two six-bar linkages over the four-bar mechanism is that there are more parameters for kinematic optimization and a higher *G.A.*

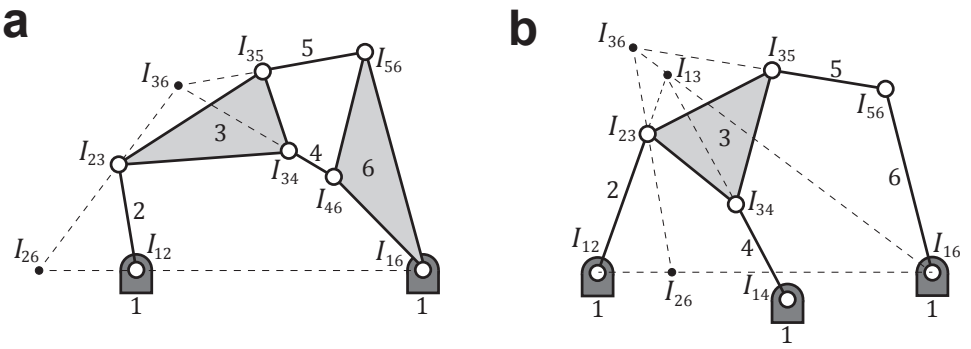

Figure 4.3: Second category of six-bar linkages and the conditions for serial singularity: (a) Stephenson-II and (b) Stephenson-III.

Third category: Watt-II is the only example from six-bar linkages which gives two serial singularity poses. As can be seen in Figure 4.4, there are two different conditions to have the instant center of rotation I_{26} coincide with I_{21}. The first serial singularity condition corresponds to the configuration in which the instant center of rotation I_{24} coincides with I_{12} (i.e. links 2 and 3 are aligned), and the second serial singularity condition corresponds to the configuration in which the instant center of rotation I_{46} coincides with I_{14} (i.e. links 4*c* and 5 are aligned). These two conditions correspond to serial singularity in each four-bar loop in the Watt-II six-bar linkage.

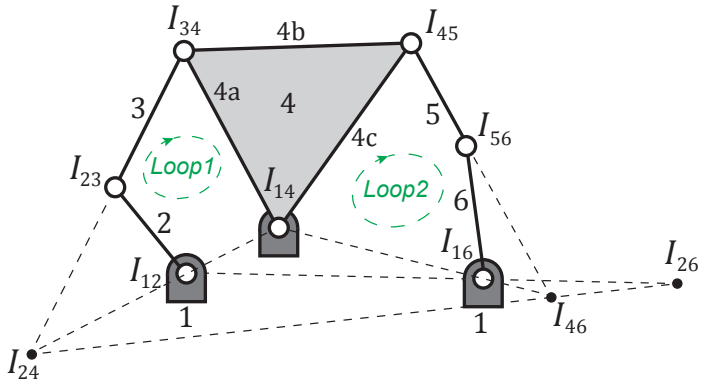

Figure 4.4: The instant centers of rotation for Watt-II six-bar linkage and the conditions for the serial singularity poses.

In fact, The Watt-II six-bar linkage is a frequency multiplier transmission mechanism topology with two four-bar loops that each are equivalent with a frequency doubler building block. Depending on the initial arrangement of two four-bar loops that are concatenated, two different scenarios may occur for the maximum number of serial singularity poses in the Watt-II linkage and their corresponding frequency multiplication ratios. The first scenario corresponds to an arrangement in which the serial singularity in *Loop* 1 occurs before the serial singularity in *Loop* 2 for a defined travel range. In this case, Watt-II experiences a maximum of two serial singularity configurations, which results in a transmission mechanism topology with a frequency multiplication ratio of "3". The second scenario corresponds to an initial linkage arrangement in which the serial singularity in *Loop* 2 occurs before the serial singularity in *Loop* 1. In this case, *Loop* 2 can passes its serial singularity configuration maximum two times, while *Loop* 1 experiences its serial singularity configuration. This results in three serial singularity configurations in Watt-II, which makes it a transmission mechanism topology with a frequency multiplication ratio of "4".

4.2. SYNTHESIS OF FREQUENCY MULTIPLIER TRANSMISSIONS

As discussed in Chapter 2, the frequency multiplication ratio of a compliant frequency multiplier transmission mechanism can be identified based on the number of serial singularities, m, in the kinematic chain within the considered range of motion, and can be given by

$$\frac{f_{out}}{f_{in}} = m + 1 \tag{4.7}$$

where f_{out} and f_{in} are the motion frequencies of the input and the output members of the mechanism, respectively.

As it was shown in the Watt-II six-bar linkage, topologies for frequency multiplier transmissions with different number of serial singularity, m, can be generated by concatenating a number of frequency doubler building blocks. Here, a synthesis method is developed based on the arrangement of the serial singularity in planar linkages to design frequency multiplier transmission mechanisms with any integer multiplication ratios.

In general, there are two different initial configurations for a frequency doubler building block which can be concatenated to design frequency multiplier transmissions with any integer multiplication ratios. These are at serial singularity configuration, and at non-singular configuration. The frequency ratios can be achieved based on the number of frequency doubler building blocks in the kinematic chain, and their initial arrangement with respect to each other.

The double-slider four-bar mechanism is a basic example of a frequency doubler building block, discussed in Chapter 2. Two different initial configurations of this building block, one at the serial singularity configuration and one at an initially angled configuration, are shown in Figure 4.5 (a). The building block shown at an initially angled position (Block-Cos) doubles the frequency of a cosine-wave input reciprocating motion, and the one at initially configured at serial singularity configuration (Block-Sin) doubles the motion frequency of a sine-wave input reciprocating movement. By concatenating these two frequency doubler building blocks, kinematics to design frequency multiplier transmission mechanism with different frequency ratios can be generated.

The frequency multiplier transmission mechanism with the frequency ratios of "3" and "4" are shown in Figure 4.5 (b). As it was discussed for Watt-II six-bar linkage, to design a kinematic for frequency ratio of "3" the serial singularity at the second building block must occur after the serial singularity in the first building block. To achieve this, a Block-Cos of double slider mechanism is concatenated with a Block-Sin of double slider mechanism. As can be seen in Figure 4.5 (b), for the frequency multiplier transmission mechanism with a frequency ratio of "4", two double-slider linkage both at the angled arrangement (Block-Cos) are concatenated. In this combination, the serial singularity in the second building block occurs earlier than the serial singularity in the first frequency doubler building block, similar to the second scenario of Watt-II linkage, which results in a frequency ratio of "4". The sequence of the input motion u_{in} and the corresponding output displacement u_{out}, indicated with blue arrows, are shown in Figure 4.5(b). Similar to the frequency ratio of "4", a frequency multiplier transmission mechanism with the ratio of 2^n can be generated by concatenating n number of initially angled frequency doubler building blocks, where $n = 1, 2, ..., N$.

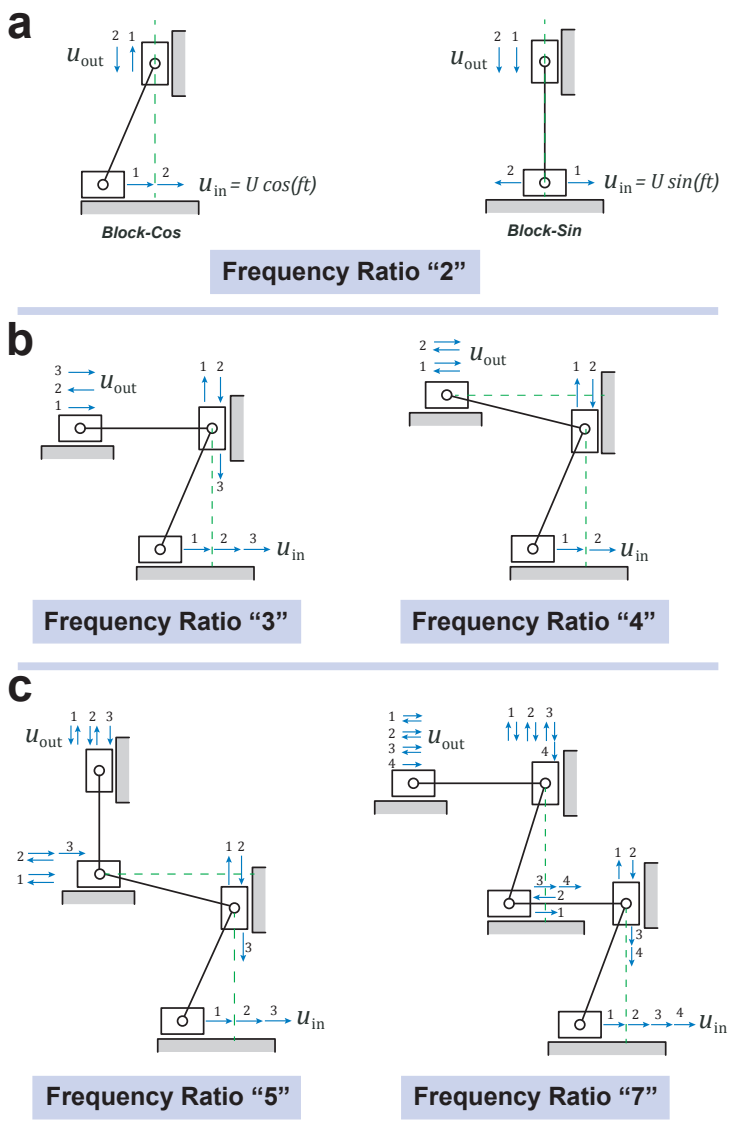

Figure 4.5: Arrangement of a frequency doubler transmission building block to design frequency multiplier transmission mechanism with different frequency ratios. (a) Double-slider four-bar mechanism as a frequency doubler building block demonstrated at two different initial configurations. (b) Arrangement of the frequency doubler building blocks for frequency ratio of 3 and 4. (c) Arrangement of the frequency doubler building blocks for frequency ratios of 5 and 7. The sequence of the input and the output motions are indicated with blue arrows and corresponding numbers. The green dashed lines illustrate the serial singularity configuration of the double-slider mechanism.

Combinations for the frequency multiplier transmission mechanisms with the frequency ratio of "5" and "7" are represented in Figure 4.5 (c). As can be seen, the fre-

quency ratio of "5" can be generated by adding a Block-Sin of double slider mechanism to the last stage of the frequency multiplier transmission with the frequency ratio of "4". In the same manner, the frequency ratio of "7" can be represented by a transmission mechanism with frequency ratio of "6" added with a Block-Sin of the double slider mechanism. As can be seen in the topology of the transmission mechanisms with the frequency ratio of "3", "5", and "7", a frequency ratio with a prime or an odd number can be generated by adding a Block-Sin frequency doubler to a multiplier transmission mechanism with a frequency ratio of previous even number of that prime or odd number.

Therefore, the Block-Cos and Block-Sin of the frequency doubler building blocks developed in the previous chapters can be concatenated in the proposed order to design frequency multiplier transmission mechanisms with any integer multiplication ratios.

4.3. COMPLIANT DESIGNS AND FABRICATION

To demonstrate the validity of the proposed synthesis method, two compliant frequency multiplier transmission mechanisms with the frequency ratios of "3" and "4" are developed in this section. To multiply both *G.A.* and *F.A.*, the compliant frequency doubler transmission based on the eight-bar linkage, developed in Chapter 2, is used as a frequency doubler principle. The equivalent compliant building blocks are shown in Figure. 4.6 for two different initial configurations, named as Block-Cos and Block-Sin.

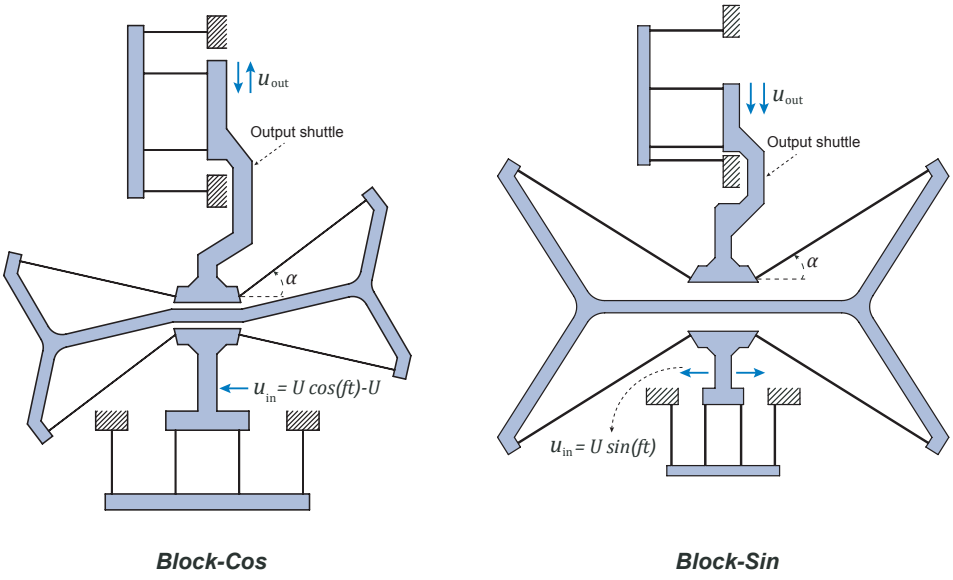

Figure 4.6: The compliant frequency doubler building blocks based on the eight-bar linkage are demonstrated at two different initial configurations. Block-Cos doubles the frequency of a cosine-wave input reciprocating motion, and Block-Sin doubles the motion frequency of a sine-wave input reciprocating movement.

4.3.1. A COMPLIANT FREQUENCY MULTIPLIER WITH A RATIO OF "3"

A compliant frequency multiplier transmission mechanism with a frequency ratio of "3" is designed and developed based on the proposed synthesis method, shown in Figure 4.7. As can be seen in Figure 4.7, the first building block is initially at the angled position (Block-Cos) and the second building block is at the singularity configuration (Block-Sin), similar to the topology shown in Figure 4.5(b) for the frequency ratio of "3".

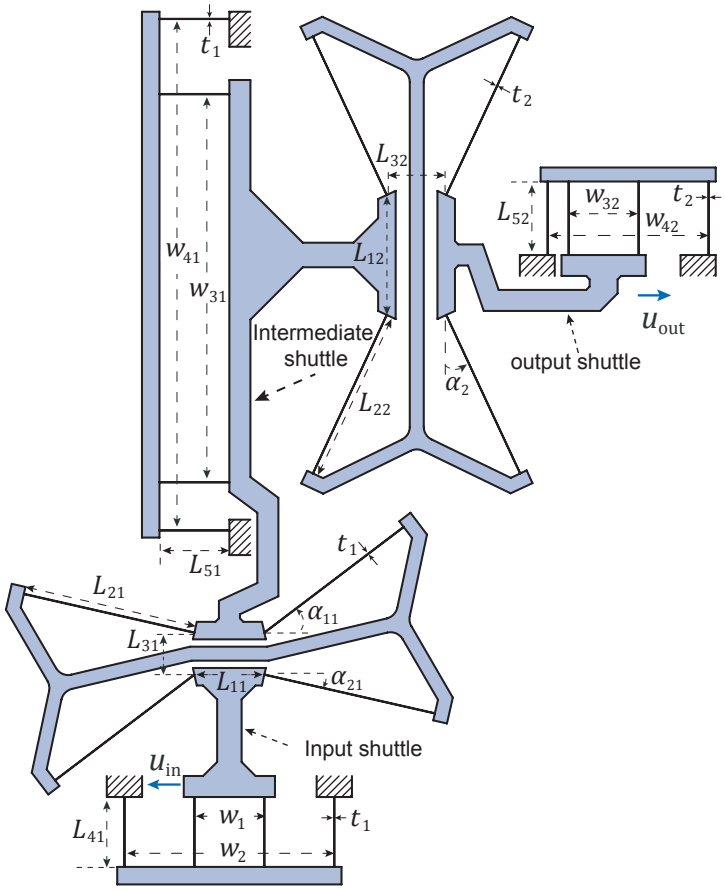

Figure 4.7: The design of compliant frequency multiplier transmission mechanism with ratio of "3".

A macro scale compliant frequency multiplier transmission mechanism with a frequency ratio of "3" is dimensioned. The prototype design parameters are summarized in Table 4.1. As can be seen in Figure 4.8 (a), a macro scale prototype is fabricated, where the austenitic stainless steel with the width of $b = 8mm$ is used for all flexures in the design. The deflections of the compliant prototype at different input displacement are shown in Figure 4.8 (b)-(d).

Table 4.1: Design parameters for the compliant macro frequency multiplier transmission mechanism with ratio of "3". All the length are given in [mm].

Parameters B1	L_{11}	L_{21}	L_{31}	L_{41}	L_{51}	w_1	w_2	w_{31}	w_{41}	t_1	α_{11}	α_{21}
Values B1	20	50	12	20	20	20	60	111	146	0.1	37.2°	12.8°
Parameters B2	L_{12}	L_{22}	L_{32}	L_{52}	w_{32}	w_{42}	t_2	α_2				
Values B2	34	50	17	21	30	66	0.05	25°				

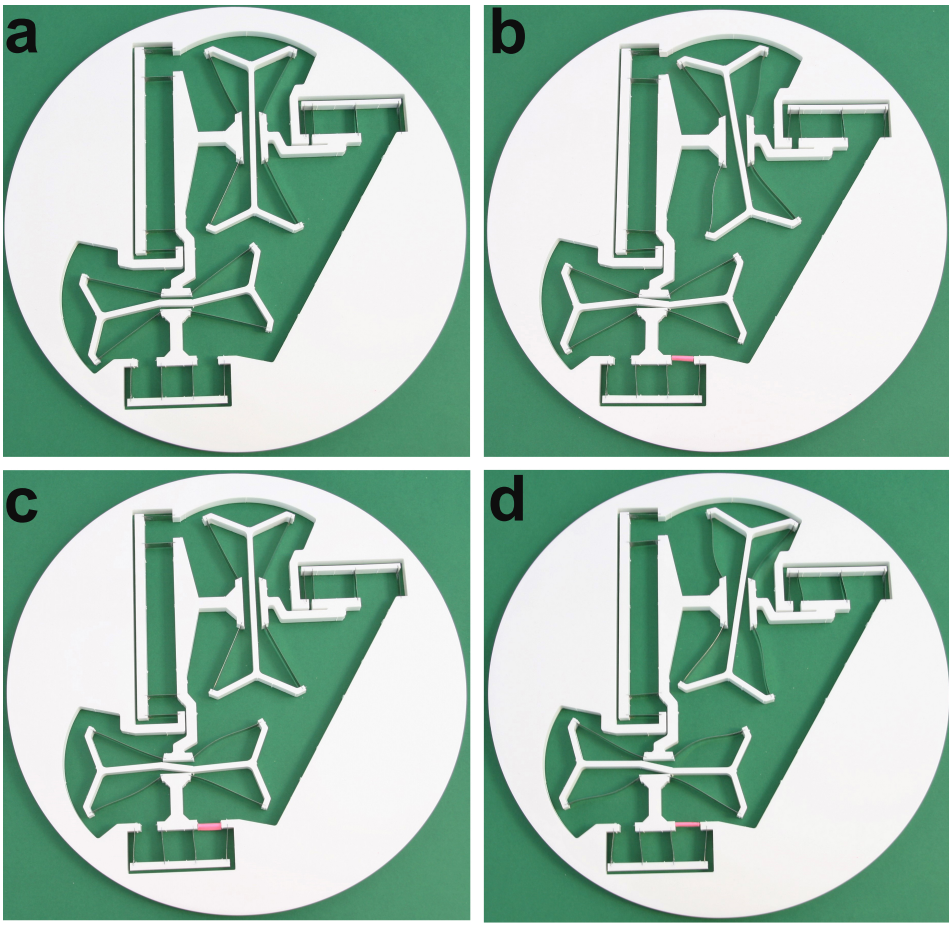

Figure 4.8: The prototype of compliant frequency multiplier transmission mechanism with a frequency ratio of "3". (a) The top view of the prototype at the rest position. The prototype at the deflected positions: (b) For an input displacement of u_{in} = 0.4 mm towards left, the output displaced about 1 mm towards right. (c) For an input displacement of u_{in} = 0.75 mm towards left, the output shuttle moves to its initial position. (d) The output shuttles moves again towards right while the input is displaced about u_{in} = 1.2 mm towards left.

4.3.2. A COMPLIANT FREQUENCY MULTIPLIER WITH A RATIO OF "4"

A compliant frequency multiplier transmission mechanism with a frequency ratio of "4" is developed based on the proposed synthesis method, shown in Figure 4.9. As can be seen, the first building block is at the serial singularity configuration (Block-Sin) and the second building block is at an initially angle configuration (Block-Cos).

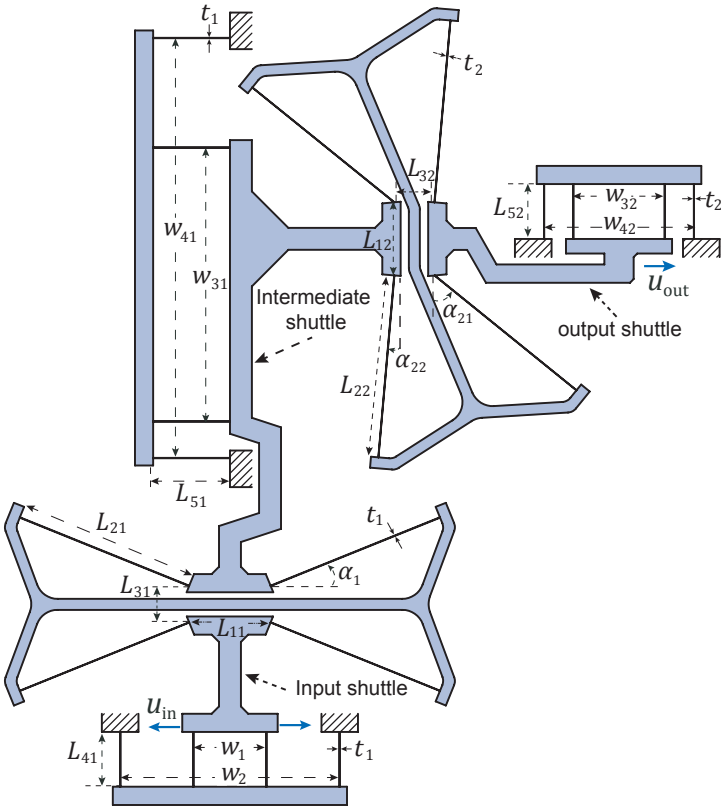

Figure 4.9: The design of compliant frequency multiplier transmission mechanism with ratio of 4.

Similarly, a macro scale compliant frequency multiplier transmission mechanism with a frequency ratio of "4" is dimensioned, design parameters are summarized in Table 4.2. As can be seen in Figure 4.10, a macro scale prototype is fabricated and the deflections of the compliant prototype at different input displacement are shown in Figure 4.8 (a)-(d).

Table 4.2: Design parameters for the compliant macro frequency multiplier transmission mechanism with ratio of "4". All the length are given in $[mm]$.

Parameters B1	L_{11}	L_{21}	L_{31}	L_{41}	L_{51}	w_1	w_2	w_{31}	w_{41}	t_1	α_1
Values B1	22.2	50	10	15	21	20	60	75	115	0.1	22°
Parameters B2	L_{12}	L_{22}	L_{32}	L_{52}	w_{32}	w_{42}	t_2	α_{21}	α_{22}		
Values B2	20	50	11	15	25	41	0.05	51°	5°		

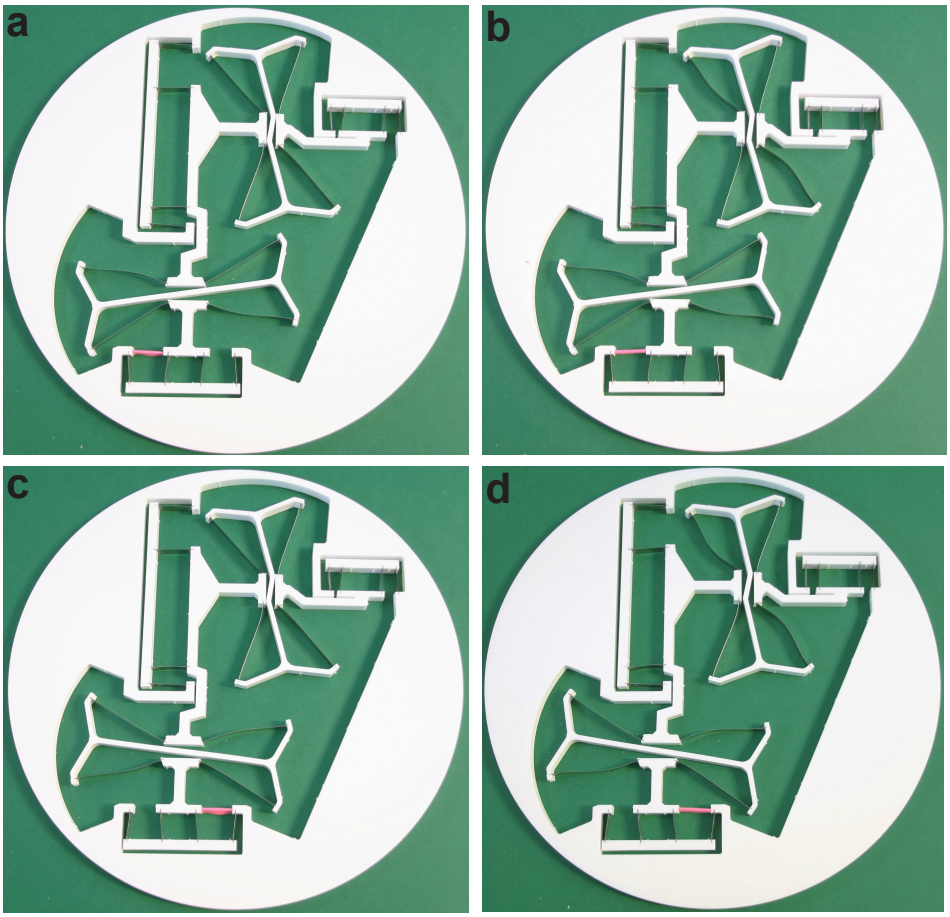

Figure 4.10: The prototype of compliant frequency multiplier transmission mechanism with a frequency ratio of "4" at deflected positions. For an input displacement towards right, the output displaced (a) first towards left, and then (b) moves back to its initial position. Similarly, for an input displacement towards left, the output displaced (c) first towards left, and then (d) moves back to its initial position.

4.4. EXPERIMENTAL RESULTS AND DISCUSSION

A customized test setup, described in Chapter 2, was used to measure the actuation stiffness and the input-output kinematics of the prototypes of proposed compliant frequency multiplier transmission mechanisms. Moreover, a parametric finite element model (FEM) was created in ANSYS to analyze the proposed designs. The beam element based on the Timoshenko beam theory *(BEAM188)* was used for the flexures, and rigid constraint elements *(MPC184)* for the rigid-bodies. The FEM model was evaluated while the maximum Von Mises stress was limited by $210MPa$. The other material specifications are $E = 183\ GPa$, and $\rho = 7.9\ gr/cm^3$ which were considered during modeling. Furthermore, the Pseudo-Rigid-Body Model (PRBM) developed in Chapter 2 for the

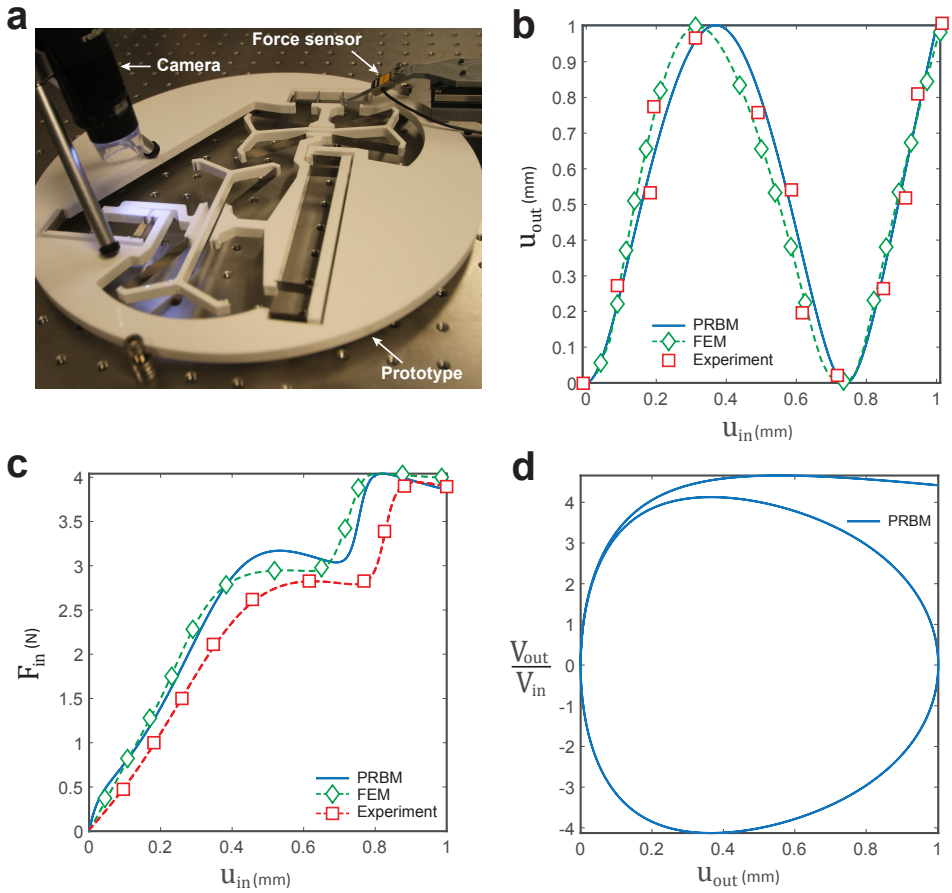

Figure 4.11: Characterization and performance of the compliant frequency multiplier transmission mechanism with a frequency ratio of "3". (a) The experimental set-up to evaluate the actuation force and the input-output kinematics of the macro device. (b) The results for input-output displacement relationships, (c) Force-Displacement characteristics of the device. (d) The input-output velocity ratio versus the output displacement. The results are from Pseudo-Rigid-Body Model (PRBM), finite element model (FEM), and the experiment.

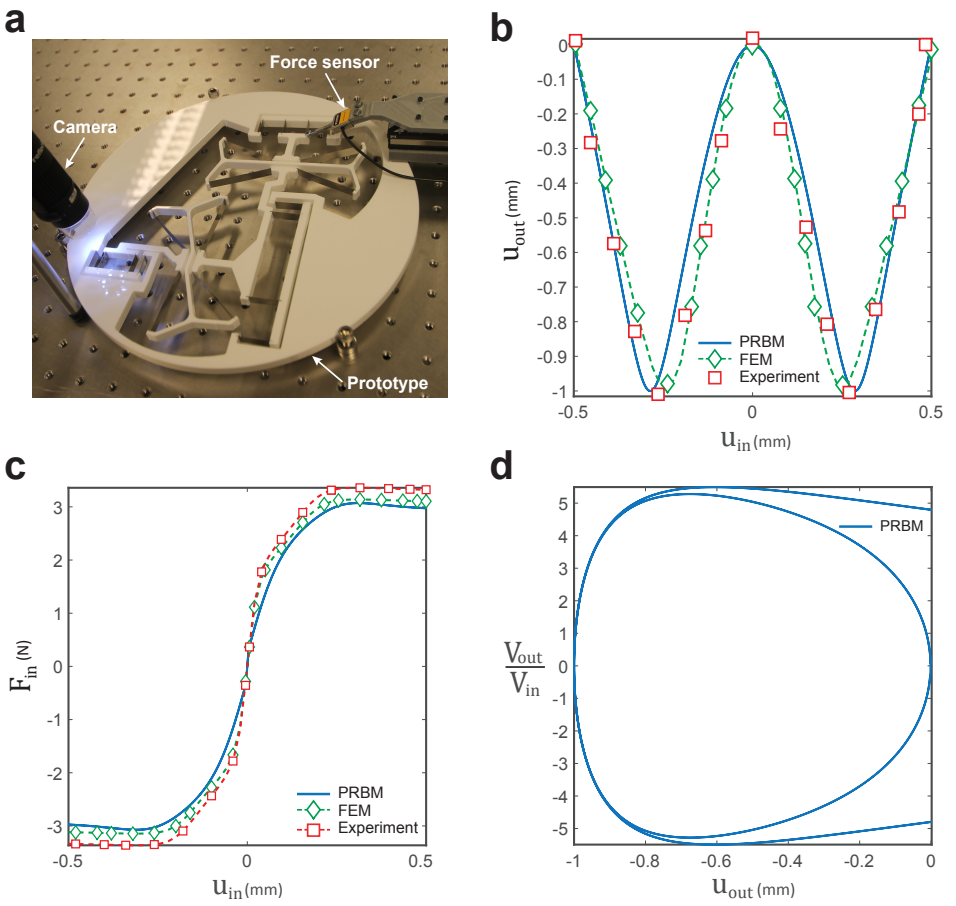

Figure 4.12: Characterization and performance of the compliant frequency and speed multiplier transmission mechanism with ratio of 4. (a) The experimental set-up to evaluate the actuation force and the input-output kinematics of the macro device. (b) The results for input-output displacement relationships, (c) Force-Displacement characteristics of the device. (d) The input-output velocity ratio versus the output displacement. The results are from Pseudo-Rigid-Body Model (PRBM), finite element model (FEM), and the experiment.

eight-bar compliant frequency doubler transmission is used to study the kinematics and stiffness characteristics of the proposed compliant designs.

The results for the compliant frequency multiplier transmission with a frequency ratio of "3" are shown in Figure 4.11. The optical displacement measurement, FEM, and the Pseudo-Rigid-Body Model (PRBM) show the same behavior and order of magnitude for the input-output kinematic relationship, shown in Figure 4.11 (b). As can be seen, the proposed compliant transmission mechanism triples the input motion frequency, with an output displacement of 1 mm. The PRBM shows a maximum discrepancy of 18.6% and 20% with the FEM and experiment, respectively. The differences can be explained by the accuracy of the displacement measurement, with percentage uncertainty of 10%, and the accuracy of the PRBM and the values chosen for the characteristic radius factor

and the stiffness coefficient.

The force-displacement measurement is illustrated and compared to the FEM, and the PRBM in Figure 4.11 (c). The results show a nonlinear correlation between the actuation force and the input displacement, which can be explained by the nonlinear kinematics of frequency doubler building block in the design. As can be seen, the results from the FEM and the experiment are in agreement. Although, there is a maximum discrepancy of 25% between these results, which can be explained by the uncertainty in the force measurement, with percentage uncertainty of 2.5%, and the stiffness of the Acrylic rigid parts which were considered rigid in the FEM model. As can be seen, the PRBM force-deflection result differs from the FEM, which is primarily due to the initial angle α_1 and α_2 of the fixed-fixed flexures, which decreases the accuracy of the PRBM.

The velocity ratio, estimated by PRBM, between the input and output shuttles versus the output displacement is shown in Figure 4.11 (d). As can be seen, the kinematics of the output motion for the first cycle is symmetric but differs from the kinematics of the last half of a cycle. Besides, the third half of the output kinematic shows a higher output velocity ratio while the variation of this ratio is less than the first cycle.

The results for the compliant frequency frequency multiplier transmission with a frequency ratio of "4" are shown in Figure 4.12. The optical displacement measurement, FEM, and the Pseudo-Rigid-Body Model (PRBM) show the same behavior and order of magnitude for the input-output kinematic relationship, shown in Figure 4.12 (b). As can be seen, the proposed compliant transmission mechanism quadruples the frequency of a reciprocating input motion. The PRBM shows a maximum discrepancy of 14% and 18.3% with the FEM and experiment, respectively. The differences can be explained by the accuracy of the displacement measurement, with percentage uncertainty of 10%, and the accuracy of the PRBM and the values chosen for the characteristic radius factor and the stiffness coefficient.

The force-deflection measurement is represented and evaluated with the FEM, and the PRBM in Figure 4.12 (c). The results show a nonlinear correlation between the actuation force and the input displacement, which can be explained by the nonlinear kinematics of frequency doubler building block in the design. As can be seen, the results from the FEM and the experiment are in agreement. Although, there is a maximum discrepancy of 3.5% between these results, which can be explained by the uncertainty in the force measurement, with percentage uncertainty about 2.9%. Similar to the compliant transmission with a frequency ratio of "3", the difference between the PRBM and FEM in this device is also caused by the accuracy of the PRBM. However, this deviation in the compliant transmission design with a frequency ratio of "4" is less. This is due to the fact that the first frequency doubler building block in this design experiences smaller deflections, which results in a more accurate PRBM.

In the design of the proposed frequency multipliers, a thinner beam was used for the second frequency doubler building block in the design. This was considered since the mechanical advantage $M.A.$ of the compliant building block drops due to their internal stiffness. Therefore, a further study could assess the static balancing of the compliant frequency doubler building blocks to cancel out their inherent internal stiffness.

4.5. CONCLUSIONS

In this chapter, a synthesis method was developed to design compliant frequency multiplier transmission mechanisms. The investigation of serial singularity in planar mechanisms using the instant center approach has provided a deeper insight into the relation between the arrangement of serial singularity in planar linkages and the frequency multiplication ratio. The results have shown that any integer frequency ratios, e.g. even, odd, and prime numbers, can be achieved by arrangement of frequency doubler building blocks. Two compliant frequency multiplier transmission mechanisms with the frequency ratios of "3" and "4" were developed to demonstrate the validity of the proposed synthesis method. The prototypes were made and experiments were performed to evaluate the input-output kinematic and the actuation stiffness of the compliant designs.

REFERENCES

[1] C. Gosselin and J. Angeles, *Singularity analysis of closed-loop kinematic chains,* IEEE transactions on robotics and automation **6**, 281 (1990).

[2] D. Zlatanov, R. Fenton, and B. Benhabib, *A unifying framework for classification and interpretation of mechanism singularities,* Journal of Mechanical Design **117**, 566 (1995).

[3] D. Zlatanov, R. Fenton, and B. Benhabib, *Identification and classification of the singular configurations of mechanisms,* Mechanism and Machine Theory **33**, 743 (1998).

[4] R. Di Gregorio, *A novel geometric and analytic technique for the singularity analysis of one-dof planar mechanisms,* Mechanism and Machine Theory **42**, 1462 (2007).

[5] J.-P. Merlet, *Parallel robots*, Vol. 128 (Springer Science & Business Media, 2006).

[6] H. M. Daniali, P. Zsombor-Murray, and J. Angeles, *Singularity analysis of planar parallel manipulators,* Mechanism and Machine Theory **30**, 665 (1995).

[7] A. G. Erdman, G. N. Sandor, and S. Kota, *Mechanism design: Analysis and synthesis. Vol. 1* (Prentice-Hall, 1997).

5

COMPLIANT TRANSMISSION COUPLINGS

The previous chapters developed synthesis methods and new kinematics for the design of compliant frequency multiplier transmission mechanisms. The proposed embodiments are devices with a finite travel range of motion as the alternatives to the continuous rotating classical gears, which convert the speed and force from a source of power to an output. However, several applications in the field of precision engineering require compliant transmission devices which convert the motion direction from a continuous rotating input to an output. This chapter aims to design and develop compliant transmission couplings which can deal with different misalignments between the direction of motion of the input and output axes. The chapter consists of two sections. Section 5.1 introduces a compliant spatial transmission coupling which can accommodate with angular misalignments. Section 5.2, presents a compliant planar coupling generated based on rigid-body Oldham linkage which can deal with lateral misalignments.

Parts of this chapter have been published in *Journal of Mechanical Design* [1, 2], and *Mechanisms and Machine Theory* [3].

5.1. COMPLIANT COUPLING FOR ANGULAR MISALIGNMENT

5.1.1. INTRODUCTION

Universal joints or power transmission couplings are spatial mechanisms which are used in general machinery to transfer rotary motion or energy between two angled shafts. For centuries, Hooke's universal joint, well-known as Cardan joint, has been used as a primary solution for power transmission [4]. However, this coupling has a non-uniform, i.e. non-constant velocity, transfer function. As the misalignment angle between the two axes increases, the non-uniformity of the speed transmission increases correspondingly. This caused increased stress on the members of the coupling and potentially harmful vibrations on the driven shaft [5]. To overcome the problem of non-uniform transmission, different types of rigid-body constant velocity universal joints (CV joints), also known as homokinetic couplings, have been invented [6–11]. A brief but broad overview of the rigid-body CV joints, a classification, and their performance can be found in [1, 12]. The rigid-body configuration has many disadvantages, such as wear, friction, and backlash. Besides, in harsh environments such as deep sea, agriculture, aerospace, or in the clean room and vacuum conditions, the fact that known CV-Joints need lubrication and maintenance presents a serious problem [13]. Moreover, the backlash in rigid mechanical connections also can become an obstacle in high precision engineering.

Many applications in precision engineering require a precise and small mechanism to overcome the misaligning issues between two rotating shafts, such as micro measurement systems, medical devices, and precision instruments, etc. Moreover, these applications are very often situated inside of vacuum or wet environments. Therefore, it is difficult to use bearings, due to the need for lubrication [13].

Compliant mechanisms are devices that accomplish the desired motion through elastic deformation of the flexures rather than using rigid-body kinematic pairs. Flexure configurations are frequently used in precision machinery because the deletion of rigid-body kinematic pairs also eliminates the effect of backlash, wear, friction, and the need for lubrication [13–16]. Several compliant universal joints based on the Cardan joint can be found in prior art [1]. Besides, Tanik et al, proposed a PRBM model of the Cardan joint and its compliant counterpart [17].

The purpose of this section is to present the first fully compliant homokinetic coupling with high misalignment angle and true constant velocity behavior to overcome the shortcomings of rigid-body CV joints. A design which can be fabricated as a monolithic piece is desired for micro and macro manufacturing processes such as wire EDM, and additive manufacturing.

The design of compliant homokinetic coupling is discussed in the following sections. In Section 5.1.2, the kinematic model of the design is demonstrated and studied regarding degrees of freedom and constant velocity conditions. Pseudo-Rigid-Body Model and possible compliant equivalents are proposed and analyzed in Section 5.1.3 and 5.1.4. The theoretical model is then verified with the finite element modeling and the experimental results in Section 5.1.5.

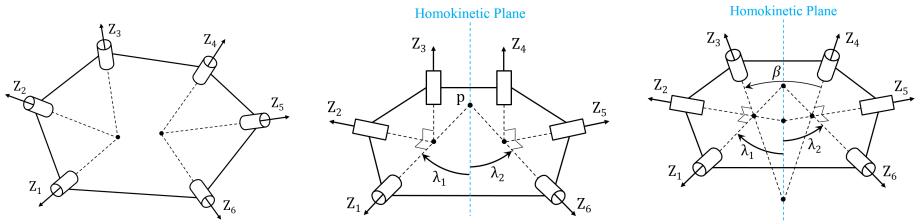

(a) (b) (c)

Figure 5.1: 6R spatial overconstrained linkages: (a) Bennett 6R hybrid linkage, (b) Double Hooke's universal joint arrangement, (c) An angled arrangement of Double Hooke's universal joint. Blue dash lines indicates the homokinetic plane.

5.1.2. KINEMATICS

KINEMATIC SELECTION

According to the literature, constant velocity transfer function and high misalignment angle are the two most important kinematic criteria in the design of power transmission couplings [1, 12]. Furthermore, it was reported that the spatial and spherical CV joints, which contain a 6R overconstrained linkage, can transfer the rotary motion uniformly with higher misalignment angle such as Double Hooke's universal joint, Thompson Coupling, and Culver joint, etc. [1]. The main advantage of this class of mechanisms, overconstrained mechanisms, is that they can be mobile using fewer links and joints that it is expected from traditional degrees of freedom formula.

The Bennett 6R hybrid spatial linkage, Figure 5.1(a), is the main combination of the rigid-body CV joints with high misalignment angles [1, 12]. This combination degenerates into the Double Hooke's universal joint, which is a 6R Overconstrained linkage [18], when each set of three rotational axes intersect each other at right angles and when the two of them, namely the two central axes Z_3 and Z_4, are parallel, Figure 5.1(b). Symmetrical configuration of a universal joint with respect to the homokinetic plane, which bisects the input axis, Z_1, and the output axis, Z_6, perpendicularly, is essential for providing a constant velocity transmission [19, 20]. According to the d'Ocagne's theory, a Double Hooke's universal joint only transmits rotation in a uniform behavior if the linkages are arranged symmetrically, and the input and output axes intersect each other at the point P in the homokinetic plane, see Figure 5.1(b). Therefore, the constant velocity transmission can only be achieved if the input and output axes are manually arranged so that it can be ensured the angle between two shafts and homokinetic plane are equal [21]. For this reason, plus the fact that the condition is not always fulfilled, i.e. $\lambda_1 \neq \lambda_2$, the Double Hooke's coupling is known as a nearly constant velocity universal joint [1].

As can be seen in Figure 5.1(c), An angled arrangement of the Double-Hooke's universal joint can guarantee a symmetric configuration respect to the homokinetic plane, i.e. $\lambda_1 = \lambda_2 = \lambda$, in the different misalignment angles. This is achieved by adding a kinematic constraint between the axes Z_3 and Z_4 in the homokinetic plane [22]. However, this is an additional kinematic constraint on the Double Hooke's universal joint which is classified in the prior art as a 6R Overconstrained linkage.

To choose the appropriate compliant kinematic pairs and ensure to provide a one

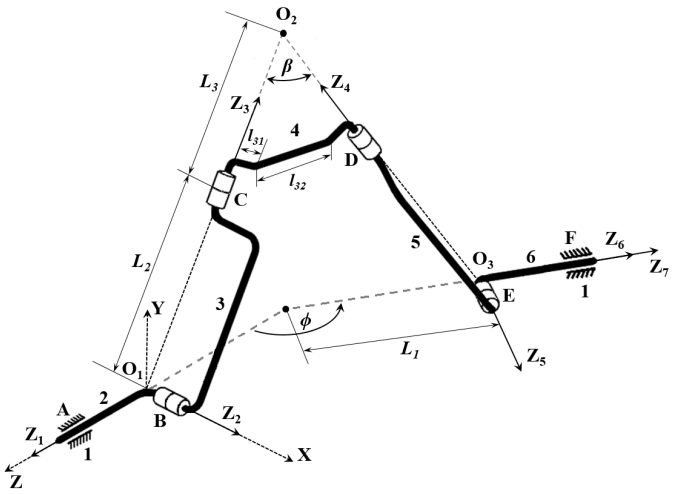

Figure 5.2: Angled arrangement of the Double Hooke's universal joint; linkage arrangement, coordinate systems, and parameters.

DoF mechanism for a full cycle rotation transmission in all different misalignment angles, the kinematics of the angled arrangement of the Double Hooke's universal joint is studied. According to the kinematic, a 3D linkage arrangement, coordinate systems, and geometric properties are shown in Figure 5.2. As can be seen, Link 2 and Link 6 are the input and the output shafts respectively, and connected to the ground, Link 1, each with a revolute joint. Each shaft is connected by a revolute joint to a link called the "Crank link", Link 3 and Link 5, respectively, where both cranks are of equal length. To illustrate the angled arrangement of Double Hooke's universal joint, the two crank links are connected with each other by a link called the "Coupler link", Link 4, with the angle β.

DEGREES OF FREEDOM ANALYSIS

The degrees of freedom (DoF) of the linkage, shown in Figure 5.2, is investigated by describing its kinematic and geometrical constraints with the screw theory. In general, there are two cases for the degrees of freedom of the universal joints. First, the mechanism should be a one DoF system for rotation transmission when the input and the output axes are grounded by two rotational bearings, as shown in Figure 5.2. Second, the output axis has to have two rotational DoF respect to the input axis. To achieve this, n number of similar sets of 4R linkage are required between the input and the output axes. This number, n, will be determined through the DoF analysis.

The Figure 5.3(a) shows the graph representation of the rotation transmission. If the output member is assigned to the end effector (EE), the mechanism can be thought of as a parallel mechanism that is made up of two kinematic chains, ABCDE and F, which connect the EE to the Ground (G). The constraints spaces applied to the Link 6 can be obtained by studying the reciprocal screws of each kinematic chain. The Plücker coordi-

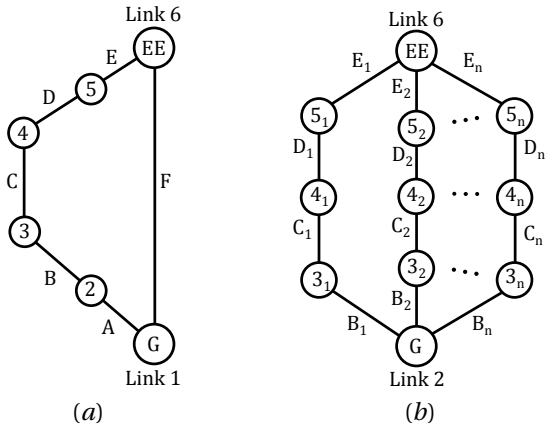

Figure 5.3: Graph representations for the Degrees of Freedom (DoF) analysis: (a) As a rotation transmission system with only one set of 6R linkage, (b) As a two rotational DoF kinematic pair with at least n number of similar sets of 4R linkage which are placed with an angular offset between the input and the output axes. The circles in the graphs indicate different links and the lines represent different revolute joints of the mechanism shown in Figure 5.2. "G" indicates the fixed link and "EE" indicates the end effector which is the output shaft.

nates of the kinematic joints A, B, C, D, and E can be denoted by

$$\$_q = \left(\vec{e}_q^T ; \left(p_q \times \vec{e}_q\right)^T\right), \quad q = \{A, B, C, D, E\}. \tag{5.1}$$

where, $\vec{e}_q$ is the vector parallel to each kinematic joint axis, and p_q is the position of an arbitrary point on the same axis. Therefore, the kinematic screw of kinematic chain ABCDE can be obtained

$$\$_{ABCDE} = \begin{bmatrix} \$_A \\ \$_B \\ \$_C \\ \$_D \\ \$_E \end{bmatrix}. \tag{5.2}$$

By calculating the null space of the kinematic screw, $\$_{ABCDE}$, the reciprocal screw of this chain can be written as

$$\$^r_{ABCDE} = \left(\frac{-\sin\phi}{L_1(\cos\phi - 1)} \quad 0 \quad 1 \quad ; \quad 0 \quad 0 \quad 0\right), \tag{5.3}$$

where, ϕ is the angle between the input and output axes, and L_1 can be determined by displacement analysis.

In the same manner, the reciprocal screw applied to the output axes, EE, by the kinematic pair F can be found. The Plücker coordinate of joint F can be given by

$$\$_F = \left(\sin\phi \quad 0 \quad \cos\phi \quad ; \quad 0 \quad -\sin\phi(\cos\phi(L_1+1)+L_1) \quad 0\right). \tag{5.4}$$

The reciprocal screws of $\$_F$ are

$$\$_F^r = \begin{bmatrix} \$_F^{r_1} \\ \$_F^{r_2} \\ \$_F^{r_3} \\ \$_F^{r_4} \\ \$_F^{r_5} \end{bmatrix}, \tag{5.5}$$

where,

$$\begin{aligned} \$_F^{r_1} &= \begin{pmatrix} 0 & 0 & 0 & ; & 0 & 1 & 0 \end{pmatrix}, \ \$_F^{r_2} = \begin{pmatrix} 0 & 0 & 0 & ; & \cot\phi & 0 & 1 \end{pmatrix}, \\ \$_F^{r_3} &= \begin{pmatrix} 1 & 0 & 0 & ; & 0 & 0 & 0 \end{pmatrix}, \ \$_F^{r_4} = \begin{pmatrix} 0 & 0 & 1 & ; & 0 & 0 & 0 \end{pmatrix}, \\ \$_F^{r_5} &= \begin{pmatrix} 0 & 1 & 0 & ; & \cos\phi(L_1+1)+L_1 & 0 & 0 \end{pmatrix}. \end{aligned} \tag{5.6}$$

Therefore, the reciprocal screws, constraints spaces, applied to the EE can be obtained

$$\$_{EE}^{C_1} = \begin{bmatrix} \$_{ABCDE}^r \\ \$_F^{r_1} \\ \$_F^{r_2} \\ \$_F^{r_3} \\ \$_F^{r_4} \\ \$_F^{r_5} \end{bmatrix}. \tag{5.7}$$

The DoF of the output axis can be calculated as

$$F = 6 - \dim \$_{EE}^{C_1} = 6 - 5 = 1, \tag{5.8}$$

where, $\dim \$_{EE}^{C_1}$ is the dimension of the constraints spaces $\$_{EE}^{C_1}$.

Therefore, the angled arrangement of Double Hooke's universal joint, with the additional kinematic constraint, is still providing one DoF for rotation transmission. However, this is valid as long as all three rotational axes in two sides of the homokinetic plane are intersecting each other at one point, i.e. Z_1, Z_2, and Z_3 at the point O_1, and Z_4, Z_5, and Z_6 at the point O_3.

The second DoF analysis is investigated to find the minimum number of similar sets, n, which are required to be arranged with an angular offset between the input and the output axes to constrain for two rotational DoF between them. As can be seen in Figure 5.3(b), the mechanism can be considered as a parallel linkage that is made up of n kinematic chains, contains four revolute joints (4R) B, C, D, and E in each, which connect the end effector (EE) to the Ground (G). In this case, the end effector is the Link 6 and the ground is the Link 2. In the same manner, as the DoF analysis in rotation transmission, the constraints spaces applied to the output shaft can be obtained by studying the reciprocal screws of each kinematic chain.

The Plücker coordinates of the kinematic joints B, C, D and E in each set can be defined by Eqn. (5.1). However, the vector parallel to the kinematic joint's axis for each set

need to be recalculated. This can be given by

$$\vec{e}_{q_m} = \left[Y\left(\frac{\pi}{2}\right)\right]\left[Z\left((m-1)\times\frac{2\pi}{n}\right)\right]\vec{e}_q, \quad q=\{B,C,D,E\}, \quad m=1,\cdots,n. \tag{5.9}$$

where, n is the number of sets of the 4R linkages connected between the input and the output axes, $\vec{e}_{q_m}$ is the vector parallel to the kinematic joint axis, q, from set m^{th}, and $[Y(\cdot)]$ and $[Z(\cdot)]$ are the rotation matrix around Y and Z axes, respectively.

It can be shown at least three sets, $n=3$, of the 4R linkages are required to constraint for two rotational DoF between the input and the output axes. The kinematic screw of each of the three parallel kinematic chains between the input and the output axes, which contains kinematic pairs B, C, D, and E, can be given by

$$\$_{B_mC_mD_mE_m} = \begin{bmatrix} \$_{B_m} \\ \$_{C_m} \\ \$_{D_m} \\ \$_{E_m} \end{bmatrix}, \qquad m=1,2,3. \tag{5.10}$$

Therefore, the reciprocal screws applied to the EE while the input axis is grounded can be given by

$$\$_{EE}^{C_2} = \begin{bmatrix} 0 & 0 & 0 & 0 & 0 & 1 \\ 0 & g_1 & g_2 & 1 & 0 & 0 \\ 0 & 0 & 0 & 0 & 0 & 1 \\ -g_1 & g_1\cot\frac{2\pi}{3} & -2g_2\cot\frac{2\pi}{3} & \cot\frac{2\pi}{3} & 1 & 0 \\ 0 & 0 & 0 & 0 & 0 & 1 \\ -g_1 & g_1\cot\frac{4\pi}{3} & -2g_2\cot\frac{4\pi}{3} & \cot\frac{4\pi}{3} & 1 & 0 \end{bmatrix}, \tag{5.11}$$

where, g_1 and g_2 can be written as

$$g_1 = \frac{2L_1\cos\theta_2\left(\sin\left(\theta_2+2\beta\right)\right)}{\sin 2\beta}, \qquad g_2 = \frac{2L_1\sin\theta_2\left(\sin\left(\theta_2+2\beta\right)\right)}{\sin 2\beta}. \tag{5.12}$$

As a result, the degrees of freedom for the output axis can be driven as

$$F = 6 - \dim\$_{EE}^{C_2} = 6-4 = 2. \tag{5.13}$$

Therefore, $n=3$ is the minimum number of sets required to constraint for two rotational DoF of the output axis respect to the input axis. However, this number can be increased as long as the mechanism can be fabricated and assembled precisely, to prevent the issues of the overconstrained linkages.

DISPLACEMENT ANALYSIS

The relative position of links and joints is described using a variant of the Denavit and Hartenberg notation [23–25]. A coordinate system is attached to each link to facilitate a mathematical description of the mechanism and the relative arrangement of the links,

Figure 5.2. The coordinate system attached to i^{th} link is numbered i. The 4×4 transformation matrix relating coordinate system $i+1$ and i is as follows [23]

$$A_i = \begin{bmatrix} \cos\theta_i & -\sin\theta_i \cos\alpha_i & \sin\theta_i \sin\alpha_i & a_i \cos\theta_i \\ \sin\theta_i & \cos\theta_i \cos\alpha_i & -\cos\theta_i \sin\alpha_i & a_i \sin\theta_i \\ 0 & \sin\alpha_i & \cos\alpha_i & d_i \\ 0 & 0 & 0 & 1 \end{bmatrix}, \tag{5.14}$$

where, the parameters a_i, α_i, d_i, and θ_i are defined so that: a_i is the length of link i, α_i is the angle between the axes of joints i and $i+1$, d_i is the offset along joint i, and θ_i is the rotation angle about axis i.

The closure equation for the 6R spatial linkage is the following matrix equation

$$A_1 A_2 A_3 A_4 A_5 A_6 = A_7. \tag{5.15}$$

This is a direct kinematic problem for a 6R spatial linkage, where the angle θ_1 is known as the input shaft movement, and the angles θ_i, $i = 2, \ldots, 6$ are the unknown quantities and must be solved by the matrix equation, Eqn. (5.15). Besides, the quantities a_i, d_i, α_i, $i = 1, \ldots, 6$, appearing in the matrices on the left hand side of this equation are known and presented in Table 5.1.

The matrix A_7 is the 4×4 transformation matrix description the Cartesian coordinate system 7, attached to the last link with respect to the coordinate system 1, attached to the ground link and can be obtained as follows

$$A_7 = \begin{bmatrix} 0 & \sin(\phi - \frac{\pi}{2}) & \sin\phi & L_1 \sin\phi \\ 1 & 0 & 0 & 0 \\ 0 & \cos(\phi - \frac{\pi}{2}) & \cos\phi & L_1(\cos\phi - 1) \\ 0 & 0 & 0 & 1 \end{bmatrix}, \tag{5.16}$$

where, ϕ is the misalignment angle and L_1 need to be determined for different misalignment angles.

To reduce the complexity of the problem, the Eqn. (5.15) can be rewritten as

$$A_3 A_4 A_5 = A_2^{-1} A_1^{-1} A_7 A_6^{-1}. \tag{5.17}$$

This can be represented in the form

$$\begin{bmatrix} J_{x_1} & K_{x_1} & L_{x_1} & P_{x_1} \\ J_{y_1} & K_{y_1} & L_{y_1} & P_{y_1} \\ J_{z_1} & K_{z_1} & L_{z_1} & P_{z_1} \\ 0 & 0 & 0 & 0 \end{bmatrix} = \begin{bmatrix} J_{x_2} & K_{x_2} & L_{x_2} & P_{x_2} \\ J_{y_2} & K_{y_2} & L_{y_2} & P_{y_2} \\ J_{z_2} & K_{z_2} & L_{z_2} & P_{z_2} \\ 0 & 0 & 0 & 0 \end{bmatrix}, \tag{5.18}$$

where, $\vec{J}_j$, $\vec{K}_j$, $\vec{L}_j$, and $\vec{P}_j$, $j = 1, \; and \; 2$, represent eight vectors of which the components are calculated from Eqn. (5.17). By computing the dot product of vector $\vec{P}_j$ with itself

Table 5.1: Denavit and Hartenberg coordinates of the angled arrangement of the Double Hooke's universal joint.

i	α	a	d
1	$\pi/2$	0	0
2	$\pi/2$	0	0
3	β	0	L_2+L_3
4	$\pi/2$	0	$-(L_2+L_3)$
5	$\pi/2$	0	0
6	0	0	0

for two sides of Eqn. (5.18) and to equalize them, $\vec{P}_1 \cdot \vec{P}_1 = \vec{P}_2 \cdot \vec{P}_2$, the length L_1 can be determined as follows

$$L_1 = \frac{\sqrt{2}\left(L_2 \sin\frac{\beta}{2} + l_{31}\cos\frac{\beta}{2} + \frac{l_{32}}{2}\right)}{\sqrt{1-\cos\phi}}. \tag{5.19}$$

By satisfying $P_{z_1} = P_{z_2}$ from Eqn. (5.18), it can be shown

$$L_1 \sin\phi\cos\theta_1\sin\theta_2 + L_1\cos\theta_2(1-\cos\phi) = (L_2+L_3)(1-\cos\beta)\,, \tag{5.20}$$

where,

$$L_3 = \frac{2l_{31}\cos\frac{\beta}{2} + l_{32}}{2\sin\frac{\beta}{2}}. \tag{5.21}$$

Angle θ_1 can be chosen as the mechanism input. Therefore, the unknown variable θ_2 can be obtained by using the tangent-half-angle formulas from Eqn. (5.20) as follows

$$\theta_2 = 2\arctan\left(\frac{a_2\cos\theta_1 + \sqrt{a_2^2\cos^2\theta_1 - a_1^2 + a_3^2}}{a_1+a_3}\right), \tag{5.22}$$

where,

$$\begin{aligned} a_1 &= 2L_2\sin^2\frac{\beta}{2} + l_{31}\sin\beta + l_{32}\sin\frac{\beta}{2}, \\ a_2 &= L_1\sin\phi, \\ a_3 &= L_1(1-\cos\phi). \end{aligned} \tag{5.23}$$

By equating P_{y_1} and P_{y_2}, $P_{y_1} = P_{y_2}$, θ_3 can be obtained

$$\theta_3 = \arccos\left(\frac{\cos\frac{\phi}{2}\sin\theta_1}{\cos\frac{\beta}{2}}\right). \tag{5.24}$$

By computing the following equation

$$\left(\vec{P}_1 \cdot \vec{P}_1\right)\vec{L}_1 = \left(\vec{P}_2 \cdot \vec{P}_2\right)\vec{L}_2. \tag{5.25}$$

the relationship between the angles θ_2 and θ_5 can be shown as

$$\theta_5 = \theta_2. \tag{5.26}$$

By computing the cross product of vectors $\vec{P}_j$ and $\vec{L}_j$ for two sides of Eqn. (5.18) and to equalize them, $\vec{P}_1 \cdot \vec{L}_1 = \vec{P}_2 \cdot \vec{L}_2$, the kinematic relationship between θ_3, θ_4, and input angular displacement, θ_1 can be given by

$$\theta_4 = \theta_3 = \arccos\left(\frac{\cos\frac{\phi}{2}\sin\theta_1}{\cos\frac{\beta}{2}}\right). \tag{5.27}$$

By equating K_{y_1} and K_{y_2}, the kinematic equation for angular displacement of the output shaft, θ_6, can be written as

$$\sin\theta_3\sin\theta_4 - \cos\beta\cos\theta_3\cos\theta_4 + \cos\phi\sin\theta_1\cos\theta_6 + \cos\theta_1\sin\theta_6 = 0. \tag{5.28}$$

By substituting Eqn. (5.27) into Eqn. (5.28) and using tangent half-angle formula, the output angular displacement, θ_6, can be obtained as a function of the input shaft angle, θ_1

$$\theta_6 = 2\arctan\left(\frac{-1+\tan\theta_1}{1+\tan\theta_1}\right), \tag{5.29}$$

Thus,

$$\theta_6 = \theta_1 - \frac{\pi}{2}, \tag{5.30}$$

in which, the first derivative of this equation with respect to the time gives the input-output angular velocity relationship

$$\omega_6 = \omega_1. \tag{5.31}$$

Therefore, according to Eqn. (5.31), the angled arrangement of the Double Hooke's universal joint is providing a uniform velocity transmission between two angled rotational axes.

5.1.3. PSEUDO-RIGID-BODY MODEL

After the mechanism has been designed and investigated by kinematic synthesis, the Pseudo-Rigid-Body Model (PRBM) is used to create an equivalent compliant design. According to displacement analysis, all four middle joints have limited cycle movement respect to a full cycle rotation of the input axis and can be turned into a flexure-based equivalent. Therefore, the PRBM model can be shown by adding lumped torsional springs at those joints to capture elasticity of equivalent compliant design, see Figure 5.4.

Moreover, this model is used to obtain the relationship between the input and the output torque of the compliant design. The analysis is based on static equilibrium, by

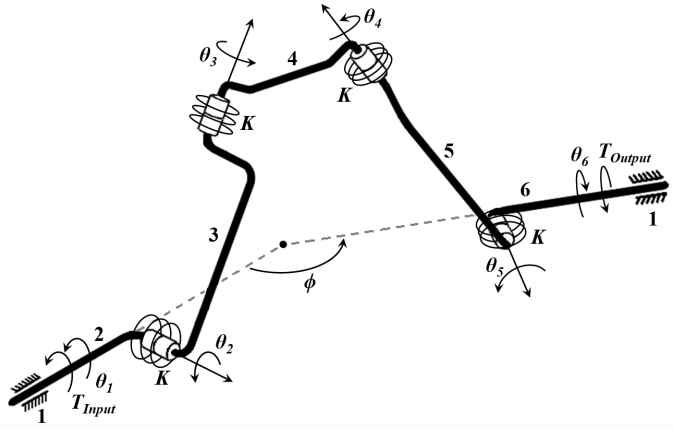

Figure 5.4: Pseudo-Rigid-Body Model (PRBM) of the angled arrangement of the Double Hooke's universal joint.

assuming that masses of compliant parts are negligible. Therefore, static torque analysis can be done using the virtual work principle.

By considering the kinematic analysis, the equality of each two internal angles Eqn. (5.26) and Eqn. (5.27), the virtual work of active forces can be written

$$\delta W = T_{Input}\delta\theta_1 - 2T_{23}\delta\theta_2 - 2T_{34}\delta\theta_3 - T_{Output}\delta\theta_6, \tag{5.32}$$

where, T_{Input} and T_{Output} are the input and the output torques and T_{ij} are the internal moments due to the deflection of the torsional springs between i^{th} and j^{th} link. $\delta\theta_i$ are the corresponding virtual angular displacements.

The torsional spring torques can be given by

$$T_{23} = K(\theta_2 - \Theta_2), \qquad T_{34} = K(\theta_3 - \Theta_3), \tag{5.33}$$

where, Θ_2 and Θ_3 are the initial angles, the undeflected position of the equivalent torsional springs, respectively, and K is the stiffness constant of the compliant joints in their intended motion direction and considered equal for all the joints. For a small length flexure, this can be determined by

$$K = \frac{Ebt^3}{12L}, \tag{5.34}$$

where, E, b, t, and L, are the Young's modulus, the width, the thickness, and the length of the flexures, respectively.

The virtual angular displacement of the output link can be determined as a function of $\delta\theta_1$ from Eqn. (5.30)

$$\delta\theta_6 = \delta\theta_1. \tag{5.35}$$

Similarly, $\delta\theta_2$ and $\delta\theta_3$ can be determined as a function of $\delta\theta_1$ from Eqn. (5.20) and Eqn. (5.28), respectively

$$\delta\theta_2 = -\frac{\sin\phi\sin\theta_1\sin\theta_2}{\sin\theta_2\left(1-\cos\phi\right) - \sin\phi\cos\theta_1\cos\theta_2}\delta\theta_1. \tag{5.36}$$

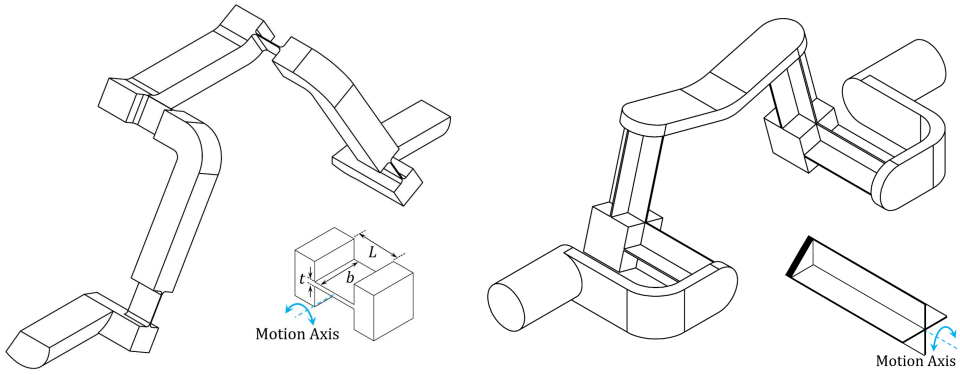

(*a*) (*b*)

Figure 5.5: Proposed compliant configurations for the PRBM model of the angled arrangement of the Double Hooke's universal joint by means of rigid-body replacement synthesis. Replacing the conventional revolute joint by (a) a small length flexure, and (b) a compliant cross flexure.

$$\delta\theta_3 = -\frac{\left(1+\cos\phi\right)\cos 2\theta_1}{2\left(1-\cos\beta\right)\cos\theta_3\sin\theta_3}\delta\theta_1. \tag{5.37}$$

According to the virtual work principle, the necessary and sufficient condition for the equilibrium of a single degree of freedom system is that the generalized forces must vanish in Eqn. (5.32). The input torque can be determined for a given external torque

$$\begin{aligned} T_{Input} = &-2K\frac{(\theta_2-\Theta_2)\sin\phi\sin\theta_1\sin\theta_2}{\sin\theta_2\left(1-\cos\phi\right)-\sin\phi\cos\theta_1\cos\theta_2} \\ &-2K\frac{(\theta_3-\Theta_3)\left(1+\cos\phi\right)\cos\left(2\theta_1\right)}{2\left(1-\cos\beta\right)\cos\theta_3\sin\theta_3} + T_{Output}. \end{aligned} \tag{5.38}$$

Therefore, the minimum actuation torque in different equivalent compliant designs of the angled arrangement of the Double Hooke's universal joint can be determined by replacing the equivalent torsional stiffness of its compliant joints in Eqn. (5.38).

5.1.4. COMPLIANT DESIGN

This section presents different concept solutions to illustrate the compliant design possibilities based on the proposed kinematic. The solutions are defined by discernible differences on the type of compliant joints used instead of rigid-body kinematic pairs, the number of sets, and the coupler link arrangement in the design.

A variety of compliant designs based on the PRBM model of the angled arrangement of the Double Hooke's universal joint, Figure 5.4, can be proposed through rigid-body replacement synthesis. The different compliant revolute joints can be used to satisfy the design criteria. High misalignment angle, compact size, high off-axis stiffnesses (stiffness along degrees of constraint), and low on-axis stiffnesses (stiffness along degrees of freedom) are the main design criteria for the rotational compliant power transmission

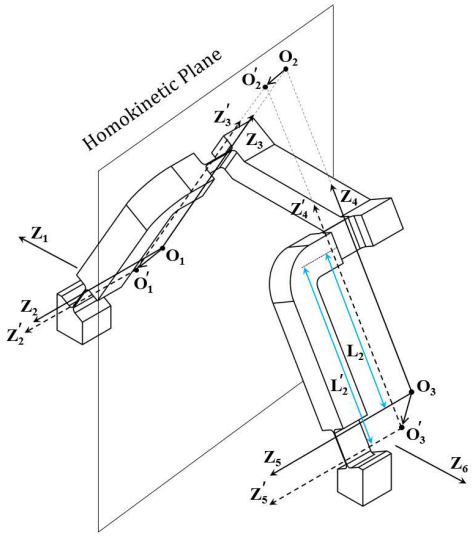

Figure 5.6: Axes deviation of flexures from their original position, axis drift, can not change the homokinetic conditions.

couplings [1]. Two design examples based on two different compliant revolute joints are shown in Figure 5.5. For instance, a small length flexure can be considered to achieve a high misalignment angle within a compact size, Figure 5.5(a), and a compliant cross flexure [26] can be replaced to provide a high off-axis stiffness result in a compliant device with a high torque transmission capacity, Figure 5.5(b).

Axis drift, deviation of the center of rotation in compliant revolute joints as a result of deflection, is not brought up as a design criterion during compliant joint selection since the proposed compliant design is insensitive to this feature. The axis drift is usually an obstacle in the design of compliant mechanisms to accomplish the kinematic of the original rigid-body mechanism. This sometimes can change the kinematic objective of the rigid-body mechanism after converting into the compliant counterpart. The deviation of rotational axes of all flexures for this compliant design is shown in Figure 5.6. As can be seen, all vital constraints between the rotational axes which define the angled arrangement of the Double Hooke's universal joint are still satisfied after deviation. The intersecting point O_2 is moved to point O_2' which is still in the homokinetic plane. It is evident that the effective length of crank links, L_2, is changed after the deviation of rotational axes. However, based on the Eqns. 5.26 and 5.27, the equality of angular displacement, and the resultant the axis drift of the rotational joints at two sides of the homokinetic plane is independent of L_2. Therefore, the axis drift of the flexures in two sides of the homokinetic plane are the same, and as a result, the symmetrical condition for uniform velocity transmission is fulfilled.

According to the DoF analysis, at least three sets of the proposed compliant designs are required to constrain the design to behave as a universal joint, two different combinations of the fully compliant homokinetic coupling are shown in Figure 5.7. As can be seen, there are two possible ways to arrange the coupler link. Each set can be decoupled

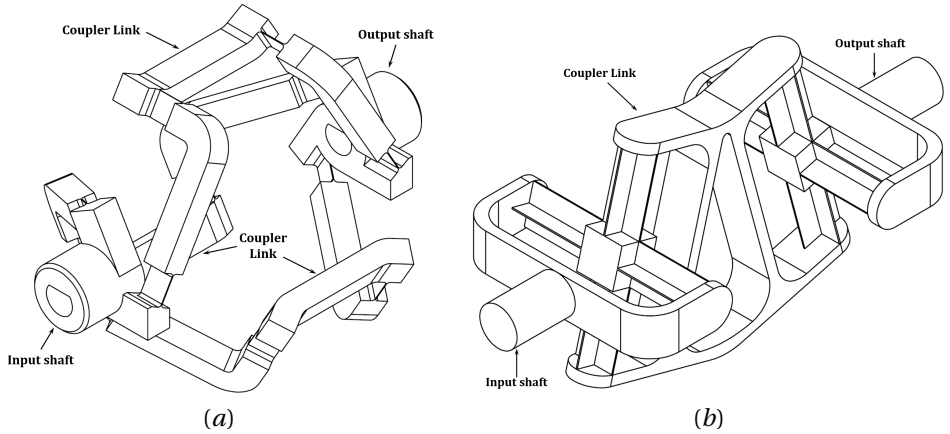

Figure 5.7: Fully compliant homokinetic couplings based on the angled arrangement of the Double Hooke's universal joint, (a) there is one decoupled coupler link corresponding to each compliant set, (b) all the compliant sets sharing one coupler link and move simultaneously.

from each other with their coupler link, see Figure 5.7(a). Therefore, as the sets are separated, the combination will allow for a high misalignment angles without any collision between the links and coupler links. As it is shown in Figure 5.7(b), for the second type of combination, all sets share one coupler link and move synchronously. However, this arrangement can not accommodate for high misalignment angles as the compliant flexure might collide with the coupler link.

There is an error motion between the input and the output angular displacement when a compliant coupling is loaded due to the elastokinematic effects. This mainly depends on the input-output rotational stiffness (K_r), stiffness in the rotation transmission direction, of the compliant coupling and the output torque (T_{Output}). The input-output angular displacement relationship, Eqn. 5.30, can be rewritten for the compliant homokinetic coupling as

$$\theta_6 = \theta_1 - \frac{\pi}{2} - \frac{T_{output}}{K_r}, \tag{5.39}$$

Therefore, uniform velocity transmission, Eqn.5.31, is still valid since K_r is constant during a full cycle rotation, and assuming the output torque is constant.

5.1.5. FABRICATION AND EXPERIMENTAL EVALUATION

This section presents a case study that proves the findings of this research and demonstrates the usefulness of compliant homokinetic coupling as a compliant transmission mechanism. The design and prototype are described in more details, and the results are then evaluated by experimental setups and finite element modeling.

PROTOTYPE

The design, which is shown in Figure 5.7(a), is dimensioned and fabricated for the experimental evaluation. The selected combination will allow studying the behavior of the

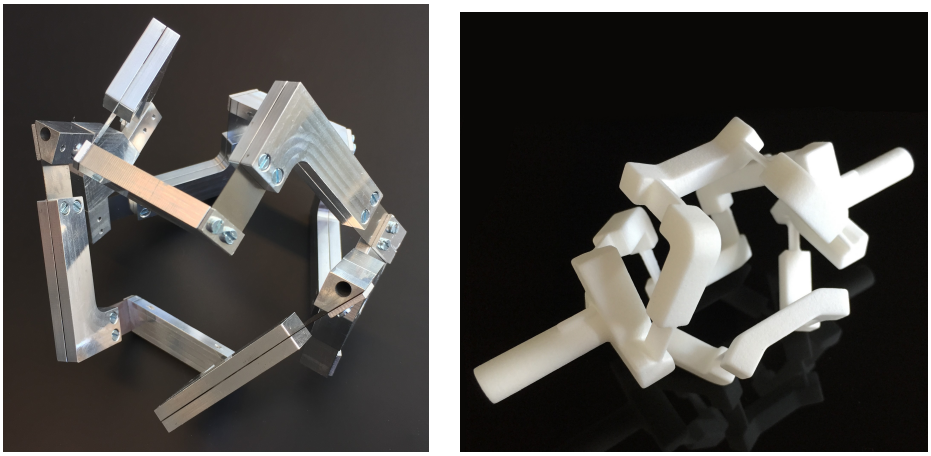

(*a*) (*b*)

Figure 5.8: The prototypes of the fully compliant homokinetic coupling, compliant CV joint. (a) An Aluminum prototype fabricated for experimental evaluations, the rigid parts are fabricated out of Aluminum, and the flexures are cut out of austenitic stainless steel. (b) A single-piece demonstrator printed out of plastic.

compliant homokinetic coupling with the minimum number of sets, high misalignment angle, and a simplified design for fabrication. An aluminum prototype with the flexures out of stainless steel AISI316L was made, Figure 5.8 (a). The set of parameters that defined the geometry and stiffness are summarized in Table 5.2. The mechanism is dimensioned to provide 45° misalignment angle. The maximum misalignment angle, $\psi = \pi - \phi$, was limited by the yield strength of austenitic stainless steel AISI316L: 500 MPa. The relevant material specifications are $E = 183\ GPa$, and $\rho = 7.9\ gr/cm^3$. For a misalignment angle of $\psi = 45°$, the kinematic analysis predicted a maximum range of motion of 22.5° for each compliant joint of the design during a full cycle movement.

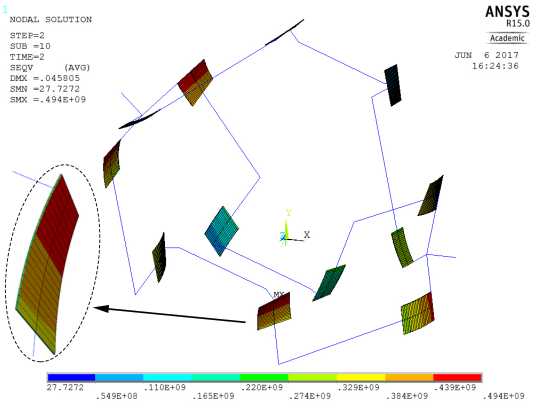

Figure 5.9: Predicted stress of the compliant homokinetic coupling under 45° misalignment angle between the input and the output axes.

Table 5.2: Prototype design parameters for the fully compliant homokinetic coupling, compliant CV joint.

Parameters	Values
l_{31}	4 mm
l_{32}	32 mm
L_2	40 mm
β	60°
L	12 mm
b	10 mm
t	0.2 mm

The input-output rotational stiffness (K_r), and the actuation stiffness are studied by the finite element model, which the results are presented in the next section. Besides, the results are also evaluated to ensure the maximum Von Mises stress is lower than the material tensile yield strength. A parametric finite element model was created in ANSYS for the analysis of the compliant homokinetic coupling, shown in Figure 5.9. The beam element based on the Timoshenko beam theory, BEAM188, was used for the small length flexures, and MPC184 was used for the rigid links. The boundary conditions were applied in different time steps for the two different cases. In the first step for all cases, the misalignment angle of 45° is applied while the input axis was fixed in all directions

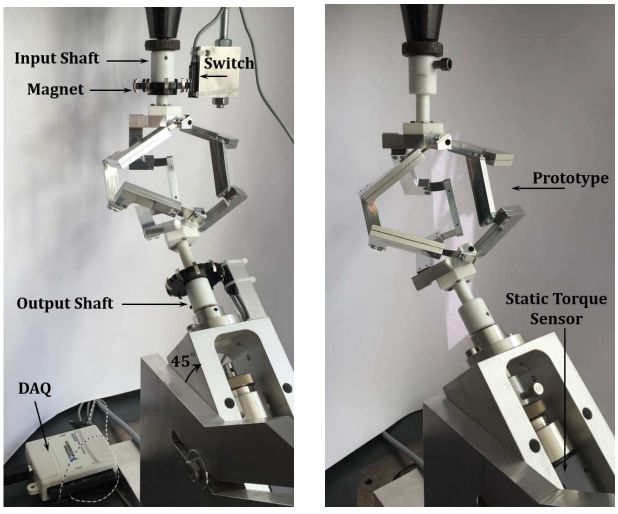

(*a*) (*b*)

Figure 5.10: The measurement setups (a) to analyze the input-output angular velocity relationship, (b) to study the input-output rotational stiffness, K_r, of the design. In both figures, the setup is adjusted for the misalignment angle of $\psi = 45°$.

and the output axis was free. For the first case, modeling the rotational stiffness of the design, the output axis was fixed in all directions, and the input was only free to rotate around itself. In the second case, actuation stiffness analysis, both shafts were free to rotate around their axis and fixed for all the other degrees of freedom.

EXPERIMENTAL EVALUATION

A velocity measurement setup was built to experimentally evaluate the kinematic characteristic of the fully compliant homokinetic coupling, Figure 5.10(a). The input shaft of the prototype is connected to the drive motor and is actuated at different angular velocities. The driven shaft is free to rotate around the output axis, and its position can be adjusted for different misalignment angles. Two discs with 10 magnets are attached on each shaft to study the input-output angular velocity relationship. The circuits will be closed while one of the magnets is facing to the switch sensor. The data was read by using a data acquisition module, DAQ, and their waveform was then recorded. As can be seen in Figure 5.11, the experimental data verify the uniform velocity transmission of the fully compliant homokinetic coupling for different misalignment angles. It is observed that the maximum error between the theoretical and the experimental results is about 0.8%.

A static torque measurement setup was constructed to investigate the input-output rotational stiffness, K_r, of the proposed compliant homokinetic coupling, Figure 5.10(b). The input shaft was connected to a rotational motor, and the output shaft was directly connected to the static torque sensor, HBM T20WN, which was mounted on an adjustable stage for different misalignment angles. The input shaft was actuated, and the

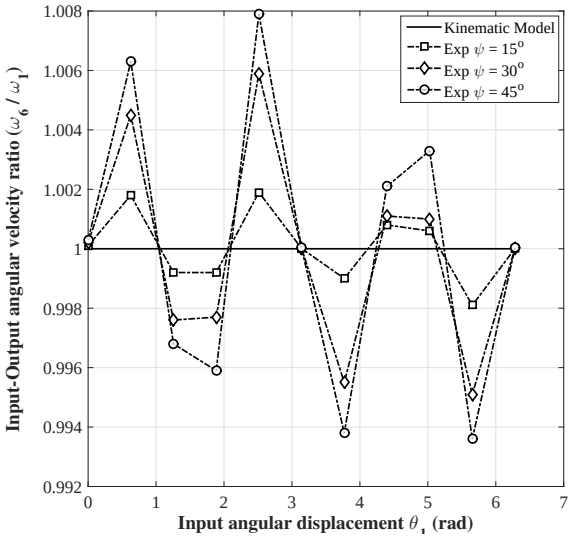

Figure 5.11: The kinematic model and experimental data for the input-output angular velocity relationship of the compliant homokinetic coupling. The experimental data was recorded at three different misalignment angles, $\psi = 15°$, $30°$, and $45°$.

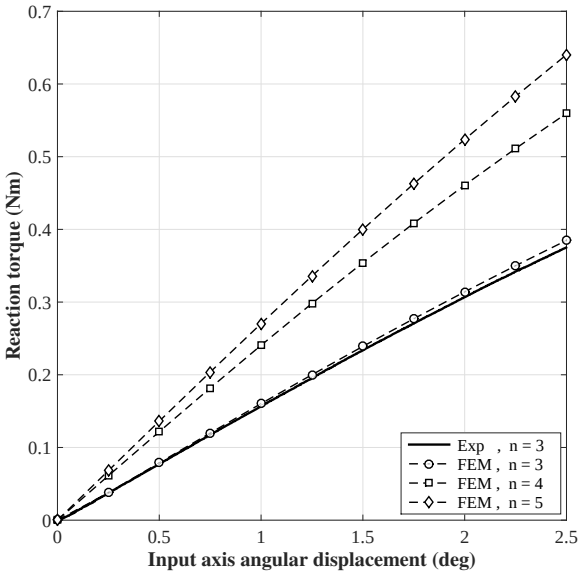

Figure 5.12: Results of the moment-angular displacement characteristic, the input-output rotational stiffness K_r, of the compliant homokinetic coupling at $\psi = 45°$ misalignment angle. Experimental data (Exp) was evaluated for the design with three compliant sets, $n = 3$. Besides, finite element modeling (FEM) are shown for three, four and five compliant sets, $n = 3$, 4, and 5.

reaction torque at the output shaft was measured by the static torque sensor which was linked to the angular displacement of the input shaft. The results for 45° misalignment angle, both from experimental data and finite element modeling, are shown in Figure 5.12. Moreover, the torque capacity of the design for more number of the compliant sets are predicted by finite element modeling. As can be seen, by increasing the number of sets the maximum torque transmission capability of the compliant homokinetic coupling is increased.

As can be seen in Figure 5.13(a), a measurement setup was made to study the actuation torque required to deal with the internal stiffness of the design, the stiffness of the design while the output is free. The setup was performed for $\psi = 45°$ misalignment angle, and the data was recorded and analyzed for one full cycle rotation of the device.

Figure 5.13(b) shows the results of the experiment, PRBM model, and the finite element modeling of the actuation stiffness of the compliant homokinetic coupling. The results are for the different number of compliant sets during a full cycle rotation, and with $\psi = 45°$ as misalignment angle for all cases. The experimental results support the finite element modeling of the design with three compliant sets, $n = 3$, where the maximum error between them increases to about 25%. Besides, it is verified that the results from finite element modeling are consistent with the PRBM model. However, there is a difference which is corresponding to the fact that the small length flexures also allow for a small torsion rather than a pure bending only, this can be seen in Figure 5.9. The differences will be increased when the transmission mechanism is loaded at the output

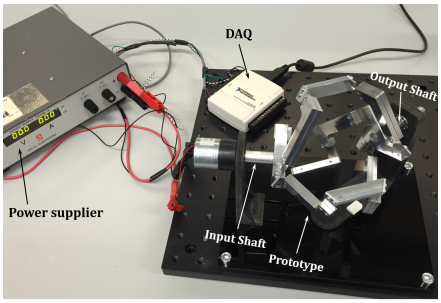

(*a*)

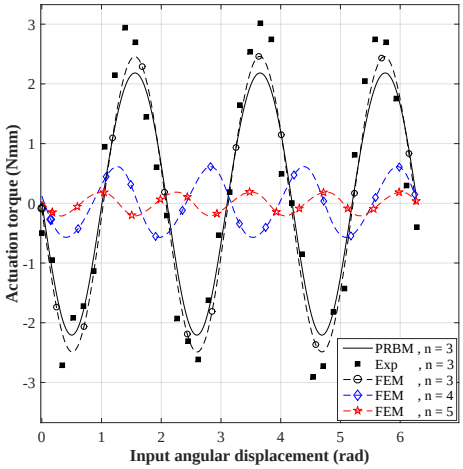

(*b*)

Figure 5.13: Actuation torque required to deal with the internal stiffness of the compliant homokinetic coupling. (a) Measurement setup to evaluate the actuation stiffness. (b) Results from finite element modeling (FEM), PRBM model, and experimental evaluation (Exp) for different number of compliant sets, $n = 3$, 4, and 5. The results for all cases were performed at $\psi = 45^\circ$ misalignment angle.

axis. Moreover, the effect of increasing the number of compliant sets on actuation torque are shown in Figure 5.13(b). As can be seen, by increasing the number of compliant sets the minimum actuation torque required to deal with the internal stiffness of the device is decreased. Therefore, it can be concluded the designed compliant device is a nearly statically balanced compliant power transmission coupling. This is mainly due to the fact that the designed compliant device can be preloaded while applying the misalignment angle between the input and the output axes. The design is nearly statically balanced since the number of compliant sets is limited. However, by having an infinite number of compliant sets around the rotational axes, this design can theoretically be fully statically balanced.

5.2. COMPLIANT COUPLING FOR LATERAL MISALIGNMENT

5.2.1. INTRODUCTION

There are different types of applications where a constant velocity transmission coupling, which can transfer a rotational power between parallel axes, can be applied. It can be used in micro/meso scale transmission systems where two gears with the same number of tooth have been used [27, 28]. Moreover, such a power transmission coupling can accommodate with lateral alignment errors, parallel misalignment, between rotational axes. This is a need in many applications such as precision measurements, micro engines, laser processing, and etc [29]. In state of the art, several kinds of constant velocity joints have been invented to accommodate with alignment errors [1]. However, these are made based on rigid-body mechanisms, and like gears, they are leading to many disadvantages such as wear, friction, backlash, need for assembly, maintenance, and lubrication. Besides, sometimes a precise or expensive assembling process is essential to have a proper transmission or gearing mechanism in micro scale applications [30].

Compliant mechanisms have shown a great potential in affording new solutions, to deal with above-mentioned obstacles, for power transmission mechanisms [31–34]. Compliant mechanisms gain their motion from elastic deformation of flexible members rather than from rigid-body kinematic pairs [13]. These mechanisms are a favorable choice in the field of precision engineering due to the elimination of rigid-body kinematic joints, which eliminates the disadvantages of rigid-body linkages.

Several patents on near-constant velocity flexible couplings, which can accommodate small alignment errors, were found in literature [35, 36]. The designers have considered an extra degrees of freedom, either by using wire flexures or an extra flexure, to enable the devices for angular misalignment as well as lateral misalignment. However, this will allow for a non-constant velocity rotation transmission between the input and the output axes due to the asymmetric linkage arrangement with respect to the homokinetic plane [19]. Besides, designs sometimes contain simple compliant four-bar mechanisms to approximate straight-line movement to compensate for lateral misalignments. However, this approximation also leads to a nonuniform velocity transmission [37].

conventional rigid-body pairs offer near zero stiffness around the motion axis and high stiffness along the constrained axes. However, compliant kinematic pairs require significant force and energy due to the elastic deformation of the flexible members. Therefore, a compliant mechanism offers a poor efficiency, and it requires continuous force to hold the mechanism in position [38]. This results in several disadvantages for compliant transmission mechanisms such as nonuniform torque/force transmission, deficient travel range, low speed, and demanding for larger actuators. However, the deformation energy is stored in flexible members. Therefore, the mechanism can be statically balanced as the elastic force is a conservative force. As a result, these mechanisms can be actuated with much less energy as compared to the unbalanced compliant design [38–41].

The aim of this section is to design a compliant and statically balanced constant velocity power transmission mechanism between two parallel rotational axes with a lateral offset. The design is furthermore required to be planar, making it desired for micro fabrication techniques such as double sided Deep Reactive Ion Etching (DRIE).

The design of the proposed compliant transmission mechanism is described in the

following subsections. The kinematic of Oldham coupling is explained in Section 5.2.2. The Pseudo-Rigid-Body model (PRBM) and static balancing are studied and developed in Section 5.2.3. The compliant design is illustrated and the torque transmission capability is discussed by the theoretical model in Section 5.2.4. The proposed compliant design is then evaluated experimentally in Section 5.2.5.

5.2.2. KINEMATICS

The compliant transmission mechanism, proposed in this chapter, is created by employing conventional kinematic synthesis and corresponding Pseudo-Rigid-Body Model (PRBM). This section describes the rigid-body kinematic of the design, which is based on the rigid-body Oldham coupling. Moreover, the PRBM model is introduced to develop the static balancing and study the torque transmission capability of the equivalent compliant design.

The rigid-body Oldham coupling is a four-bar mechanism, RPPR, for constant velocity rotation transmission between two parallel rotational axes with a lateral offset [37]. There are three mobile links in this mechanism. The first and second links are rotating around the input and the output axes, respectively. The third link, which is a middle component, is then connected to the first and second links by two prismatic joints which their motion axes are perpendicular to each other. The schematic of the Oldham coupling and its simplified geometrical representation are shown in Figure 5.14.

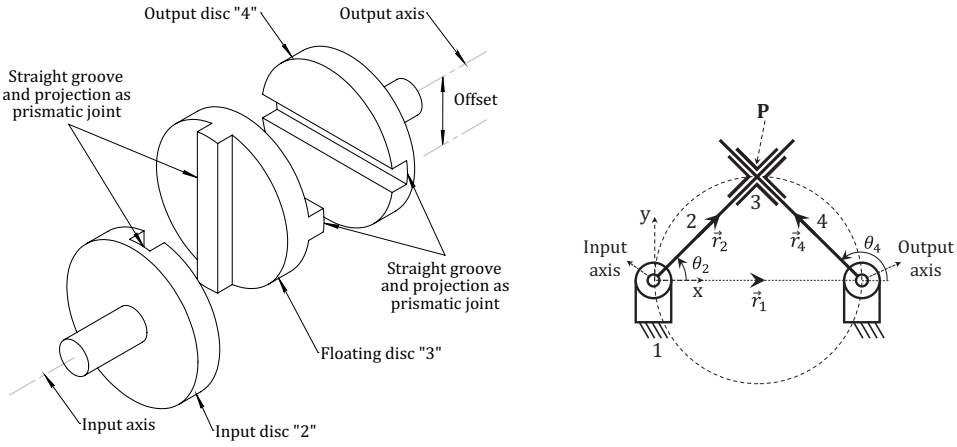

Figure 5.14: Oldham coupling (a) Rigid-Body schematic (b) Simplified geometrical representation

When the input axis rotates through some angle, θ_2, the floating disc, link 3, rotates through the same angle. This in turn rotates the output axis, link 4, through the same angle but with 90° phase shift due to the right angle between the two prismatic joints,

$$\theta_4 = \theta_2 + \frac{\pi}{2}. \tag{5.40}$$

Therefore, there is a uniform, one-to-one, rotational velocity transmission between

the input and the output axes, i. e. $\omega_4 = \omega_2$.

The position of the sliders, r_2 and r_4, varies during full cycle movement of the mechanism and for a given input angle, θ_2, can be expressed

$$r_2 = L_1 \cos\theta_2, \qquad r_4 = L_1 \sin\theta_2. \tag{5.41}$$

where, L_1 is the offset between the input and the output axes and considered as the length of the ground link.

Therefore, the maximum displacement required at the prismatic joints can be given by

$$\Delta r_2 = \Delta r_4 = 2L_1. \tag{5.42}$$

5.2.3. PSEUDO-RIGID-BODY MODEL

In order to study the static balancing conditions of the compliant design, a PRBM model for the Oldham coupling is presented, as shown in Figure 5.15. The sliders joined by a pin joint are considered at each rotational axes since the mechanism will be connected to the input and the output rotating axes. Therefore, the two sliders in the PRBM model, which the input and the output axes are suspended on each, are replaced by two linear springs.

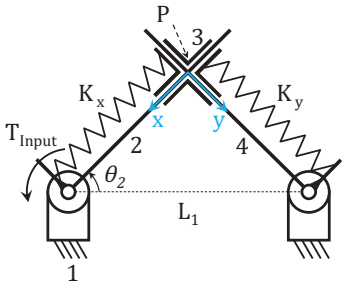

Figure 5.15: The proposed Pseudo-Rigid-Body model for the Oldham coupling with the sliders joined at the axes by a pin joint.

As the rotational axes will be suspended by a series combination of the linear flexure bearings, the torque transmission capability is limited by their in-plane rotational stiffness, K_θ, within the stress limit of the flexible material. Moreover, depends on different linear flexure bearings used in compliant design, the in-plane rotational stiffness of linear flexure bearings may be depends on their displacement with respect to their rest position, r_2 and r_4, due to the elastokinematic effects. Therefore, the overall in-plane rotational stiffness of the device, i.e. transmission stiffness, K_m, can be given by

$$K_m = \frac{K_\theta(r_2) K_\theta(r_4)}{K_\theta(r_2) + K_\theta(r_4)}. \tag{5.43}$$

ENERGY EQUATION AND STATIC BALANCING

If the compliant elements are replaced at each prismatic joint, the mechanism can be modeled as illustrated in Figure 5.15. The energy equation can be given by adding the energy storage terms for each linear springs

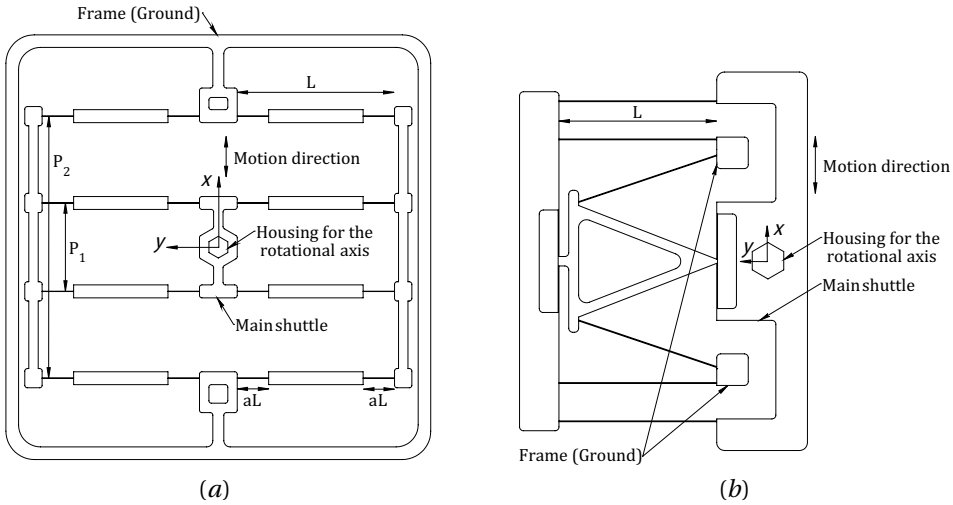

Figure 5.16: Two linear flexure bearings with their geometrical parameters (a) Paired Double Parallelogram flexure (DP-DP), and (b) Double Parallelogram flexure with Nested Linkage (DP-NL).

$$V_e = \frac{1}{2}\left(K_x x^2 + K_y y^2\right) \tag{5.44}$$

where, K_x and K_y are the spring constant in motion direction of the sliders as shown in the Figure 5.15, and the x and y are the deflection of each spring.

The principle of virtual work can be applied to drive the input torque, T_2, which can be given by

$$T_2 \delta\theta_2 - \delta V_e = 0. \tag{5.45}$$

The mechanism can be statically balanced, $T_2 = 0$, by having a constant value for total elastic potential energy of the mechanism over different input angle. This can be accomplished by having two zero length linear springs K_x and K_y with a constant and equal stiffness coefficient, i.e. $K_x = K_y = K$. Moreover, the input and the output axes have to be collinear, $L_1 = 0$, when the linear springs are located at their rest positions, point P. As a result, the total potential energy of the mechanism is constant and can be rewritten as

$$V_e = \frac{1}{2}K\left(x^2 + y^2\right) = \frac{1}{2}KL_1^2 = const. \tag{5.46}$$

Therefore, any equivalent compliant design based on the proposed PRBM model, Figure 5.15, and the above-mentioned conditions can be statically balanced.

5.2.4. COMPLIANT DESIGN

The rigid-body replacement synthesis [13] is considered to design the compliant rotation transmission mechanism based on the proposed PRBM model, shown in Figure 5.15. The two frictional prismatic joints, which are the main sources of the energy lose, can

Table 5.3: Qualitative comparison of different types of linear flexure bearings reported in prior art. Double Parallelogram flexure (DP), Paired Double Parallelogram flexure (DP-DP), Clamped Paired Double Parallelogram flexure (C-DP-DP), Double Parallelogram flexure with External Linkage (DP-EL), Double Parallelogram flexure with Nested Linkage (DP-NL), Double Tilted flexure (DT). For the first three criteria, the DP-DP design is considered as good solution (0) for comparison. The excellent and poor performance are indicated by (+) and (−), respectively. For the last criterion, the designs with one grounding point are scored by (+) and those with more than one grounding points are scored by (−).

Linear flexure bearings	Criteria			
	Stroke over footprint	In-plane rotational stiffness	Dynamic performance	Ease of integration into PRBM model
DP [42]	+	−	−	+
DP-DP [43]	0	0	0	+
C-DP-DP [44]	−	0	0	+
DP-EL [29, 45, 46]	−	+	+	−
DP-NL [47]	−	+	+	−
DT [48, 49]	−	0	0	+

be replaced by the linear flexure bearings and hence the PRBM model can be converted into a single-piece compliant design. In order to have a uniform velocity transmission, a precise rectilinear flexure bearing is required as replacement of prismatic joints in the PRBM model.

A brief overview and a qualitative comparison of different linear flexure bearings reported in literature, which provide precise rectilinear motion, is presented in Table. 5.3. Stroke over footprint, in-plane rotational stiffness, dynamic performance, and ease of integration into the PRBM model for fabrication are considered as the design criteria to compare different linear flexure bearings.

Designers might weight each of the above mentioned criteria differently based on their design requirements, and select different linear flexure bearings for the integration into the proposed PRBM model. As can be seen in the Table. 5.3, Double Parallelogram flexure with Nested Linkage (DP-NL), shown in Figure 5.16(b), and Double Parallelogram flexure with External Linkage (DP-EL) giving better in-plane rotational stiffness and dynamic performance. However, the frame (ground) parts of this type of linear flexure bearings are apart and can not be connected in the same plane, as shown in Figure 5.16(b). As a consequence, at least five design layers are required to convert the PRBM model into a compliant embodiment. Therefore, the whole transmission mechanism can not potentially be fabricated with micro planar fabrication technique such as double sided DRIE [50], which allow for maximum three design layers. More alternatives, for the linear flexure bearings based on the DP-NL and the DP-EL, can be found in prior art where there is a single ground member [51]. However, this will end up to a much larger footprint of the design as the external linkages need to be placed inside of the mechanism.

The Paired Double Parallelogram flexure (DP-DP) design, shown in Figure 5.16(a), offering a good trade off between all criteria. The single ground link is also made it desired

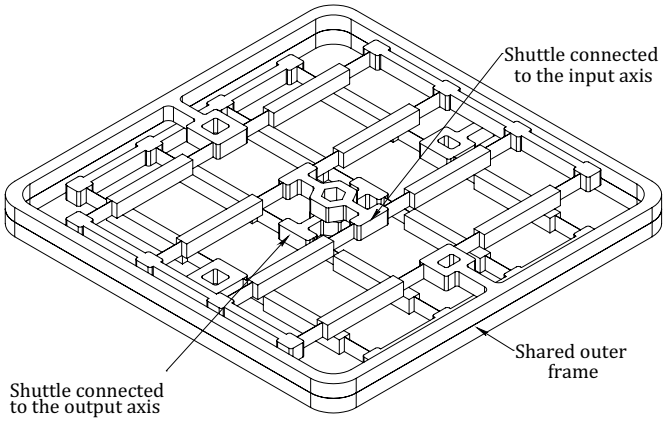

Figure 5.17: Statically balanced fully compliant transmission mechanism based on the proposed PRBM model of the Oldham coupling.

for planar fabrication technique. Therefore, in this study, a DP-DP linear flexure bearing, is selected for further design process and model validation.

As can be seen in Figure 5.17, a statically balanced fully compliant power transmission mechanism, compliant equivalent of the PRBM model shown in Figure 5.15, is designed by using DP-DP linear flexure bearing. The two linear flexure bearings are placed on top of each other with 90° offset between their motion directions. They are connected to the input and the output axes by the housing which are considered on their main shuttles. Both flexure bearings share their frame (ground), which is corresponding to the Link 3 in equivalent PRBM model shown in Figure 5.15.

The torque transmission capability of the design is corresponded to the in-plane rotational stiffness, K_θ, of the selected linear flexure bearings within the stress limit of the material. The closed-form nonlinear stiffness for the DP-DP linear flexure bearing is a function of the location of the main shuttle with respect to the frame, x, and can be given by [48]

$$K_\theta(x) = \frac{Ewt^3\kappa P_1^2 P_2^2}{12L^3\left(P_1^2+P_2^2\right)\left(1+\kappa\lambda\left(\frac{x}{2L}\right)^2\right)}, \tag{5.47}$$

where, w and t are flexure width and thickness, respectively, and

$$\lambda = \frac{2a^3\left(105-630a+1440a^2-1480a^3+576a^4\right)}{175\left(3-6a+4a^2\right)^3}, \qquad \kappa = \frac{6L^2}{at^2}. \tag{5.48}$$

By substituting Eq. 5.41 and Eq. 5.47, into Eq. 5.43, the in-plane rotational stiffness, transmission stiffness, of the proposed compliant design, K_m, can be given by

$$K_m = \frac{Ewt^3\kappa P_1^2 P_2^2}{12L^3\left(P_1^2+P_2^2\right)\left(2+\kappa\lambda\left(\frac{L_1}{2L}\right)^2\right)}. \tag{5.49}$$

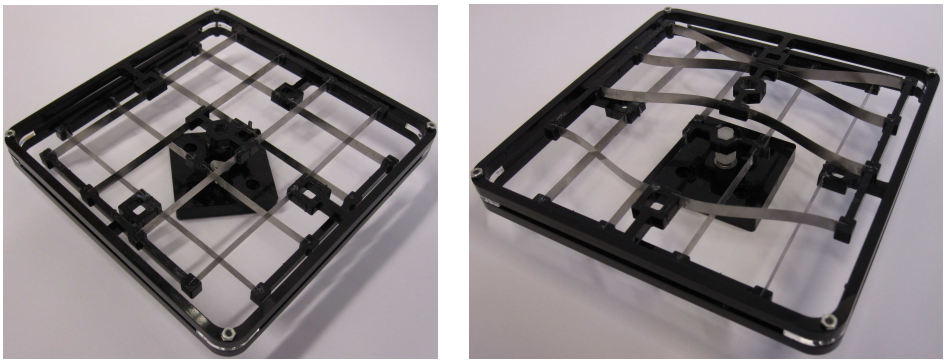

(*a*) (*b*)

Figure 5.18: The large scale prototype of statically balanced fully compliant power transmission mechanisms, (a) at the rest position, and (b) at the deflected position, 20mm lateral offset.

Therefore, as can be seen in Eq. 5.49, the transmission stiffness of the proposed PRBM model and the compliant design is a constant value over a full cycle rotation of the input axis, i.e. it is independent from the location of the main shuttle, where the axes are attached, with respect to the frame. Moreover, the torque transmission capability of the device can be independently increased by a proper choice of the parameters P_1 and P_2 such that it does not effect the maximum range of motion of the shuttles.

The distribution of compliance in a compliant transmission mechanism give raise to elastokinematic effects, which in the case of a compliant coupling results in error motion between the input and the output rotations. This error depends on the output load, T_{out}, and the transmission stiffness of the coupling, K_m. Therefore, the input-output kinematic relationship of the Oldham coupling, Eq. 5.40, for an equivalent compliant design can be rewritten as

$$\theta_4 = \theta_2 + \frac{\pi}{2} - \frac{T_{out}}{K_m}. \tag{5.50}$$

Assuming a constant output torque, the equivalent compliant coupling yet provides a constant velocity transmission, i. e. $\omega_4 = \omega_2$, since the transmission stiffness, K_m is constant based on the Eq. 5.49.

5.2.5. FABRICATION AND EXPERIMENTAL EVALUATION

Fabrication and experimental evaluations of the proposed compliant rotational power transmission mechanism are discussed in this section. Two features of the compliant design will be evaluated experimentally. These are the static balancing of the compliant transmission mechanism and the input-output rotational stiffness, transmission stiffness, of the compliant device. Besides, the results from experiments, finite element modeling (FEM), and theoretical modeling will be illustrated and discussed in this section.

Table 5.4: Prototype design parameters of statically balanced fully compliant rotational power transmission mechanism.

Parameters	$L(mm)$	$t(mm)$	$w(mm)$	a	$P_1(mm)$	$P_2(mm)$
Values	50	0.2	5	0.5	28	84

PROTOTYPE

A macro scale device was constructed for the experimental evaluation, Figure 5.18 (a). The austenitic stainless steel AISI316L is selected for the flexible members. The device is designed and dimensioned for a maximum lateral offset of 20 mm, Figure 5.18 (b), which is limited by the yield strength of AISI316L rated at 500 Mpa. The prototype design parameters of the statically balanced fully compliant transmission mechanism are given in Table 5.4.

EXPERIMENTAL EVALUATION

The static balancing feature of the proposed compliant transmission mechanism is investigated experimentally by two approaches. The mechanism is able to remain at any arbitrary position without requiring any effort, as shown in Figure 5.19.

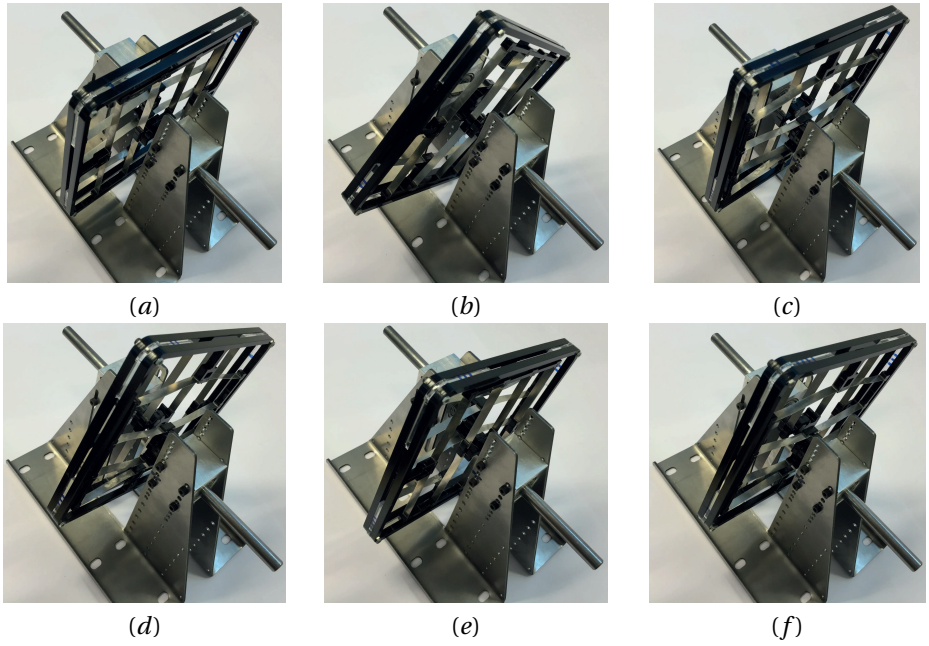

Figure 5.19: The proposed compliant transmission mechanism is statically balanced and can remain at any position without requiring a continues torque to hold the mechanism in position. Blue lines indicated on the middle glassy part of prototype are indicating the mechanism at different position.

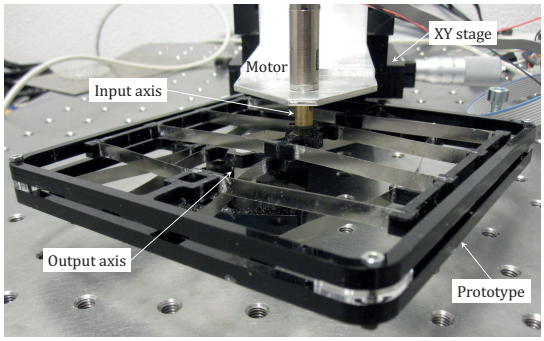

Figure 5.20: Experimental setup for the actuation torque measurement.

As it is shown in Figure 5.20, an experiment was performed to study the actuation stiffness of the compliant device. This is done by studying the input torque at the input axis, while the output axis was unloaded. The motor was mounted on an XY stages to provide the lateral offset between the axes. The input axis was attached to the housing of the main shuttle from the upper DP-DP linear flexure bearing. The output axis, was only free to rotate and attached to the lower DP-DP linear flexure bearing. First, the actuation torque was measured without any lateral offset between the rotational axes, where both linear flexure bearings where at their rest positions during a full cycle motion. This torque corresponded to the inertia of the device, the frictions at the bearing where the output axis was grounded, and the other sources of energy loss in the measurement setup. Further, the actuation torque was recorded after applying a lateral offset of $L_1 = 20mm$, and this amount was subtracted from the first torque measurement

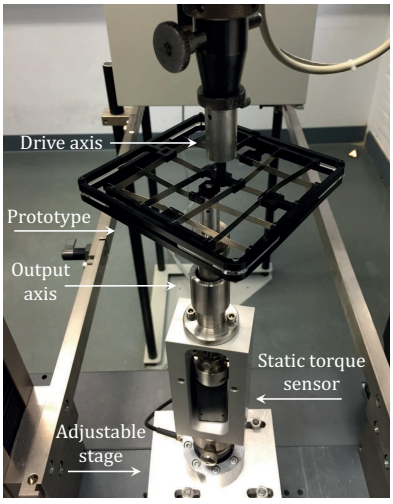

Figure 5.21: The measurement setup to analyze the transmission stiffness of the prototype. The measurement was performed at $L_1 = 20mm$, the lateral offset between the axes.

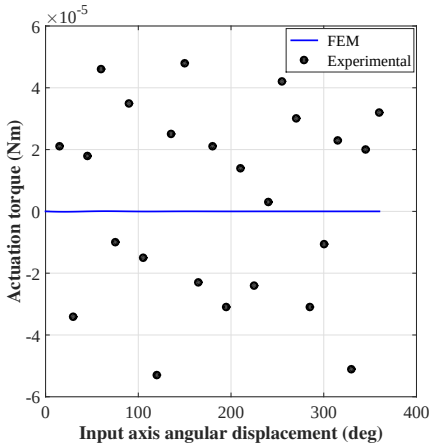

Figure 5.22: Results of the experiment and finite element modeling (FEM) for the actuation torque of the proposed compliant transmission mechanism. The measurement was performed at 20mm lateral offset between the input and the output axes.

and shown as the input torque required to deal with the internal stiffness of the device. Moreover, a setup was constructed for experimental evaluation of the in-plane rotational stiffness, transmission stiffness, of the compliant transmission mechanism, shown in Figure 5.21. The output axis is directly mounted on a static torque sensor, HBM T20WN. Besides, the torque sensor is attached to an adjustable stage to tune for lateral offset between the axes. The drive axis is connected to the housing of the main shuttle from the upper DP-DP linear flexure bearing and was actuated for some angles. The reaction torque at the output axis is then recorded with respect to the input rotation.

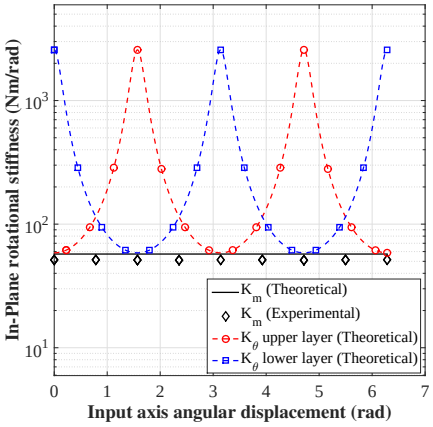

Figure 5.23: The results from experiment and the theoretical model for the in-plane rotational stiffness, transmission stiffness, of the statically balanced compliant transmission mechanism and each DP-DP linear flexure bearing of the design at different input axis angular displacement.

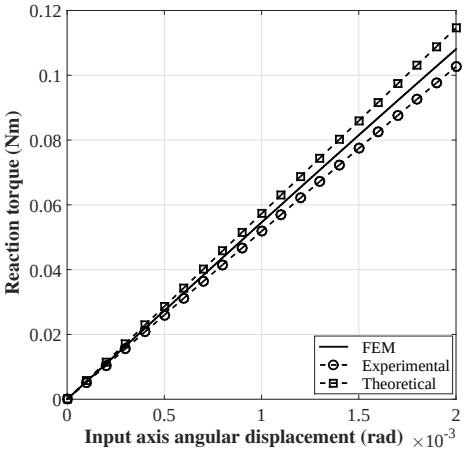

Figure 5.24: Torque-Angular displacement characteristic of the statically balanced compliant transmission mechanism. The results are from experiment, finite element modeling (FEM), and the theoretical model. These were recorded at $L_1 = 20mm$, lateral offset between the axes.

5

The measurement result for the actuation torque is shown in Figure 5.22. As it is shown, the measurement result and FEM modeling indicate the compliant design based on the proposed PRBM model is statically balanced as this was also proven by the theoretical model in Section 5.2.2. However, the measurement shows some torque was still needed to force the device. This was mainly due to the friction which was increased at the bearing of the output axis, caused by the reaction force from deflected linear flexure bearings, while applying the lateral offset between the axes.

The transmission stiffness of the macro scale prototype based on the theoretical model and experiment are shown in Figure 5.23. As can be seen, an in-plane rotational stiffness of $K_m = 57.29\ Nm/rad$ is predicted by the theoretical model. As aforementioned, shown in Eq. 5.49, the in-plane rotational stiffness of the device is independent from the angular displacement of the input axis. This means the mechanism has a constant in-plane rotational stiffness at any location of the input axis during a full cycle rotation, shown in Figure 5.23. Although, the in-plane rotational stiffness of the belonging DP-DP linear flexure bearings are not constant during the full cycle rotation of the mechanism.

Besides, the torque-angular displacement characteristic are shown in Figure 5.24. These were evaluated by the experiment, theoretical model, and finite element modeling. As can be seen, the device is capable to transfer more than 100 Nmm torque, at lateral offset of $L_1 = 20\ mm$, within 500 Mpa stress limit. An in-plane rotational stiffness of 51.35 Nm/rad and 54.05 Nm/rad were recorded through experiment and finite element modeling, respectively. The results from experiment and finite element modeling agree with the theoretical model within 5.66 % and 10.37 %, respectively.

5.3. CONCLUSIONS

First large deflection and fully compliant homokinetic coupling for angular misalignments is presented and its principle is described in the first section of this chapter, Section 5.1. The kinematic and Pseudo-Rigid-Body Model (PRBM) of the proposed compliant design were studied. It was shown, the uniformity of the rotation transmission of the device is insensitive to the axis drift of the used flexures. Moreover, a prototype was manufactured and evaluated by experimental data, and it is shown that the results support the kinematic model, PRBM model, and the finite element modeling. The results indicate that by increasing the number of compliant sets around the rotational axes the required actuation torque will be reduced significantly and the device can be labeled as a nearly statically balanced compliant power transmission coupling. Moreover, the increase in the number of the compliant set enhances the torque transmission capability, by increasing the rotational stiffness of the compliant design. It can be concluded that the proposed compliant homokinetic coupling is feasible and may have great potential in micro measurement systems, medical devices, power transmission systems, and precision instruments.

In the next section, Section 5.2, a compliant and potentially monolithic transmission coupling for lateral misalignment is presented. The design is generated based on the proposed Pseudo-Rigid-Body model (PRBM) of Oldham coupling. Moreover, The PRBM model is applied to develop for static balancing and study torque transmission capability of the design. It was shown the proposed fully compliant design is statically balanced and therefore can be expressed as a high efficient power transmission mechanism. Moreover, the static balancing feature of the design makes it suitable for high torque applications, where the high stiffness of the linear flexure bearings will not effect on the required actuation torque. Although this will increase the effort to make the lateral offset between the input and the output axes. The design can be fabricated by common micro scale manufacturing process such as double sided Deep Reactive Ion Etching (DRIE) and LIGA due to the planar design configuration. The design map presented in this section, based on the proposed PRBM model, can aid in designing and sizing this monolithic and statically balanced power transmission mechanism for various applications and design criteria in different length scales.

REFERENCES

[1] D. F. Machekposhti, N. Tolou, and J. L. Herder, *A review on compliant joints and rigid-body constant velocity universal joints toward the design of compliant homokinetic couplings,* Journal of Mechanical Design **137**, 032301 (2015).

[2] D. F. Machekposhti, N. Tolou, and J. L. Herder, *A fully compliant homokinetic coupling,* Journal of Mechanical Design **140**, 012301 (2018).

[3] D. F. Machekposhti, N. Tolou, and J. Herder, *A statically balanced fully compliant power transmission mechanism between parallel rotational axes,* Mechanism and Machine Theory **119**, 51 (2018).

[4] F. Schmelz, C. H.-C. Seherr-Thoss, and E. Aucktor, *Universal jointed driveshafts for transmitting rotational movements,* in *Universal Joints and Driveshafts* (Springer, 1992) pp. 1–28.

[5] C.-H. Chiang, *Kinematics of spherical mechanisms*, Vol. 5 (Cambridge University Press Cambridge, 1988).

[6] G. A. Thompson, *Constant velocity coupling and control system therefor,* (2006), uS Patent 7,144,326.

[7] H. Kocabas, *Design and analysis of a spherical constant velocity coupling mechanism,* Journal of Mechanical Design **129**, 991 (2007).

[8] N. Sclater and N. P. Chironis, *Mechanisms and mechanical devices sourcebook*, Vol. 3 (McGraw-Hill New York, 2001).

[9] H. Geisthoff, H. Welschof, and P. Herchenbach, *Quasi homokinetic double hooke,* German Patent (1966).

[10] I. S. Fischer, *Numerical analysis of displacements in a tracta coupling,* Engineering with Computers **15**, 334 (1999).

[11] L.-W. Tsai, *Mechanism design: enumeration of kinematic structures according to function* (CRC press, 2000).

[12] D. F. Machekposhti, N. Tolou, and J. L. Herder, *The scope for a compliant homokinetic coupling based on review of compliant joints and rigid-body constant velocity universal joints,* in *ASME 2012 International Design Engineering Technical Conferences and Computers and Information in Engineering Conference* (American Society of Mechanical Engineers, 2012) pp. 379–392.

[13] L. L. Howell, *Compliant mechanisms* (John Wiley & Sons, 2001).

[14] D. F. Machekposhti, N. Tolou, and J. L. Herder, *Monolithic and statically balanced rotational power transmission coupling for parallel axes,* in *Microactuators and Micromechanisms* (Springer, 2017) pp. 189–198.

[15] G. Ananthasuresh and S. Kota, *The role of compliance in the design of mems,* in *Proceedings of the 1996 ASME Design Engineering Technical Conferences*, Vol. 96 (1996).

[16] S. Kota and G. Ananthasuresh, *Designing compliant mechanisms,* Mechanical Engineering-CIME **117**, 93 (1995).

[17] E. Tanık and V. Parlaktaş, *Compliant cardan universal joint,* Journal of mechanical design **134**, 021011 (2012).

[18] J. E. Baker, *Displacement–closure equations of the unspecialised double-hooke's-joint linkage,* Mechanism and machine Theory **37**, 1127 (2002).

[19] K. Hunt, *Constant-velocity shaft couplings: a general theory,* Journal of Engineering for Industry **95**, 455 (1973).

[20] K. Hunt, *Structural kinematics of in-parallel-actuated robot-arms,* Journal of Mechanisms, Transmissions, and Automation in Design **105**, 705 (1983).

[21] M. d'Ocagne, *Cours de géométrie, pure et appliquée,* Bull. Amer. Math. Soc. 36 (1930), 789-790 DOI: http://dx. doi. org/10.1090/S0002-9904-1930-05057-0 PII , 0002 (1930).

[22] I. H. Culver, *Constant velocity universal joint,* (1969), uS Patent 3,477,249.

[23] J. Denavit, *A kinematic notation for lower-pair mechanisms based on matrices.* Trans. of the ASME. Journal of Applied Mechanics **22**, 215 (1955).

[24] H. Lee, C. Woernle, and M. Hiller, *A complete solution for the inverse kinematic problem of the general 6r robot manipulator,* Journal of Mechanical Design **113**, 481 (1991).

[25] M. Raghavan and B. Roth, *Inverse kinematics of the general 6r manipulator and related linkages,* Journal of Mechanical Design **115**, 502 (1993).

[26] B. P. Trease, Y.-M. Moon, and S. Kota, *Design of large-displacement compliant joints,* Journal of mechanical design **127**, 788 (2005).

[27] J. J. Sniegowski and E. J. Garcia, *Surface-micromachined gear trains driven by an on-chip electrostatic microengine,* IEEE Electron Device Letters **17**, 366 (1996).

[28] E. J. Garcia and J. J. Sniegowski, *Surface micromachined microengine,* Sensors and Actuators A: Physical **48**, 203 (1995).

[29] S. T. Smith, *Foundations of ultra-precision mechanism design*, Vol. 2 (CRC Press, 2003).

[30] S. L. Miller, J. J. Sniegowski, G. LaVigne, and P. J. McWhorter, *Friction in surface-micromachined microengines,* in *1996 Symposium on Smart Structures and Materials* (International Society for Optics and Photonics, 1996) pp. 197–204.

[31] D. F. Machekposhti, N. Tolou, and J. L. Herder, *A fully compliant constant velocity universal joint,* in *ASME 2015 International Design Engineering Technical Conferences and Computers and Information in Engineering Conference* (American Society of Mechanical Engineers, 2015) pp. V05AT08A014–V05AT08A014.

[32] J. B. Hopkins and R. M. Panas, *Design of flexure-based precision transmission mechanisms using screw theory,* Precision Engineering **37**, 299 (2013).

[33] J. Wessels, D. F. Machekposhti, J. L. Herder, G. Sèmon, and N. Tolou, *Reciprocating geared mechanism with compliant suspension,* Journal of Microelectromechanical Systems (2017).

[34] D. F. Machekposhti, N. Tolou, and J. Herder, *A fully compliant homokinetic coupling,* Journal of Mechanical Design .

[35] F. A. Goodknight, *Tape drive coupling apparatus,* (1999), uS Patent 5,992,782.

[36] H. Soemers, *Design principles: for precision mechanisms* (University of Twente, 2011).

[37] F. Freudenstein, L. Tsai, and E. Maki, *The generalized oldham coupling,* Journal of Mechanisms, Transmissions, and Automation in Design **106**, 475 (1984).

[38] J. L. Herder and F. Van Den Berg, *Statically balanced compliant mechanisms (sbcms), an example and prospects,* in *Proceedings of the Design Engineering Technical Conferences and Computer in Engineering Conference, DETC2000/MECH-14144* (2000).

[39] J. L. Herder, *Design of spring force compensation systems,* Journal of Mechanism and Machine Theory **33**, 151 (1998).

[40] A. Lamers, J. A. G. Sánchez, and J. L. Herder, *Design of a statically balanced fully compliant grasper,* Mechanism and machine theory **92**, 230 (2015).

[41] D. Sarojini, T. J. Lassche, J. L. Herder, and G. K. Ananthasuresh, *Statically balanced compliant two-port bistable mechanism,* Journal of Mechanism and Machine Theory **102**, 1 (2016).

[42] R. Jones and I. Young, *Some parasitic deflexions in parallel spring movements,* Journal of Scientific Instruments **33**, 11 (1956).

[43] W. C. Tang, T.-C. Nguyen, and R. T. Howe, *Laterally driven polysilicon resonant microstructures,* in *Micro Electro Mechanical Systems, 1989, Proceedings, An Investigation of Micro Structures, Sensors, Actuators, Machines and Robots. IEEE* (IEEE, 1989) pp. 53–59.

[44] M. Olfatnia, S. Sood, J. J. Gorman, and S. Awtar, *Large stroke electrostatic comb-drive actuators enabled by a novel flexure mechanism,* Journal of Microelectromechanical Systems **22**, 483 (2013).

[45] B. Krijnen and D. M. Brouwer, *Flexures for large stroke electrostatic actuation in mems,* Journal of micromechanics and microengineering **24**, 015006 (2013).

[46] D. M. Brouwer, B. De Jong, and H. Soemers, *Design and modeling of a six dofs mems-based precision manipulator,* Precision Engineering **34**, 307 (2010).

[47] R. M. Panas and J. B. Hopkins, *Eliminating underconstraint in double parallelogram flexure mechanisms,* Journal of Mechanical Design **137**, 092301 (2015).

[48] S. Awtar, A. H. Slocum, and E. Sevincer, *Characteristics of beam-based flexure modules,* Journal of Mechanical Design **129**, 625 (2007).

[49] L. Saggere, S. Kota, and S. Crary, *New design for suspension of linear microactuators,* in *ASME* (1994).

[50] X. Zhou, L. Che, B. Xiong, K. Fan, Y. Wang, and Z. Wang, *Single wafer fabrication of a symmetric double-sided beam–mass structure using drie and wet etching by a novel vertical sidewall protection technique,* Journal of Micromechanics and Microengineering **20**, 115009 (2010).

[51] G. Hao, H. Li, X. He, and X. Kong, *Conceptual design of compliant translational joints for high-precision applications,* Frontiers of Mechanical Engineering **9**, 331 (2014).

6

CONCLUSIONS

This thesis was undertaken to develop new kinematics and synthesis methods for the design of a new generation of compliant transmission mechanisms as alternatives to classical gears and couplings. In this chapter, the previous chapters are looked over and the main original contributions of the performed research are discussed. Furthermore, the limitations of the approach proposed in this research are addressed and recommendations for further research are given.

6.1. CONCLUSIONS

Advances in the field of Micro-Electromechanical-Systems (MEMS) have inaugurated the urge to design alternatives to classical transmission mechanisms with high energy-efficiency and minimal mechanical complexity. Compliant mechanisms have shown a great potential to realize sophisticated motion with minimal mechanical complexity by employing the natural elasticity of their constituted materials. It is in this context that this thesis set out *to innovate kinematics and synthesis methods for the design of compliant and monolithic transmission mechanisms as the alternatives to classical gears and couplings.*

The five chapters of this thesis have shown three major contributions to the field of transmission mechanisms: Development of new kinematics, compliant designs, and synthesis method.

6.1.1. DEVELOPMENT OF NEW KINEMATICS

One of the more significant findings to emerge from this study is the finite travel range kinematics which was proposed as an alternative to classical gears for frequency multiplication. It was shown that the geometrical advantage (*G.A.*) and the frequency advantage (*F.A.*) of the proposed movement can be designed independently, unlike in classical gears where these two are the same. The results in Chapter 2 and Chapter 3 have identified two approaches to double the motion frequency (*F.A.* = 2).

The findings reported in Chapter 2 shed new light on the application of the serial singularity in planar linkages for the design of frequency doubler transmission mechanisms, a principle ratio for frequency multiplication. Two kinematic articulations, one based on a four-bar linkage, and one based on an eight-bar linkage were proposed for frequency doubling (*F.A.* = 2). However, both designs have shown a nonlinear *G.A.* due to the nonlinear kinematics of the proposed linkages. The results indicate that the design based on the eight-bar linkage provides a better kinematic linearity compared to the design based on the four-bar linkage since there were more parameters for kinematic optimization. The kinematics developed in Chapter 3 have shown that frequency doubling with a linear *G.A.* can be achieved by switching between two instant centers of rotation of a lever arm. This was carried out by employing reconfigurable kinematic pairs on the lever arms.

Furthermore, the use of screw theory for the degrees of freedom (DoF) analysis in Chapter 5 has led to a better understanding of the spatial 6R linkages for application in rotational couplings. It was shown that a perfect constant velocity transmission coupling can be realized by adding an extra kinematic constraint on the Double-Hooke's 6*R* linkages without sacrificing the essential DoFs of a universal joint.

6.1.2. DEVELOPMENT OF COMPLIANT DESIGNS

This thesis has reported a diversity of monolithic and contact-less designs for transmission mechanisms, both couplings, and frequency multipliers. All the theoretical analyses regarding the kinematics and stiffness characteristics of the proposed compliant transmission designs were validated using the experimental results and finite element models (FEM). Prototypes were made of several designs at different length scales, where the micro transmission devices were fabricated out of silicon using Deep Reactive Ion Etching

(DRIE).

The compliant designs and analyses presented in Chapter 2, Chapter 3, and Chapter 4 lay the foundation for the development of new types of transmission mechanisms, suitable for on-chip integration, to adapt the frequency and speed requirements of MEMS-based oscillators, sensors, and actuators. The results of the stiffness analyses and experiments have shown that there is a trade-off between adding compliant frequency doubler building blocks and the associated additional motion stiffness. Furthermore, it was shown in Chapter 3 how a buckle-sensitive slender segment can be employed as a compliant reconfigurable kinematic pair, which enables to switch between two instant centers of rotation for frequency doubling with linear kinematic.

The compliant frequency multiplier transmission mechanisms have shown a great potential to integrate energy storage and transmission functionality. For instance, in the application of mechanical wrist watches the internal stiffness of the the proposed compliant transmission designs can potentially replace the conventional Barrel spring and gear train. This allows for size and component reduction, and increases the mechanical efficiency in such applications.

Two compliant designs were shown in Chapter 5 as alternatives to transmission couplings. These were a compliant homokinetic coupling for angular misalignment, and a monolithic transmission mechanism for lateral misalignment between rotational axes. The results highlighted the importance of the constancy of the bearing stiffness (rotational stiffness) of the rotational couplings over the range of motion. This was found essential to guarantee a constant velocity rotation transmission of a compliant coupling in presence of a constant output load. It was further shown that the uniformity of the rotation transmission of the compliant homokinetic coupling can be insensitive to the axis drift of the used flexures by a symmetrical design arrangement of the flexures with respect to the homokinetic plane. The results indicate that by increasing the number of compliant sets around the rotational axis the required actuation torque will be reduced significantly and the proposed compliant homokinetic coupling can be labeled as a nearly statically balanced compliant transmission coupling. Moreover, the increase in the number of compliant sets enhances the torque transmission capability, by increasing the rotational stiffness and maximum load of the compliant design.

6.1.3. DEVELOPMENT OF SYNTHESIS METHOD

A synthesis method was developed in Chapter 4 to design compliant frequency multiplier transmission mechanisms by concatenating different frequency doubler building blocks, which were developed in Chapter 2 and Chapter 3. The investigation of serial singularity in planar mechanisms using instant center approach has provided a deeper insight into the relation between the arrangement of the serial singularity in the planar linkages and the frequency multiplication ratio. The results have shown that any integer frequency ratios based on even, odd, and prime numbers can be achieved by arrangement of frequency doubler building blocks.

6.2. LIMITATIONS AND RECOMMENDATIONS

Apart from the accomplishments in this thesis, several limitations still remain and need to be acknowledged. This can open a range of future research avenues for the next frontier of compliant transmission mechanisms.

A natural progression of this thesis is to analyze the dynamics and buckling instabilities of the proposed compliant transmission mechanisms. Many applications require an understanding of dynamic operating conditions, since the dynamical performance of a compliant mechanism may deviate from its static performance. Therefore, developing dynamic models for the proposed compliant transmission mechanisms provides valuable insight into the dynamic performance, and allows for further design improvements.

The scope of the proposed compliant frequency doubler transmission building blocks in Chapter 2 was limited to four-bar and eight-bar linkages, which was a good trade-off between complexity and performance. Since a higher number of links gives more parameters for the kinematic optimization, a further study could assess the possibilities of frequency doubling in other one-DoF planar mechanisms such as ten-bar, twelve-bar, and fourteen-bar linkages.

The kinematic nonlinearity and the nonlinearity of the actuation stiffness of the proposed compliant frequency multiplier transmission mechanisms results in a nonlinear output force, i.e. output force variations. This limits the practicability of the proposed transmission mechanisms in some applications. For instance, the precision of the oscillator in a mechanical watch is dependent on the level of the constancy of the output force in the transmission line. Further research should be undertaken to explore different strategies to statically balance the proposed compliant frequency multiplier transmission mechanisms to result in a constant output force.

SUMMARY

Classical human-engineered transmission mechanisms such as linkages, gears, and couplings are well established designs which made out of multiple parts and rigid hinges. However, these mechanisms impose disadvantages such as wear, friction, low precision and reliability, need for assembly and lubrications, and difficulty for miniaturization. By employing the natural elasticity of materials, rather than using rigid hinges and connections, sophisticated motions can be realized with minimal mechanical complexity. This relative new paradigm in engineering design, called compliant mechanisms, enables the creation of monolithic mechanisms that are strong, compliant, precise, scalable, and cost-effective.

The kinematics of classical gears and couplings impose several limitations to design their compliant alternatives. One of the main limitations is that gears and couplings are rotating continuously but the range of motion for an elastic mechanism is limited by the stress in the material. Another limitation is that the transmission principle for conventional gears and couplings are based on the engagement between separated bodies and form closure, like teeth and sliding contacts. However, compliant mechanisms transfer motion by elastic deformation of their own materials within a monolithic embodiment. Therefore the aim of this thesis has been to develop kinematics and synthesis methods for the design of compliant and monolithic alternatives to classical gears and couplings.

In Chapter 2 insights from serial singularity in planar linkages are used to develop kinematics for frequency duplication, which is a functionality equivalent with a gearing ratio of two. Two compliant transmission building block, one based on a four-bar linkage, and one based on an eight-bar linkage have been proposed for frequency duplication. The input-output kinematics and force-deflection characteristic of the proposed compliant transmission mechanisms have been studied by using a Pseudo-Rigid-Body model (PRBM). Furthermore, corresponding designs were dimensioned and fabricated at different length scale to validate the PRBM and finite-element model (FEM) with the experimental evaluations. Results have shown a nonlinear geometrical advantage ($G.A.$) due to the nonlinear kinematics of the proposed linkages.

The kinematics developed in Chapter 3 have shown that frequency duplication with a linear $G.A.$ can be achieved by switching between two instant centers of rotation of a lever arm. This was carried out by employing elastic deformation and buckling of slender segments in an embodiment that exhibits a precise and linear transmission of frequency and deflection rate. Furthermore, the input-output kinematics and force-deflection characteristics of the compliant design were described by a theoretical model, and validated experimentally in a silicon MEMS device.

A graphical method based on the instant centers of rotation in planar linkages was proposed in Chapter 4 for the synthesis of frequency multiplier transmission mechanisms. It has shown that any integer frequency multiplication ratios can be achieved by arrangement of frequency doubler building blocks. Furthermore, the developed synthe-

sis method was experimentally validated with two compliant designs with the frequency ratios of "3" and "4".

Compliant transmission couplings, which can deal with different misalignments between the direction of motion of the input and output axes, were developed in Chapter 5. Two compliant designs were shown as alternatives to classical transmission couplings. These were a compliant homokinetic coupling for angular misalignment, and a monolithic transmission coupling for lateral misalignment between rotational axes. The proposed compliant designs have been studied by using PRBM and validated experimentally. The results highlighted the importance of the constancy of the bearing stiffness (rotational stiffness) of the compliant rotational couplings over their range of motion. This was found essential to guarantee a constant velocity rotation transmission of a compliant coupling in presence of a constant output load.

Furthermore, the use of screw theory for the degrees of freedom (DoF) analysis in Chapter 5 has led to a better understanding of the spatial 6R linkages for application in rotational couplings. It was shown that a precise constant velocity homokinetic coupling can be achieved by adding an extra kinematic constraint on the Double-Hooke's $6R$ linkages without sacrificing the essential DoFs of a universal joint. Furthermore, it was shown that the uniformity of the rotation transmission of the compliant homokinetic coupling can be insensitive to the axis drift of the used flexures by a symmetrical flexure design arrangement.

SAMENVATTING

Klassiek door de mens ontworpen mechanismen, zoals stangenmechanismen, tanwielen en koppelingen, zijn veel gebruikte en bekende ontwerpen, bestaande uit starre lichamen en scharnieren. Aan deze mechanismen kleven echter ook nadelen. Ze hebben last van slijtage en wrijving, hebben vaak een lage precisie en betrouwbaarheid, moeten geassembleerd en gesmeerd worden en zijn vaak moeilijk te miniaturiseren. Door de natuurlijke elasticiteit van materialen te gebruiken in plaats van starre verbindingen, kunnen geavanceerde bewegingen worden gerealiseerd met minimale mechanische complexiteit. Dit relatief nieuwe paradigma in werktuigbouwkundig ontwerp, compliante mechanismen genoemd, maakt monolithische mechanismen mogelijk die sterk, compliant, nauwkeurig, schaalbaar en kosteneffectief zijn.

De kinematica van klassieke tandwielen en koppelingen leggen echter wel enkele beperkingen op aan het ontwerp van hun compliante alternatieven. Een van de belangrijkste beperkingen is dat tandwielen en koppelingen vrij kunnen roteren, terwijl het bewegingsbereik van een elastisch mechanisme wordt beperkt door de spanning in het materiaal. Een andere beperking is dat het transmissieprincipe voor conventionele tandwielen en koppelingen gebaseerd is op het in elkaar grijpen van losse lichamen en vormgeslotenheid zoals tanden en glijcontacten, terwijl in compliante mechanismen bewegingen worden overgedragen via elastische deformatie van het materiaal in één enkel lichaam. Daarom is het doel van dit proefschrift om methoden te wontwikkelen voor de kinematische analyse en synthese van compliante en monolitische alternatieven voor klassieke tandwielmechanismen en koppelingen.

In hoofdstuk 2 worden inzichten in seriële singulariteiten voor mechanismen in het vlak gebruikt voor het ontwikkelen van kinemematica voor frequentieverdubbeling, het functionele equivalent van een tandwieloverbrenging met overbrengsratio twee. Twee compliante transmissiebouwblokken, één gebaseerd op een vierstangenmechanisme en de ander gebaseerd op een achtstangenmechanisme, worden voorgesteld om frequentieverdubbeling te bereiken. De ingangs en uitgangs kinematica en het kracht-weg gedrag van de voorgestelde compliante transmissiemechanismen zijn bestudeerd met behulp van een Pseudo-Rigid-Body-model (PRBM). Daarnaast zijn de ontwerpen gedimensioneerd en vervaardigd om het PRBM en het eindige-elementenmodel met de experimentele evaluaties te valideren. De resultaten laten een niet-lineare overbrengingsverhouding zien als gevolg van de niet-lineare kinematica.

De kinematica ontwikkeld in hoofdstuk 3 laat zien dat de frequentieverdubbeling met een lineare overbrengingsverhouding kan worden gerealiseerd door te wisselen tussen twee momentane rotatiecentra van de hefboomarm. Dit is gerealiseerd door gebruikt te maken van de elastische vervorming en het knikke van slanke segmenten op een manier die een nauwkeurige en lineare transmissie van de frequentie en mate van verbuiging bewerkstelligd. Verder worden van het voorgestelde mechanisme de ingangs en uitgans kinematica en het kracht-weg gedrag beschreven met behulp van een theore-

tisch model en word deze experimenteel gevalideerd door middel van een MEMS apparaat.

Een grafische methode op basis van momentane rotatiecentra voor de synthese van transmissiemechanismen voor frequentievermenigvuldiging in het vlak wordt voorgesteld in hoofdstuk 4. Door middel van deze methode is aangetoond dat elke geheeltallige frequrentievermenigvuldiging kan worden behaald door een aaneenschakeling van bouwblokken die de frequentie verdubbelen. Daarnaast is de ontwikkelde synthese methode experimenteel gevalideerd met twee compliante transmissiemechanisme-ontwerpen voor frequentievermenigvuldiging met een factor 3 en 4.

Compliante transmissiekoppelingen die om kunnen gaan met verschillende uitlijnfouten tussen de in- en uitgangsbeweging worden gepresenteerd in hoofdstuk 5. De ontwerpen bieden een alternatieven voor klassieke transmissiekoppelingen. Een compliante homokinetische koppeling voor een uitlijnfout in de hoek tussen de assen en een monolithische transmissiekoppeling voor een translationele uitlijningsfout worden gepresenteerd. Deze compliante transmissiekoppelingen zijn bestudeerd met behulp van PRBM en experimenteel gevalideerd. De resultaten benadrukken het belang van een constante draagkracht (torsiestijfheid) van de compliante rotatiekoppeling over hun bewegingsbereik. Dit bleek essentieel om een constante rotatiesnelheid over te kunnen dragen met behulp van een compliante koppeling in het geval van een constante uitgansbelasting.

Het gebruik van screw theory voor de analyse van de graden van vrijheid in hoofdstuk 5 heeft geleid tot een beter begrip van de ruimtelijke 6R stangenmechanismen voor applicaties in rotatiekoppelingen. Hieruit bleek dat een precieze homokinetische koppeling met een constante snelheidsoverbrenging kan worden gemaakt door het toevoegen van een extra kinematische beperking aan Double-Hooke's 6R stangenmechanismen zonder dat de essentiële graden van vrijheid van een universele koppeling worden opgeofferd. Daarnaast is aangetoond dat de uniformiteit van de rotatietransmissie van de compliante homokinetische koppeling ongevoelig kan zijn voor asafwijkingen door de flexibele elementen symmetrisch te plaatsen ten opzichte van het homokinetische vlak.

CURRICULUM VITÆ

Davood FARHADI MACHEKPOSHTI

18 - 12 - 1987 Born in Sary, Iran.

EDUCATION

2006 – 2010	**B.Sc.** in Mechanical Engineering, *Babol Noshirvani University of Technology, Babol, Iran.*
2010 – 2013	**M.Sc.** in Mechanical Engineering-Applied Mechanics. *Babol Noshirvani University of Technology, Babol, Iran.* *Thesis: Kinematics of Spatial Transmission Mechanisms*
2014 – 2018	**Ph.D.** in Precision and Microsystems Engineering, *Delft University of Technology, Delft, The Netherlands.* *Thesis: Compliant Transmission Mechanisms* *Promotor: Prof. dr. ir. Just L Herder*

EXPERIENCE

Sept.2017 – Dec.2017	**Visiting Researcher** at Chair of Applied Mechanics, *Technical University of Munich, Munich, Germany,* *Research Topic: Nonlinear Dynamics of Compliant Mechanisms.*
June 2018 – Present	**Post-Doc** in Precision and Microsystems Engineering, *Delft University of Technology, Delft, The Netherlands.*

AWARDS AND DISTINCTIONS

2013	M.Sc. Degree with Honors
2015	Best Interactive Demo Award, Mechanisms and Robotics Conference, Boston, USA.
2015	Finalist, Mechanism Design Competition, Boston, USA.
2015	Conference Travel grant (1500 EUR), ASME/IDETC, Boston, USA.

OUTREACH

2018	Swiss Watches Featuring Dutch Precision, Mikroniek, Magazine.
2018	TU Delft en Tag Heuer bouwen frequentievermenigvuldiger uit een stuk, Mechatronica en Machinebouw, Dutch Magazine.

PATENTS

1. **D. Farhadi Machekposhti**, N. Tolou, *"Compliant Constant Velocity Constant Torque Universal Joint"*, US Patent, Application Number. US20150065259A1 (2013).
2. **D. Farhadi Machekposhti**, J. L. Herder, N. Tolou, *"Mechanical Frequency Converter Utilizing Singularity"*, Dutch Patent, Application Number. 2020143 (2017).
3. **D. Farhadi Machekposhti**, J. L. Herder, N. Tolou, *"Mechanical Frequency Converter Utilizing Buckling"*, Dutch Patent, Application Number. 2020145 (2017).
4. G.J. van den Doel, **D. Farhadi Machekposhti**, J. L. Herder, *"Transmission Mechanism"*, Dutch Patent, Application Number. N2021122 (2018).

LIST OF PUBLICATIONS

JOURNAL PUBLICATIONS

1. **D. Farhadi Machekposhti**, N. Tolou, J. L. Herder, *A Review on Compliant Joints and Rigid-Body Constant Velocity Universal Joints Toward the Design of Compliant Homokinetic Couplings*, Journal of Mechanical Design 137 (3), 032301 (2015).

2. J. Wessels, **D. Farhadi Machekposhti**, J. L. Herder, G. Sémon, N. Tolou, *Reciprocating Geared Mechanism with Compliant Suspension*, Journal of Microelectromechanical Systems 26 (5), 1047-1054 (2017).

3. **D. Farhadi Machekposhti**, N. Tolou, J. L. Herder, *A Fully Compliant Homokinetic Coupling*, Journal of Mechanical Design 140 (1), 012301 (2018).

4. **D. Farhadi Machekposhti**, N. Tolou, J. L. Herder, *A Statically Balanced Fully Compliant Power Transmission Mechanism Between Parallel Rotational Axes*, Mechanism and Machine Theory 119, 51-60 (2018).

5. **D. Farhadi Machekposhti**, J. L. Herder, G. Sémon, N. Tolou, *A Compliant Micro Frequency Quadrupler Transmission Utilizing Singularity*, Journal of Microelectromechanical Systems 27 (3), 506-512 (2018).

6. **D. Farhadi Machekposhti**, J. L. Herder, N. Tolou, *Buckling can be Utilized to Design a Frequency Doubler Transmission Mechanism*, Applied Physics Letters (Submitted 2018).

PEER-REVIEWED CONFERENCE PAPERS

1. **D. Farhadi Machekposhti**, N. Tolou, J. L. Herder, *A Fully Compliant Constant Velocity Universal Joint*, ASME IDETC/CIE, DETC2015-46813, Boston, United States (2015).

2. **D. Farhadi Machekposhti**, N. Tolou, J. L. Herder, *Monolithic and statically balanced rotational power transmission coupling for parallel axes*, Microactuators and Micromechanisms, 189-198, Ilmenau, Germany (2016).